Theses and Dissertations   1. Thesis and Dissertation Collection, all items

2010-09

Development of a receiver processor for UAV video signal acquisition and tracking using digital phased array antenna

Kaya, Fevzi Aytac

Monterey, California. Naval Postgraduate School

http://hdl.handle.net/10945/5221

NAVAL POSTGRADUATE SCHOOL

MONTEREY, CALIFORNIA

THESIS

DEVELOPMENT OF A RECEIVER PROCESSOR FOR UAV VIDEO SIGNAL ACQUISTION AND TRACKING USING DIGITAL PHASED ARRAY ANTENNA

by

Fevzi Aytaç Kaya

September 2010

Thesis Advisor:	David C. Jenn
Second Reader:	Terry Smith

Approved for public release; distribution is unlimited

THIS PAGE INTENTIONALLY LEFT BLANK

REPORT DOCUMENTATION PAGE		*Form Approved OMB No. 0704-0188*
Public reporting burden for this collection of information is estimated to average 1 hour per response, including the time for reviewing instruction, searching existing data sources, gathering and maintaining the data needed, and completing and reviewing the collection of information. Send comments regarding this burden estimate or any other aspect of this collection of information, including suggestions for reducing this burden, to Washington headquarters Services, Directorate for Information Operations and Reports, 1215 Jefferson Davis Highway, Suite 1204, Arlington, VA 22202-4302, and to the Office of Management and Budget, Paperwork Reduction Project (0704-0188) Washington DC 20503.

1. AGENCY USE ONLY *(Leave blank)*	**2. REPORT DATE** September 2010	**3. REPORT TYPE AND DATES COVERED** Master's Thesis

4. TITLE AND SUBTITLE Development of a Receiver Processor For UAV Video Signal Acquisition and Tracking Using Digital Phased Array Antenna	**5. FUNDING NUMBERS**

6. AUTHOR(S) Fevzi Aytaç Kaya

7. PERFORMING ORGANIZATION NAME(S) AND ADDRESS(ES) Naval Postgraduate School Monterey, CA 93943-5000	**8. PERFORMING ORGANIZATION REPORT NUMBER**
9. SPONSORING /MONITORING AGENCY NAME(S) AND ADDRESS(ES) N/A	**10. SPONSORING/MONITORING AGENCY REPORT NUMBER**

11. SUPPLEMENTARY NOTES The views expressed in this thesis are those of the author and do not reflect the official policy or position of the Department of Defense or the U.S. Government. IRB Protocol number _____N/A_____.

12a. DISTRIBUTION / AVAILABILITY STATEMENT Approved for public release; distribution is unlimited	**12b. DISTRIBUTION CODE**

13. ABSTRACT

Air dominance is a key factor concerning today's warfare. Obtaining air dominance requires having a high degree of situational awareness. Unmanned aerial vehicles (UAVs) have gained popularity for surveillance and reconnaissance missions and provide situational awareness to ground-based military units. During operations it is necessary to maintain an uninterrupted data and control link between the UAV and the ground control station (GCS). This requires GCS antennas with signal-tracking capability.

The work on this research was based on an ongoing project that originally started in 2002. The ultimate purpose is to design and build a digital phased-array antenna system that can automatically acquire, track, demodulate and decode video signals from a UAV using commercial-off-the-shelf (COTS) equipment. Previous work done includes integration of hardware components and development of software modules that allow the array system to auto-track signals from a UAV as well as decode the video signals in a standard format. The research in this thesis focused on allowing the system to demodulate the video signals acquired by the digital tracking array. The baseband demodulation technique implemented was previously tested with video signals. A new technique utilizing tangent-type demodulation of signals was also implemented and tested using a bench-top test setup.

14. SUBJECT TERMS Air Dominance, Situational Awareness, UAV, Digital Phased Array Antenna, Tracking, Video Signal, Commercial-Off-The-Shelf, Hardware, Software Modules, NTSC, Baseband Demodulation, Tangent Type Demodulation	**15. NUMBER OF PAGES** 177
	16. PRICE CODE

17. SECURITY CLASSIFICATION OF REPORT Unclassified	**18. SECURITY CLASSIFICATION OF THIS PAGE** Unclassified	**19. SECURITY CLASSIFICATION OF ABSTRACT** Unclassified	**20. LIMITATION OF ABSTRACT** UU

NSN 7540-01-280-5500

THIS PAGE INTENTIONALLY LEFT BLANK

**DEVELOPMENT OF A RECEIVER PROCESSOR
FOR UAV VIDEO SIGNAL ACQUISITION AND TRACKING
USING DIGITAL PHASED ARRAY ANTENNA**

Fevzi Aytaç Kaya
1st Lieutenant, Turkish Air Force
B.S., Gazi University, 2005

Submitted in partial fulfillment of the
requirements for the degrees of

**MASTER OF SCIENCE IN ELECTRONIC WARFARE
SYSTEMS ENGINEERING**
and
MASTER OF SCIENCE IN ELECTRICAL ENGINEERING

from the

**NAVAL POSTGRADUATE SCHOOL
September 2010**

Author: Fevzi Aytaç Kaya

Approved by: David C. Jenn
Thesis Advisor

Terry Smith
Second Reader

Dan C. Boger
Chairman, Department of Information Sciences

Clark Robertson
Chairman, Department of Electrical and Computer Engineering

THIS PAGE INTENTIONALLY LEFT BLANK

ABSTRACT

Air dominance is a key factor concerning today's warfare. Obtaining air dominance requires having a high degree of situational awareness. Unmanned aerial vehicles (UAVs) have gained popularity for surveillance and reconnaissance missions and provide situational awareness to ground-based military units. During operations it is necessary to maintain an uninterrupted data and control link between the UAV and the ground control station (GCS). This requires GCS antennas with signal-tracking capability.

The work on this research was based on an ongoing project that originally started in 2002. The ultimate purpose is to design and build a digital phased-array antenna system that can automatically acquire, track, demodulate and decode video signals from a UAV using commercial-off-the-shelf (COTS) equipment. Previous work done includes integration of hardware components and development of software modules that allow the array system to auto-track signals from a UAV as well as decode the video signals in a standard format. The research in this thesis focused on allowing the system to demodulate the video signals acquired by the digital tracking array. The baseband demodulation technique implemented was previously tested with video signals. A new technique utilizing tangent-type demodulation of signals was also implemented and tested using a bench-top test setup.

THIS PAGE INTENTIONALLY LEFT BLANK

TABLE OF CONTENTS

THIS PAGE INTENTIONALLY LEFT BLANK

LIST OF FIGURES

THIS PAGE INTENTIONALLY LEFT BLANK

LIST OF TABLES

THIS PAGE INTENTIONALLY LEFT BLANK

LIST OF ACRONYMS AND ABBREVIATIONS

A/D   Analog to Digital

ADT   Automatic Detection and Track

AF   Array Factor

AM   Amplitude Modulation

AOA   Angle of Arrival

BER   Bit Error Rate

COTS   Commercial off The Shelf

DBF   Digital Beamforming

DF   Direction Finding

DSP   Digital Signal Processing

EMI   Electromagnetic Interference

ESA   Electronically Scanned Array Antennas

EW   Electronic Warfare

FM   Frequency Modulated/Modulation

FOV   Field of View

GCS   Ground Control Station

HPA   High Power Amplifier

HPBW   Half-Power Beam Width

JDAM   Joint Direct Attack Munitions

I   In-phase

IC   Integrated Circuit

IP   Intercept Point

IRE	Institute of Radio Engineers
LNA	Low Noise Amplifier
LO	Local Oscillator
LPF	Low Pass Filter
MGTOW	Maximum Gross Takeoff Weight
MMIC	Monolithic Microwave Integrated Circuits
MTBF	Mean-time Between Failures
NI	National Instruments
NTSC	National Television Standards Committee
OODA	Observation-Orientation-Decision-Action
PAL	Phase Alternating Line
PCB	Printed Circuit Board
PLL	Phase Locked Loop
PM	Phase Modulation
Q	Quadrature
RF	Radio Frequency
RSNS	Robust Symmetric Numeric System
SAR	Synthetic Aperture Radar
SECAM	Systeme Electronic Pour Avec Memoire
SNR	Signal to Noise Ratio
STT	Single Target Tracking
TBM	Tactical Ballistic Missile
T/R	Transmit/Receive
TWS	Track While Scan

UAV	Unmanned Aerial Vehicle
UCAV	Unmanned Combat Aerial Vehicle
USA	Unites States of America
USAF	Unites States Air Force
USB	Universal Serial Bus
VCO	Voltage Controlled Oscillator
VI	Virtual Instrument

THIS PAGE INTENTIONALLY LEFT BLANK

EXECUTIVE SUMMARY

In today's warfare the concept of air dominance has emerged as a key factor. The ability to gain air dominance is crucial in the sense that it saves lives, affects the duration of the combat and ensures the accomplishment of national and military objectives. The capability of obtaining air dominance requires a high degree of situational awareness during combat. Research and developments in several areas have led to sensor systems that can increase the level of situational awareness in a combat environment. Unmanned aerial vehicles (UAVs) are among the most important of these systems. From their operational beginnings as converted target drones to the more sophisticated battlefield observation platforms, UAVs have finally gained acceptance by the military community. During military operations, UAVs provide a high degree of situational awareness by carrying out surveillance and reconnaissance missions that lead to gaining air dominance against adversaries.

One of the biggest challenges encountered in UAV operations is the ability to establish secure and reliable data links between the UAV and ground stations. Disruption in data links can easily occur and the quality and speed of the data received may be adversely affected. This necessitates an antenna, possibly with an electronic beam steering and tracking capability, to sustain a reliable data link between the UAV and the ground control station (GCS). When the signal is received at the GCS, signal processing techniques are used to retrieve the necessary data (e.g., video).

The advancements in the field of signal processing have provided several advantages. Many tasks that used to be done via hardware can now be done using software. With this opportunity, today's GCSs can be built at relatively lower costs, in smaller spaces, and are easily upgraded. Another important technological advancement is the phased-array antenna. The advent of relatively low-cost monolithic microwave integrated circuits (MMICs), automated assembly of microwave components, and new low-cost high-speed digital processors led to the development and optimization of these

antennas. Phased arrays have the capability to steer their beams electronically in nanoseconds by using processor-controlled phase adjustments for each individual antenna element.

The objective of the research presented in this thesis, as part of an ongoing project, is to develop a digital tracking array for use in communications with a UAV using commercial-off-the-shelf (COTS) components that reduce overall cost. The research previously done in key areas comprised a robust symmetric number system (RSNS) direction-finding processor, and digital beamforming (DBF) as well as demodulation and decoding techniques for video data transmission. The previous research focused on the optimization of the demodulation techniques in order to bring the digital tracking array the capability to successfully retrieve and display the video data embedded in the frequency modulated (FM) signals received by the antenna. An in-depth review of the properties and functionalities of the current system and its components was also made in order to provide a useful reference for future studies.

The feasibility of utilizing new demodulation techniques for the proper demodulation of the video signals was previously investigated. The tangent-type demodulation technique was studied as a novel approach for the demodulation process. The baseband FM demodulation technique implemented previously was limited to simple sinusoidal input waveforms. This technique was enhanced to handle video signals. The applicability of these two techniques in the receiver system was validated by computer simulations done in both MATLAB and LabView. It was seen that FM video signals received from a UAV can be successfully demodulated by using either the baseband or tangent-type demodulation techniques.

The development of the software modules for the receiver processor was done using a modular approach to complement the previous work done. Based on the results of the simulations, an FM demodulation module utilizing the tangent-type demodulation technique for the demodulation of FM video signals was developed. Additionally, the previous FM demodulation module, using the baseband demodulation technique was modified for video signal demodulation. Both modules were developed for operation on a single array channel. Subsequently, both modules were tested using a bench-top test

setup. Different waveforms were used as input-modulating signals. The waveforms tested were chosen to range from simple to complex signal content. Hence they included sinusoidal, square, and ramp waves and, for the more complex representations, real-time streaming video signals.

The newly developed tangent-type FM demodulation module showed similar performance compared to the previous baseband demodulation module. Both modules were able to demodulate the sine wave. The demodulated square and ramp waves by both modules had distortions due to the attenuation of high-frequency components by the filters. However, the fundamental frequencies of both waves were retrieved. The baseband video signals were frequency modulated and then successfully demodulated using both demodulation modules. However, the video signals obtained had excessive distortion levels which prevented decoding of the video data. The filter cut-off frequencies were decreased to eliminate the high-frequency noise. A slight improvement was obtained; however, the video data still could not be decoded and displayed by the video decoder. This was due to the corruption of the synchronization (sync) pulses within the video signals. The video decoder used measures the duration of the sync pulses and compares the measured value with the minimum duration required for a valid sync pulse. The distortions on the demodulated signals prevented the decoder to validate the sync pulses. As a result they were considered as noise and the video could not be displayed.

The development process also included the modification of the user interfaces of the previously developed software modules. The previous user interfaces of the National Television Standards Committee (NTSC) decoding module and the baseband FM demodulation module were examined, analyzed and modified to provide more efficient functionality and analysis. The functionality of the modified NTSC decoding module was tested using a bench-top test setup and verified using unmodulated streaming video obtained from a video camera as the input. However, when integrated within the demodulation modules, the module failed to decode and display the demodulated video obtained at the output of the demodulators due to the excessive noise level of the demodulated signals.

THIS PAGE INTENTIONALLY LEFT BLANK

ACKNOWLEDGMENTS

THIS PAGE INTENTIONALLY LEFT BLANK

I.   INTRODUCTION

A.   BACKGROUND

Air dominance has emerged as one of the most important factors concerning today's warfare. The ability to gain air dominance is crucial in the sense that it saves lives, affects the length of the conflict and the quality of the peace, and ensures the accomplishment of national and military objectives [1]. Obtaining air dominance requires a high degree of situational awareness during combat. In the last few decades, various systems have been developed to increase the level of situational awareness in a combat environment. Unmanned aerial vehicles (UAVs) are among the most important of these systems. From their operational beginnings as converted target drones to today's more sophisticated battlefield observation platforms, UAVs have finally gained acceptance by the military community. During Operation Desert Storm in 1991, it was even reported that an Iraqi ground unit attempted to surrender to a U.S. Pioneer UAV as it buzzed overhead [2].

Today's UAVs can carry out a variety of military and civilian applications. One of the most common missions in which UAVs are extensively used is remote sensing. This includes surveillance and reconnaissance, target recognition, search and rescue and even traffic monitoring. These kinds of UAVs employ various kinds of electromagnetic sensors in order to achieve their missions. Electromagnetic sensors include visual sensors, infrared or near-infrared cameras, and radar systems [3].

UAVs can also be used for transporting goods. For example, a UAV can be used to transport emergency medical supplies to frontline troops in a battlefield environment. UAVs are uniquely capable of penetrating into areas where it is highly dangerous for human beings to approach. This feature makes UAVs capable of monitoring contaminated areas (such as the Chernobyl disaster) without risk to human life.

Today, new military applications are opening to UAVs—beyond their traditional surveillance and reconnaissance missions. Currently, UAVs are effectively used in electronic warfare (EW) as airborne jammers, decoys, and emitter locators. Future roles are likely to include anti-radar hard kill, communications relay, pre-launch and boost-phase tactical ballistic missile (TBM), and both lethal and non-lethal submunition dispensing.

Being a complex aerial system, UAVs have several design challenges. One of the biggest problems encountered in UAV operations is establishing secure and reliable data links between the UAV and ground stations. Disruption in the data link can easily occur, and the quality and speed of the data received may be adversely affected. Of the 36 Pioneer UAVs (Figure 1) lost by the U.S. during Operation Desert Storm, only one was lost to enemy fire. Eleven of them, however, were lost due to loss of data link. From the Pioneer example, it can be understood that it is important for the ground control station (GCS) to accurately track the signals coming from a UAV. This necessitates a directional antenna, possibly with electronic beam steering and with tracking capability to sustain a reliable data link between the UAV and the GCS. When the UAV signal is received at the GCS, signal processing techniques are used to retrieve the necessary data (e.g., video).

Considering the operational environment, we see that the observation-orientation-decision-action (OODA) loop, which is described in [4], has great importance in all kinds of military operations. The OODA loop is a function of the characteristic tempo of operations and, hence, situational awareness. A war-fighting enterprise that can process the entire OODA cycle quickly, observing and reacting to unfolding events more rapidly than an opponent, can "get inside" the opponent's decision cycle and gain a military advantage. From this perspective, establishing a reliable and uninterrupted data link between a GCS and a UAV will decrease the time needed in the decision-making process (operational tempo). Once disrupted, an enemy's operational tempo may be stretched in time, thus providing additional opportunities to exploit the enemy's weaknesses.

Figure 1.   Pioneer UAV used by the U.S. in Operation Desert Storm (From [5]).

There has been much technological advancement in the field of signal processing in the last few decades. Many tasks that used to be done via hardware can now be done using software that employs digital signal-processing techniques. With these developments, today's GCSs can be built at relatively lower costs and occupying less space. Another important technological advancement is the phased array antenna. The advent of relatively low-cost gallium arsenide (GaAs) monolithic microwave integrated circuits (MMICs), automated assembly of microwave components and new low-cost, high-speed digital processors led to the development and optimization of these antennas. They have the capability to steer their beams electronically in nanoseconds by using phase adjustments for each individual antenna element.

Phased arrays consist of a collection of individual antennas that are geometrically arranged and excited so as to provide the desired radiation characteristics. Traditionally, the elements are connected by a system of microwave transmission lines and power

3

dividers (the beamforming network). The array radiates or receives energy over a spatial angle (beam) that is measured by its half-power beam width (HPBW), which is also referred to as the field-of-view (FOV) [6].

In Figure 2, block diagrams of a conventional and a digital phased array antenna are shown. For the data transmission between a UAV and a GCS using a conventional phased array, the data is encoded onto a baseband waveform that is up-converted to the operating band—2.4 gigahertz (GHz) for the proposed system—then amplified and sent to the antenna. On the receive side (i.e., GCS), the signal out of the antenna is down-converted to baseband in the receiver and the information contained in the received message is reconstructed. For digital phased arrays, each element has its own transmitter and receiver combined into a transmit-receive (T/R) module. This eliminates the need for a beamforming network. The received signal processing is performed in a digital beamformer. Advancements in the development of low-cost miniaturized electronics and fast, powerful, computer processors have made this architecture practical for many applications [6].
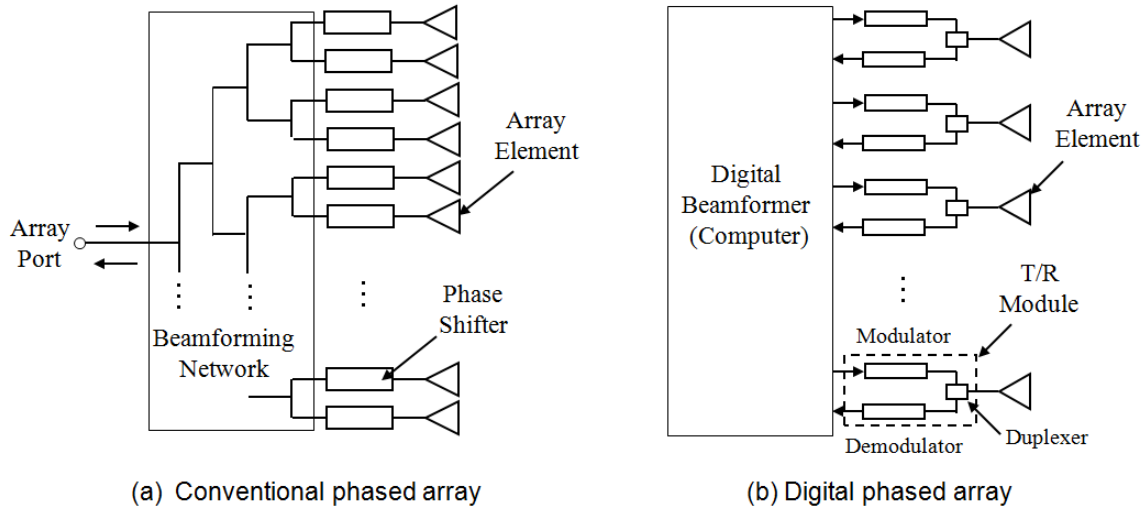
Figure 2.   Conventional (a) and digital (b) phased-array architectures (From [6]).

Another important advantage that comes with phased-array antennas is reliability. With their fixed structure, phased-array antennas eliminate the need for gimbal systems, servos and rotary joints to steer the beam of the antenna. These components are possible sources of mission failures because of breakdowns even though there is nothing wrong with the processors or the array itself. Using electronic beam steering eliminates these problems and provides an improved mean-time between failures (MTBF), which may even extend to a period as long as the lifetime of the antenna.

In a phased array, digital processing techniques can also be applied to track the transmitting UAV. For a UAV located at a close range to the GCS, the beam should be formed wider in order to keep up with the faster change in the angle of arrival (AOA) of the signal. Similarly, if the range between the GCS and the UAV is long, a narrow beam is preferred since more power density in a narrow angular range is required. This concept is illustrated in Figure 3.
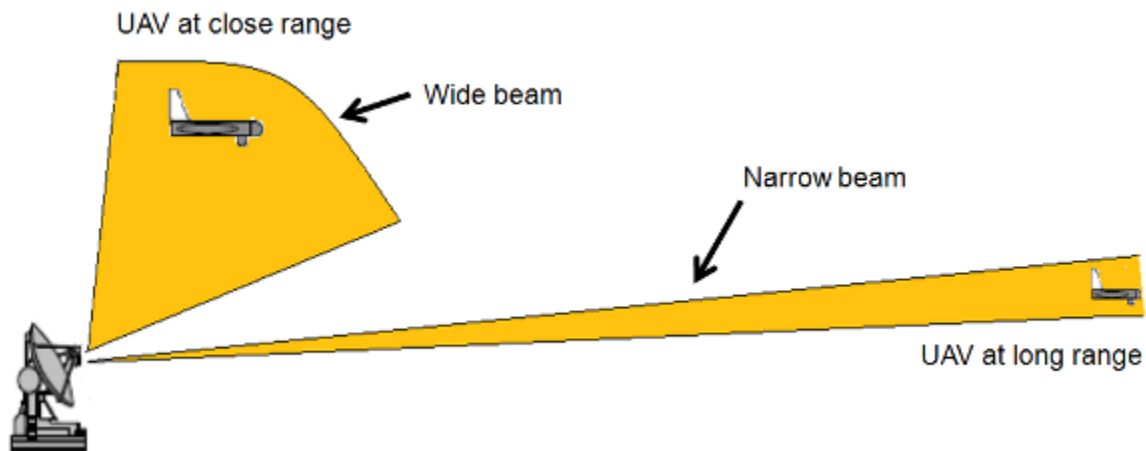
Figure 3.   UAV tracking beam formation according to range.

With the help of high-speed digital processing techniques, real-time video streams can be relayed from a UAV to personnel on the ground, providing better situational awareness. This video data can also be transmitted to the decision-makers located in the headquarters away from the battlefield and the decision process can be efficiently supported.

B. PREVIOUS WORK

This research is part of an ongoing project that originally started with Bartee [7] in 2002. Ong [8] studied the receiver part of the project and investigated the periodic phase error attributed to the modulator boards. He was able to eliminate the phase errors by modifying the bias voltage conditions that were used. Burgstaller [9] characterized the critical commercial-off-the-shelf (COTS) hardware to reduce cost in 2006.

Using the device information obtained in the studies mentioned above, Gezer [10] designed and built a digital array employing the National Instruments (NI) cRIO system to process down-converted data from the COTS hardware. Gezer also determined system design parameters, such as element spacing, scan angle, HPBW, gain, number of elements, signal-to-noise ratio (SNR) and operating range.

Later, direction finding (DF) methods were studied by Lee [11] and Benveniste [12] using the Robust Symmetrical Number System (RSNS). DF is of interest in this study for the purpose of acquisition. Lee developed a three-channel phase interferometer using RSNS and tested the antenna array using relatively prime moduli for direction finding. Benveniste developed a single-channel RSNS system with virtual spacing for direction finding.

Finally, Tan and Pandya [13] researched advanced techniques of the RSNS and Digital Beamforming (DBF) to accurately acquire and track a UAV signal using the monopulse technique. They determined optimum power levels for the direct-conversion receiver to ensure optimum performance and integrated the antenna array and the receivers into a single chassis. They also tested the antenna array in an anechoic chamber.

For the software part, using LabView, Tan and Pandya implemented the monopulse technique and software modules to retrieve a frequency modulated (FM) video signal encoded using the National Television System Committee (NTSC) standard format. They also tested the antenna using different transmit powers and different AOAs.

C.   SCOPE OF RESEARCH

This research effort furthers the ultimate goal of designing, building and testing an antenna array and digital receiver that utilizes DBF for tracking and the RSNS to accurately acquire an FM video signal coming from a UAV. The hardware used was selected from COTS equipment in order to reduce cost.

Software modules were developed and tested to retrieve an FM video signal which was encoded using the NTSC format. Simulations were designed using MATLAB and LabView software to verify the methods used for demodulation. Software module tests were conducted using initially basic signals, such as sine waves, in order to provide a better understanding for the behavior of the demodulation modules designed. Further tests were performed using real time video signals as the modulating signals. The results obtained from the different demodulation methods were compared.

D.   ORGANIZATION OF THESIS

The tracking methods used in tracking antennas are presented in Chapter II. Tracking techniques such as sequential lobing, conical scan and monopulse tracking are also introduced. The theory of the RSNS is given and its application to direction finding is briefly explained. Finally, the theoretical background for DBF and phase interferometry is presented.

The theory behind the direct-conversion receiver architecture is covered in Chapter III. The quadrature detection theory is introduced and the process of down-conversion of signals to baseband is explained. Finally, the advantages and associated problems of the direct conversion architecture are discussed.

The properties of analog and digital video signals are presented in Chapter IV. The formats for the analog video formats are introduced with emphasis on the NTSC format. The frequency modulation and demodulation techniques for baseband in-phase

(I) and quadrature (Q) signals are discussed. The demodulation techniques discussed include baseband demodulation, tangent-type demodulation and demodulation using Kalman filtering.

The hardware and software components of the UAV digital tracking array system are described in Chapter V. The parameters indicating the performance of the components (e.g., antenna) are also given. The LabView programming environment is introduced in order to provide familiarization with the software modules developed. Finally, the details of the software modules are presented.

The validation and verification process for the software modules developed is presented in Chapter VI. The simulations done in order to validate the applicability of the baseband and tangent-type demodulation techniques to the system are presented. The verification process, which includes bench-top testing of the software modules developed, is covered and the results obtained are discussed.

A summary of the work done and the conclusions drawn are provided in Chapter VII. Recommendations for future work are also made.

The Appendix contains MATLAB codes used for the simulation of the software modules in order to validate FM demodulation techniques presented.

II.   ACQUISITION AND TRACKING TECHNIQUES

A tracking array must first find and acquire its target before starting to operate as a tracker. In this section, target acquisition and tracking techniques, which were utilized in the digital array antenna hardware, are covered. In Section A, basic principles of tracking are introduced. In Section B, a brief overview of direction finding with the RSNS is covered. Finally, in Section C, the key principles of DBF are discussed.

A.   TARGET TRACKING

In this section, the target tracking concept is classified into two categories. In the first part, the types of target tracking are discussed. In the second part, the techniques used for target tracking are covered.

1.   Tracking Types

There are four main types of target tracking that are described in the following sub-sections.

a.   *Single-Target Tracking (STT)*

Single-target tracking is used in applications that require a high data rate (i.e., observations per second), such as guided-missile weapon control radar. An example of this kind of radar is shown in Figure 4. As the beam of the antenna follows the target, an angle-error signal is generated continuously. Then, a closed-loop servo system is employed to keep the angle-error small in order to track the target with high accuracy [14].

9

Figure 4.   AN/FPQ-6 Long-range precision tracking radar (From [15]).

b.   *Track While Scan (TWS)*

This type of radar scans a limited angular sector to track more than one target simultaneously within the coverage of the antenna. Common applications include air defense radars and airborne intercept radars [14].

c.   *Automatic Detection and Track (ADT)*

Different from the STT, the position of the antenna in an ADT is not controlled by the processed tracking data. Instead, the antenna makes rotations continuously and the rate at which observations are made depends on the time for the antenna to make one rotation. This results in a lower data rate than the STT, but it provides the capability of tracking a larger number of targets [14].

d. *Phased Array Radar Tracking*

Phased array radars have the capability to steer their beams electronically in nanoseconds. This provides many advantages, such as high data rates and the capability to simultaneously track a large number of targets. With these features, phased-array radars can be considered as the combination of the STT and the ADT radar [14]. Most of the work in this thesis focuses on phased array tracking.

2. Tracking Techniques

In this section, three main techniques for angle tracking are discussed. These techniques are: (1) sequential lobing, (2) conical scan and (3) monopulse tracking. Of interest in this thesis is the monopulse tracking technique. However, the other two techniques will be introduced as well.

a. *Sequential Lobing*

In this tracking technique, the antenna beam is time-shared between two separate directions to obtain the angle measurement in a sequential manner. This process is demonstrated in Figure 5. The difference in amplitude between the voltages obtained in Position 1 and Position 2 is a measure of the angular displacement of the target from the switching axis between the two beam positions. The beam of the antenna is then turned to the direction of the position which has the larger signal level. If the difference is zero, it means the target is on axis.
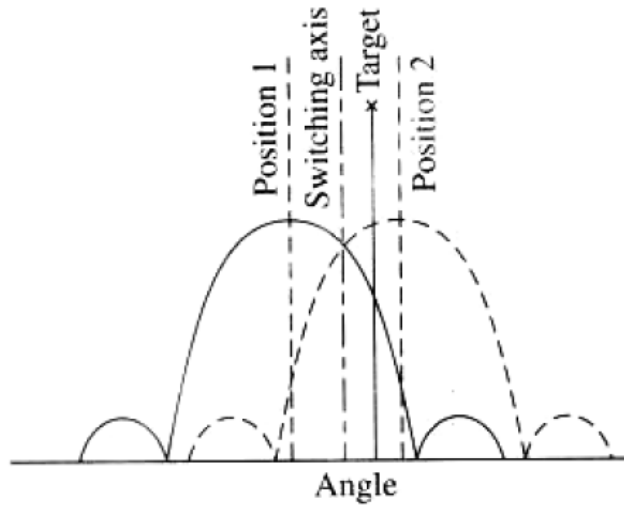
Figure 5.   Rectangular representation of the antenna beam
in two switched positions (From [14]).

b.   *Conical Scan*

The concept of conical scan is illustrated in Figure 6. The antenna beam is squinted and then rotated. The angle between the axis of rotation and the antenna beam axis is called the squint angle. The axis that shows the direction of the axis relative to the antenna is called the target axis. If the target axis and the rotation axis are aligned, the echo responses received as the beam is rotated have equal amplitudes. If unequal amplitude is detected, this means the target is not in the direction of the rotation axis. Hence, the direction of the target can be determined relative to the rotation axis and tracking can be achieved with continuous utilization of this scheme.
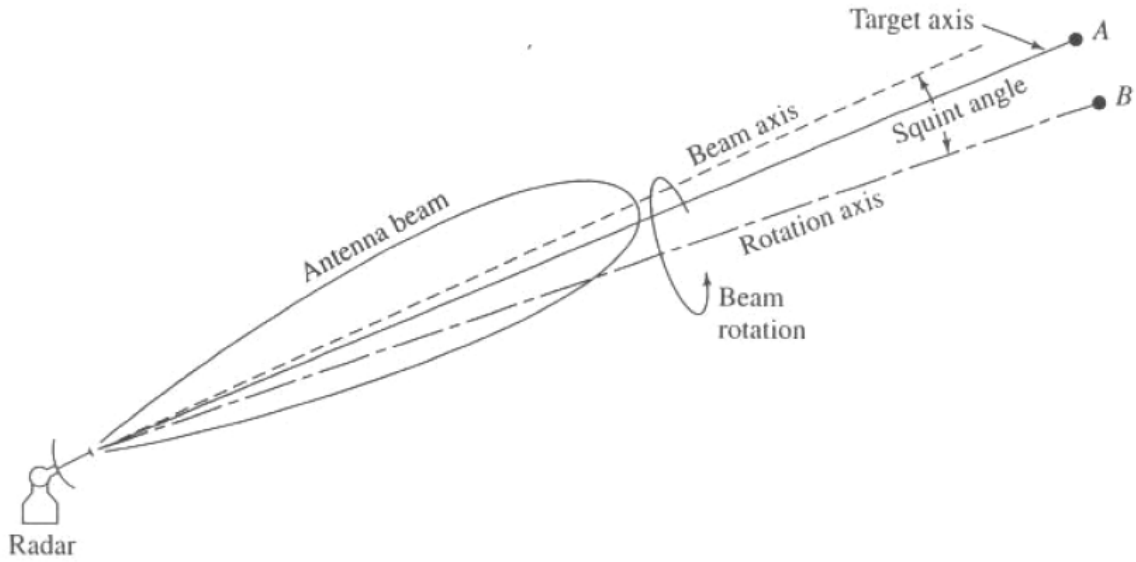
Figure 6.   Conical scan tracking (From [14]).

c.   *Monopulse Tracking*

In monopulse tracking, two or more simultaneous beams are compared to obtain the angular location of a target. The name monopulse comes from the fact that a single pulse can be used for the measurement of the angle. Since the signals received from the multiple antenna beams are simultaneous, the accuracy is improved compared to conical scan and sequential lobing, which use time-shared, single-beam tracking systems. Conical scan and sequential lobing techniques suffer degradation when the echo signal amplitude changes with time. Conversely, the accuracy of the monopulse is not affected by amplitude fluctuations of the target echo [14].

Monopulse angle measurements can be made by using two different methods. These are called amplitude-comparison monopulse and phase-comparison monopulse.

For amplitude-comparison monopulse, two antenna beams are generated at small positive and negative squint angles. By the addition and subtraction of the two

13

beams, the sum and the difference beams are obtained, respectively. For transmission, only the sum beam is used, while both sum and difference beams are used for reception. In Figure 7, an example of the two beams generated is shown, along with the sum and difference beams obtained. For tracking, the objective is to position the null of the difference pattern in the direction of the target.
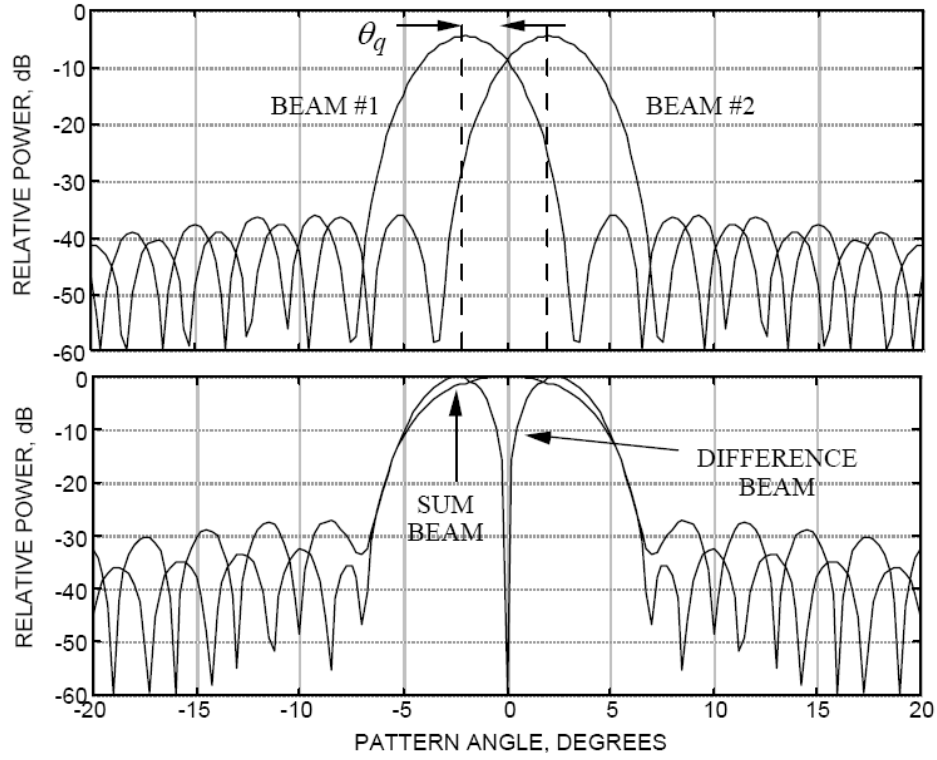
Figure 7.   Sum and difference patterns of two squinted beams (From [16]).

The direction of angle error is obtained from the comparison of the amplitude of the signal obtained from the sum beam and the amplitude of the signal obtained from the difference beam. This information can be obtained by the difference-to-sum voltage ratio, which is given as [16]

$$\frac{\Delta}{\Sigma} = \frac{\text{difference voltage}}{\text{sum voltage}}.$$

(2.1)

14

If this ratio is normalized and plotted versus the pattern angle in the vicinity of the null of the pattern, a linear region is observed, depending on the antenna beamwidth and squint angle. The plot of a typical Δ/Σ ratio is given in Figure 8.
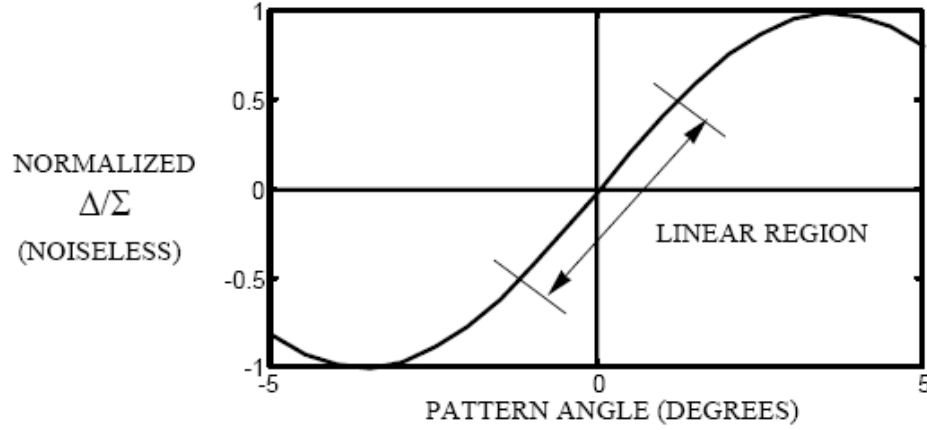
Figure 8.   Typical plot of Δ/Σ in the vicinity of the null (From [16]).

In the linear region shown in Figure 8, the Δ/Σ ratio can be approximated as [16]

$$\frac{\Delta}{\Sigma} \approx K\theta \qquad (2.2)$$

where K is called the monopulse slope constant. The monopulse slope constant can be determined from measurement or simulation.

In phase-comparison monopulse, as in amplitude-comparison monopulse, two beams are used to obtain an angle measurement. However, the two beams look in the same direction and cover the same space rather than being squinted [14]. The amplitudes of the received signals will be the same; however, the phases will be different. Hence, the measurement of the phase difference of the signals received in the two antennas can provide the angle θ to the target. This is the classical interferometer measurement.

Monopulse tracking can suffer from some errors related to noise and imperfections in the antennas used. Antenna errors include null shifting and null filling due to antenna illumination errors. Another source of error is the target glint. Glint refers to the distortion of the wavefront received from the UAV due to environmental and interference effects. If a distorted wavefront is received, the target direction calculated may differ from the actual target direction [16].

B.   ROBUST SYMMETRICAL NUMBER SYSTEM (RSNS)

The tracking techniques discussed in the previous section use amplitude or phase comparison in order to obtain the angle of a target. These techniques require the use of at least two antennas separated by a known spacing, which is referred to as the baseline. Another direction finding approach is the RSNS, which is a modular preprocessing architecture. The RSNS has been used for both analog and digital signal processing. When applied to direction finding, RSNS can provide reduced baselines and high resolution [12].

1.   RSNS Theory

The symmetric waveform that is coming out of an antenna can be mapped into a sequence of numbers as in the following [11]:

$$x_m = [0,1,2,...,m-1,m,m-1,...,2,1] \qquad (2.3)$$

where x_m is a row vector and m is an integer $(m>0)$ called the modulus. The sequence x_m is called the RSNS sequence. In an N-channel RSNS sequence, each element in x_m is repeated N times. Hence the sequence x_m takes the following form [11]:

$$x_m = \left[\underbrace{0,...,0}_{N}, \underbrace{1,...,1}_{N}, \underbrace{2,...,2}_{N}, ..., \underbrace{m-1,...,m-1}_{N}, \underbrace{m,...,m}_{N}, \underbrace{m-1,...,m-1}_{N}, ..., \underbrace{1,...,1,}_{N} \right] \qquad (2.4)$$

16

The RSNS sequence can be represented in a basic form as follows [13]:

$$\{x\} = \begin{cases} \left\lfloor \left| \dfrac{h-s_i}{N} \right| \right\rfloor, & s_i \le h \le Nm_i + s_i + 1 \\ \left\lfloor \dfrac{2Nm_i + N - h + s_i - 1}{N} \right\rfloor, & Nm_i + s_i + 2 \le h \le 2Nm_i + s_i - 1 \end{cases} \tag{2.5}$$

where h is an integer with a value $0 < h < m$ and s_i is the sequence shift value. A number system is comprised of N row vectors of different pair wise relatively prime moduli, $m_1, m_2, .., m_N$. When the row vectors are combined, they are shifted one cell per row [18].

The dynamic range $\hat{M}$ of the sequence is defined as the longest sequence of unique vectors formed in the sequence. The dynamic range is mapped into the FOV of the antenna and contributes to the angular accuracy of the sequence in tracking within that FOV. For example, if the dynamic range of a sequence is $\hat{M} = 30$ and the FOV is $180°$, the angular resolution using the RSNS sequence will be $180° / 30 = 6°$ at broadside. For a two-channel RSNS sequence with moduli m_1 and m_2, the dynamic range $\hat{M}$ can be calculated for three different combinations of m_1 and m_2 given as follows [13]:

$$\hat{M} = \begin{cases} 3(m_1 + m_2) - 6, & m_1 > 3 \text{ and } m_2 = m_1 + 1 \\ 3(m_1 + m_2) - 7, & m_1 > 5 \text{ and } m_2 = m_1 + 2 \\ 4m_1 + 2m_2 - 2, & m_1 > 5 \text{ and } m_2 = m_1 + C \ (C > 3) \end{cases} \tag{2.6}$$

The number of folds within each modulus can be found after the dynamic range is known. This is given by

$$n_i = \frac{\hat{M}}{2Nm_i}, \quad i = 1, 2, ..., N. \tag{2.7}$$

In order to achieve n number of folds, the spacing between the channels needs to be adjusted. The required spacing is found by

$$d_i = n_i \frac{\lambda}{2} \tag{2.8}$$

17

where λ is the wavelength.

When n_i folds occur in the visible region, there will be $\hat{M}$ spatial resolution bins of equal width in direction cosine space [17]. Threshold voltages have to be computed for defining the different bins for the RSNS code. There are $m_i - 1$ threshold values for each channel. The values are found by the following equation [13]:

$$V_{j,m_i} = \cos\left(\frac{m_i - j + \frac{1}{2}}{m_i}\pi\right), \quad 1 \le j \le m_i. \tag{2.9}$$

The integer value within the RSNS sequence increments when the folding waveform exceeds a threshold, and decrements when the folding waveform drops below a threshold. This process is demonstrated for a two-channel RSNS sequence in Figure 9 for moduli $m_1 = 3$ and $m_2 = 4$.
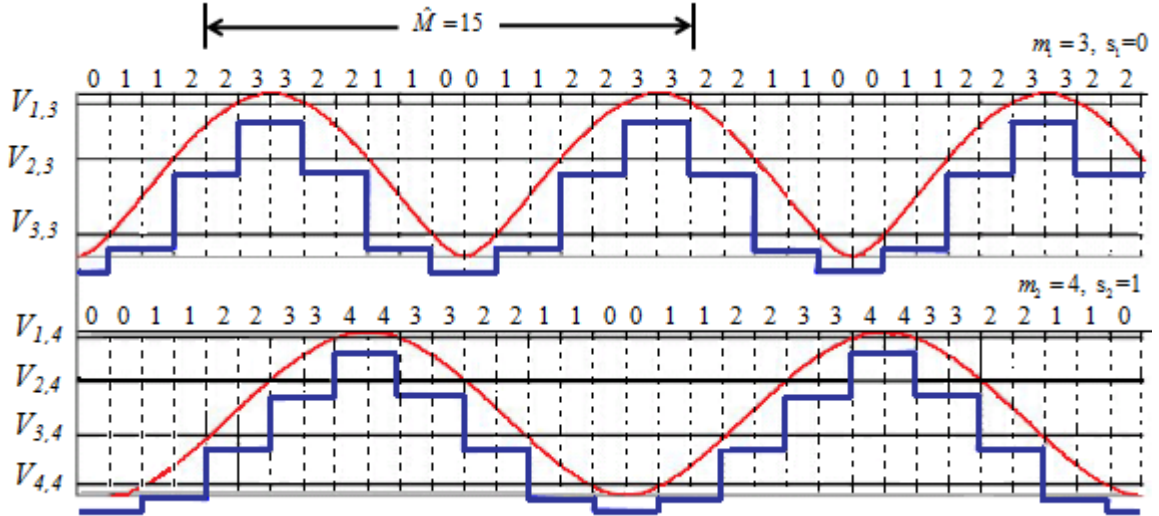
Figure 9.   Folding waveforms mapped into RSNS threshold values (After [11]).

18

The final step in developing an RSNS system is the computation of a phase adjustment term φ_i for each channel to shift the center of the dynamic range to the broadside angle of arrival. After the phase adjustment term φ_i is added, the output voltage as a function of the zenith angle (θ), wavelength (λ) and antenna spacing (d) for each channel is found as [13]

$$V_i(\theta) = \cos(kd\sin(\theta) + \varphi_i). \tag{2.10}$$

2.   RSNS Virtual Spacing

The concept of RSNS virtual spacing comes from the idea that an arbitrary folding waveform can be generated in the processor from an unambiguous measured phase difference $\Delta\phi$ [18]. The generated folding waveform is considered to arise from an imaginary spacing rather than a real spacing, therefore leading to the description *virtual*. Virtual spacing provides elimination of the limitations due to half-power beamwidth of the antenna or physical space constraints for achieving a certain channel spacing. A scale factor C is computed to translate the element spacing to the virtual spacing for each channel [13]. Using the scale factor C and the real element spacing d for a single channel, we find the RSNS virtual spacing as

$$d_i = C_i d. \tag{2.11}$$

The channel output voltages can then be found for any spacing using [17]

$$V_i(\theta) = \cos\left(\frac{Ckd}{2}\sin(\theta)\right) = \cos\left(\frac{kd_i}{2}\sin(\theta)\right) = \cos\left(\frac{C\Delta\phi}{2}\right). \tag{2.12}$$

Thus, the output voltage for an angle of arrival can be determined for any spacing d_i provided the relationship between the phase difference $\Delta\phi$ and the AOA is unambiguous. For amplitude combining, unambiguous phase difference occurs if the physical spacing d is less than one λ.

19

3.   Direction Finding Using RSNS with Moduli [5, 9]

A two-channel RSNS design with moduli [5, 9] and virtual spacing proposed in [12] was chosen by Tan and Pandya [13] for the implementation of tracking in the digital tracking array. Using $m_1 = 5$ and $m_2 = 9$ $(C = 4)$ in Equation (2.6), we calculate the dynamic range of the system as 36. For a scanning range of $-90° \leq \theta \leq 90°$, the angular resolution of one bin at broadside will be $180° / 36 = 5°$.

Using Equation (2.7), we calculate the number of folds for each of the two channels as

$$n_1 = \frac{36}{(2)(2)(5)} = 1.8 \tag{2.13}$$

and

$$n_2 = \frac{36}{(2)(2)(9)} = 1. \tag{2.14}$$

The operating frequency of the proposed system is 2.4 GHz. This gives a wavelength of $\lambda = 0.125$ m. Using $n_1 = 1.8$ and $n_2 = 1$ and $\lambda = 0.125$ in Equation (2.8), we calculate the virtual channel spacings as $d_1 = 0.1125$ m and $d_2 = 0.0625$ m, respectively.

The next step is the calculation of the scale factors for each channel. For the physical spacing of 0.065 m used in the proposed system, the scale factors are $C_1 = 1.73$ and $C_2 = 0.96$ [13]. The threshold values for the different bins can then be computed using Equation (2.9). The calculated values for the thresholds are shown in Table 1.

Table 1.   Voltage threshold values for RSNS with moduli [5, 9] (From [13]).

m/j	0	1	2	3	4	5	6	7	8
5	-0.5878	0	0.5878	0.9511	1	-	-	-	-
9	-0.866	-0.6428	-0.3420	0	0.3420	0.6428	0.866	0.866	1

The phase adjustments φ_i for Channel 1 and Channel 2 are found as $\varphi_1 = -1.2566$ and $\varphi_2 = -1.5708$ radians, respectively. These are used to align the folding waveforms to the center of the dynamic range.

The voltage of the incoming wave can be found from

$$V_i(\theta) = \cos\left(\frac{C_i \Delta\phi}{2} + \varphi_i\right), \ i = 1, 2 \tag{2.15}$$

where $\Delta\phi$ is the measured phase difference mentioned earlier, C_i is the scale factor and φ_i is the phase adjustment. For the system used in this study, the phase difference $\Delta\phi$ can be found from the in-phase (I) and quadrature (Q) data, which is obtained from the quadrature demodulator boards.

Finally, the voltages computed from Equation (2.15) are compared with the thresholds that are given in a look-up table (i.e., Table 1) and the AOA can be found.

C.   DIGITAL BEAMFORMING AND PHASE INTERFEROMETRY

For a simple linear antenna array, the wavefronts of the plane waves that arrive at each of the array elements may not be parallel to the array axis. Therefore, there will be a phase difference that occurs between each array element due to the time for the wavefront to travel between two elements. This situation is shown in Figure 10.

The phase difference $\Delta\phi$ between the elements depends on the AOA (θ), frequency and the element spacing (d) and can be calculated using

$$\Delta\phi = \frac{2\pi}{\lambda} d \cos(\theta). \tag{2.16}$$
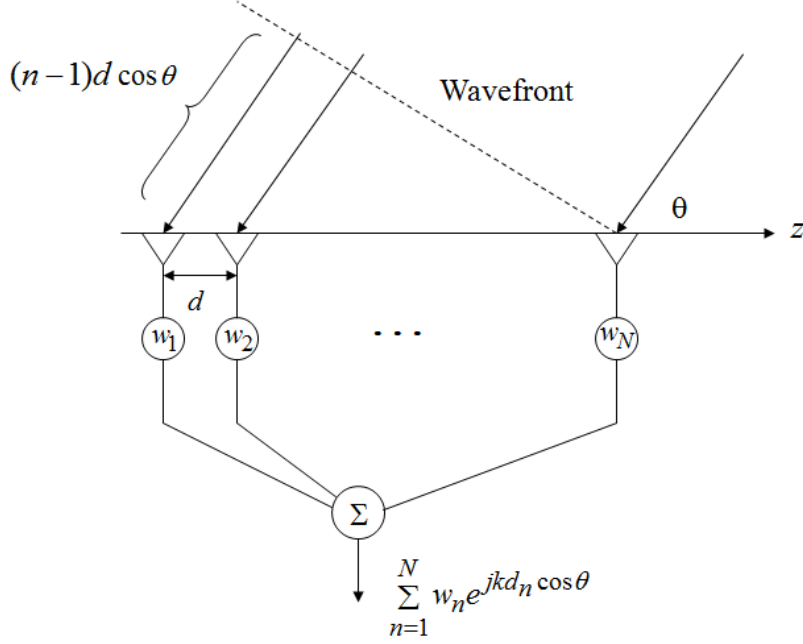
Figure 10.   Digital array beamforming on reception (From [19]).

Also shown in Figure 10 is the process of the beam-forming by the application of the weights calculated for each element and summation by the processor. The complex weight added to each array element is given by $w_n = A_n e^{j\alpha_n}$. From the addition of the weights, the sum beam array factor can be expressed by

$$AF_\Sigma(\theta,\phi) = \sum_{n=1}^{N} w_n e^{jkd_n \cos(\theta)} = \sum_{n=1}^{N} A_n e^{j\alpha_n} e^{jkd_n \cos(\theta)} \qquad (2.17)$$

where N is the number of elements, d_n is the location of element n relative to the center of the array and $k = 2\pi/\lambda$. The spacing d_n is calculated from

$$d_n = \frac{(2n - (N+1))}{2} d. \qquad (2.18)$$

In DBF, the beam is formed from the I and Q signals, which are obtained from the down-conversion and sampling of the RF signals received by the array elements. Quadrature demodulators are used to obtain I and Q signals during reception. The output of the quadrature demodulators can be represented by [19]

$$I_n = \cos\left(kd_n \cos(\theta)\right) \tag{2.19}$$

and

$$Q_n = \sin\left(kd_n \cos(\theta)\right). \tag{2.20}$$

Therefore, to obtain a response equivalent to a beam scanned in the direction θ_s, the weights must be given by

$$w_n = e^{-jkd_n \cos(\theta_s)}. \tag{2.21}$$

Thus, the sum and difference beams are obtained using

$$\Sigma \equiv AF_\Sigma(\theta, \phi) = \sum_{n=1}^{N} w_n e^{jkd_n \cos(\theta)} = \sum_{n=1}^{N} A_n e^{j\alpha_n} e^{jkd_n \cos(\theta)} \tag{2.22}$$

and

$$\Delta \equiv AF_\Delta(\theta, \phi) = \sum_{n=1}^{N/2} A_n e^{j\alpha_n} e^{jkd_n \cos(\theta)} - \sum_{N/2}^{N} A_n e^{j\alpha_n} e^{jkd_n \cos(\theta)}. \tag{2.23}$$

Using the sum and difference beams given by Equations (2.22) and (2.23), we obtain the plot given in Figure 8, and the phase error of the direction to the target can be evaluated for the linear region using Equation (2.2).

D.   SUMMARY

In this chapter, target tracking types and techniques were discussed. Monopulse tracking and RSNS for direction finding were introduced since they are used in the proposed system. Finally, digital beamforming for phased array antennas was described.

In Chapter III, the direct conversion receiver architecture will be discussed.

THIS PAGE INTENTIONALLY LEFT BLANK

III. DIRECT CONVERSION RECEIVER ARCHITECTURE

The reception process for the FM modulated video signals involves signal processing methods for the proper demodulation of the video data. The receiver architecture used in this research employs direct conversion techniques in which quadrature detection and frequency down-conversion takes place. In this section, the direct conversion receiver architecture is described and problems associated with this architecture are discussed.

A. QUADRATURE DETECTION THEORY

Quadrature detection is a common technique used for the demodulation of RF signals. The signal is demodulated to form the in-phase (I) and quadrature (Q) components of the input signal after frequency down-conversion.

In a quadrature detector, the input signal is divided into two equivalent channels as seen in Figure 11. In one channel, the signal is mixed with a sinusoidal local oscillator signal. If the local oscillator (LO) frequency is given as $\omega_{LO} = 2\pi f_{LO}$ and the input RF signal frequency as $\omega_{IN} = 2\pi f_{IN}$, the mixing process can be described mathematically as

$$
\begin{aligned}
V_{out} &= \cos(\omega_{IN}t)\cos(\omega_{LO}t) \\
&= \frac{1}{2}\Big[\cos\big((\omega_{IN} - \omega_{LO})t\big) + \cos\big((\omega_{IN} + \omega_{LO})t\big)\Big]
\end{aligned}
\tag{3.1}
$$

where V_{out} is the output voltage obtained after the mixing process. The resulting signal is passed through a low-pass filter (LPF) and the in-phase (I) component is obtained. The reason for the LPF process is to eliminate one of the terms that is created after the mixing process, usually the sum term on the right hand side of Equation (3.1). In the other channel, the input signal is mixed with a $90°$ phase-shifted version of the local oscillator signal. After low-pass filtering of the resulting signal, the quadrature (Q) component is obtained [20].
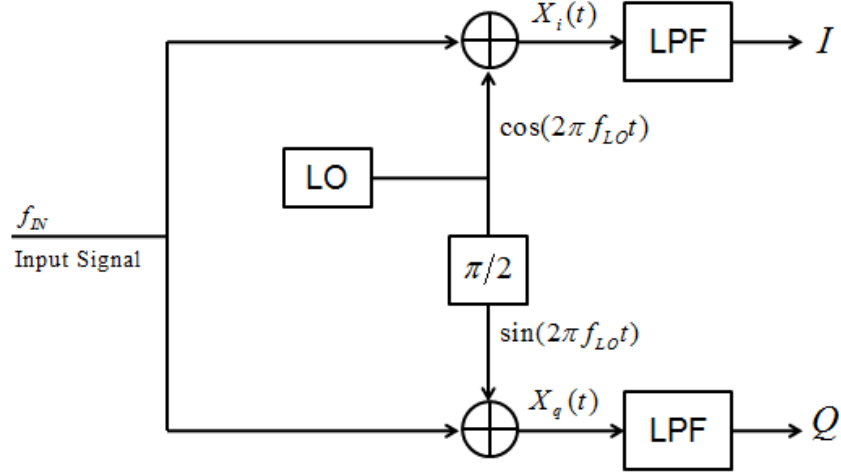
Figure 11.   Quadrature detection process (After [20]).

For the current design, an LO signal equal to the input carrier frequency $(\omega_{LO} = \omega_{IN} = \omega_0)$ is used. In the mixing process, the I and Q signals are regarded as being the real and imaginary components of a complex valued baseband signal. They can be used to observe any changes in the magnitude and phase of the input signal originally modulated onto a quadrature carrier and transmitted. This feature provides an advantage for the phase information since the direct recovery of the phase of an RF carrier sine wave is a difficult process and requires expensive hardware circuits. It is much simpler in hardware to induce a $90°$ phase shift.

The mathematical derivation of the mixing process for I and Q signals is done as follows. The in-phase baseband component can be described by [13]

$$X_i(t) = \text{Re}\left[A_c e^{j(2\pi f_0 t + \theta(t))} \right] \cos(2\pi f_0 t) \tag{3.2}$$

where $\theta(t)$ is the frequency modulated input signal. Considering a complex quantity α, we find the real and imaginary parts of α from

26

$$\text{Re}[\alpha] = \frac{\alpha + \alpha^*}{2} \tag{3.3}$$

and

$$\text{Im}[\alpha] = \frac{\alpha - \alpha^*}{2}. \tag{3.4}$$

It is convenient to use the Euler's identities for the cosine term in Equation (3.2) since it is represented with exponentials. Euler's identities are given as

$$\cos(2\pi f_0 t) = \frac{e^{j2\pi f_0 t} + e^{-j2\pi f_0 t}}{2} \tag{3.5}$$

and

$$\sin(2\pi f_0 t) = j\frac{e^{-j2\pi f_0 t} - e^{j2\pi f_0 t}}{2}. \tag{3.6}$$

Here $e^{j(\square)}$ represents the positive frequency component, and $e^{-j(\square)}$ represents the negative frequency component.

Using Equation (3.3) and (3.5), we can rewrite Equation (3.2) as

$$
\begin{aligned}
X_i(t) &= \frac{A_c\left(e^{j(2\pi f_0 t + \theta(t))} + e^{-j(2\pi f_0 t + \theta(t))}\right)}{2}\left(\frac{e^{j2\pi f_0 t} + e^{-j2\pi f_0 t}}{2}\right) \\
&= \frac{A_c}{4}\left(e^{j(2\pi 2 f_0 t + \theta(t))} + e^{j\theta(t)} + e^{-j\theta(t)} + e^{-j(2\pi 2 f_0 t + \theta(t))}\right) \\
&= \frac{A_c}{2}\left(\text{Re}\left[e^{j(2\pi 2 f_0 t + \theta(t))}\right] + \text{Re}\left[e^{j\theta(t)}\right]\right).
\end{aligned}
\tag{3.7}
$$

The leftmost component on the right-hand side of Equation (3.7) is the high-frequency component. The rightmost component on the right-hand side is the desired message signal. Hence, low-pass filtering the signal given in Equation (3.7) provides the desired message component. After low-pass filtering, the following expression is obtained:

$$I = \frac{A_c}{2}\text{Re}\left[e^{j\theta(t)}\right]. \tag{3.8}$$

In Figure 12, a frequency domain representation of the process described above is given. The real and imaginary components of the input signal are shown in the upper section, while the real and imaginary components obtained after the mixing process are

27

shown in the lower section of the figure. The single arrow lines show the multiplication with the positive frequency component, and the double dot-dashed lines show the multiplication with the negative frequency component [13]. The shaded area represents the low-pass filtered portion of the signal.

Figure 12.   Frequency spectrum for the mixing and LPF process for the I channel (From [13]).

The derivation of the quadrature component is similar to the process for the in-phase component. The quadrature baseband component can be expressed by

$$X_q(t) = \text{Im}\left[A_c e^{j(2\pi f_0 t + \theta(t))}\right] \sin(2\pi f_0 t). \tag{3.9}$$

Using Equations (3.4) and (3.6), we can rewrite Equation (3.9) as

$$
\begin{aligned}
X_q(t) &= \frac{A_c\left(e^{j(2\pi f_0 t + \theta(t))} - e^{-j(2\pi f_0 t + \theta(t))}\right)}{2}\left(j\frac{e^{-j2\pi f_0 t} - e^{j2\pi f_0 t}}{2}\right) \\
&= j\frac{A_c}{4}\left(e^{j\theta(t)} - e^{j(2\pi 2 f_0 t + \theta(t))} + e^{-j\theta(t)} - e^{-j(2\pi 2 f_0 t + \theta(t))}\right) \tag{3.10} \\
&= j\frac{A_c}{4}\left(\text{Im}\left[e^{j(2\pi 2 f_0 t + \theta(t))}\right] - \text{Im}\left[e^{j\theta(t)}\right]\right).
\end{aligned}
$$

28

Similar to the previous situation, the left-most component inside of the parenthesis in Equation (3.10) is the high-frequency component. The component on the right side is the desired message signal. Hence, low-pass filtering the signal given in Equation (3.10) provides the desired quadrature message component. After low-pass filtering, the following expression is obtained:

$$Q = j\frac{A_c}{2}\operatorname{Im}\left[e^{j\theta(t)}\right]. \tag{3.11}$$

In Figure 13, the frequency domain representation of this process is given. Again, the real and imaginary components of the input signal are shown in the upper section, while the real and imaginary components obtained after the mixing process are shown in the lower section of the figure. The single arrow lines show the multiplication with the positive frequency component, and the double dot-dashed lines show the multiplication with the negative frequency component [13]. The shaded area represents the low-pass filtered portion of the signal.
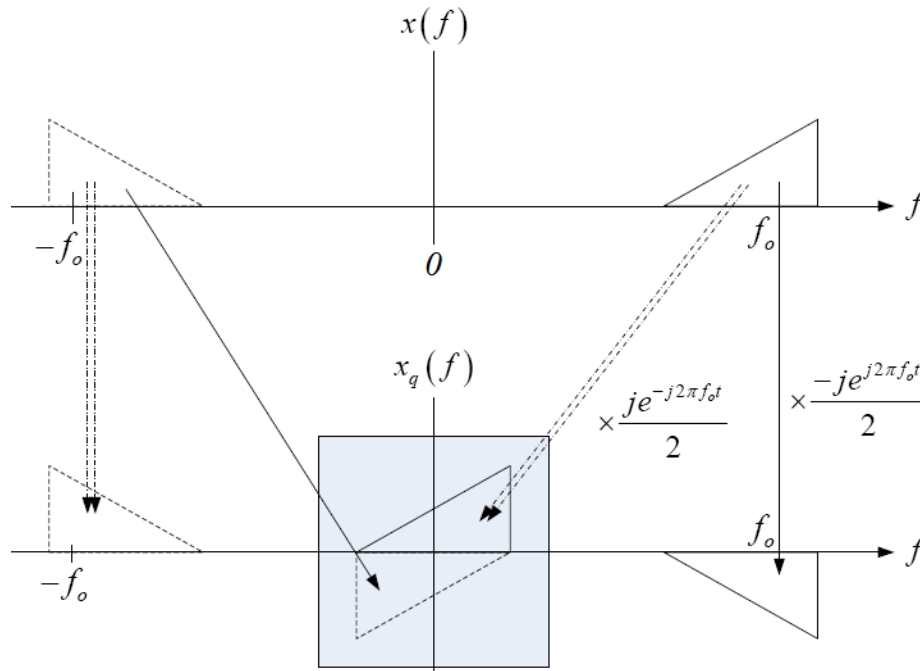
Figure 13.   Frequency spectrum for the mixing and LPF process for the Q channel (From [13]).

One important point to notice in Figures 12 and 13 is that the filtered component is the same for both I and Q channels. Hence, the amplitude of the summation of the I and Q signals is two times that of the individual components. The final output signal obtained from the summation of the I/Q signals after the down-conversion process is shown in Figure 14.
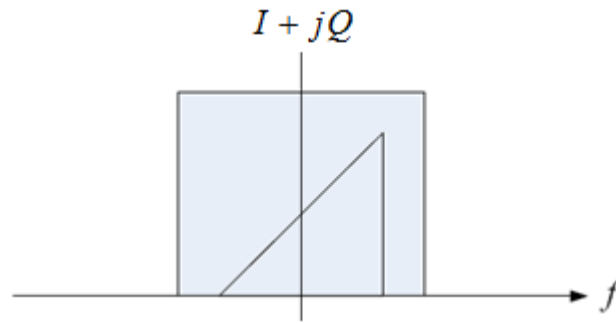
Figure 14.　　Frequency domain representation for the filtered output signal (From [13]).

B.　　DIRECT CONVERSION ADVANTAGES

Compared with other common architectures, such as the super-heterodyne architecture, direct conversion provides some advantages. In the super-heterodyne architecture, the carrier frequency is converted to an intermediate frequency before the demodulation process. This means two or more stages of detection and filtering are required. However, for the direct conversion receiver architecture, the carrier frequency is directly down-converted to baseband, where the signal can be detected and demodulated. This process requires only a single stage, which means a lower complexity and power consumption. The elimination of the intermediate frequency stages provides the ability to build these architectures with less circuitry and, hence, less cost.

Another advantage obtained from the elimination of the intermediate frequency stages is that the problem of image rejection can be solved. There are two sidebands in an RF carrier signal. These sidebands contain different information about the phase and

the frequency of the modulated signals and they need to be separated from each other. If these signals overlap each other, irreversible corruption occurs and the phase and frequency information are lost. Also, it is very expensive and difficult to design and build circuits to directly recover the phase of an RF carrier wave [13]. The direct conversion architecture eliminates these problems with the features described above and provides cost efficiency.

C.   DIRECT CONVERSION PROBLEMS

The direct conversion architecture has some problems and limitations due to several reasons, including couplings and mismatches in the circuitry used. In this section, four main problems associated with the direct conversion receiver architecture are discussed.

The quadrature detection process was illustrated in Figure 11. During this process, a finite amount of feedthrough exists from the local oscillator to the inputs of the mixer. This effect is also called "LO leakage" or "LO feedthrough" and arises from parasitic coupling of the LO and RF signals [21]. This coupling produces a dc component in the mixing process which cannot be filtered out since the RF and LO signals are in band. This problem can be solved by applying proper isolation between the RF and LO signal paths on a circuit board to prevent the leakage. Another approach is to apply a certain amount of shielding between these paths. The dc offsets may also arise from the mismatches in the I/Q demodulator. Since in a direct conversion architecture, the band of the down-converted signal extends to zero frequency, extraneous offset voltages can corrupt the signal and saturate the following stage, therefore, causing significant problems [21]. This problem can be resolved by applying a calibration routine to find the offsets. After the offsets are found, necessary adjustments can be made to compensate for the dc offsets. The calibration of the quadrature demodulators will be discussed in more detail in Chapter V.

Another problem for the direct conversion architecture is the mismatch between the amplitudes of the I and Q signals. Referring back to Figure 11, we recall that it was mentioned that the LO oscillator is shifted by $90°$ for the generation of the quadrature signal. The errors that occur in this phase shift and additional mismatches between the amplitudes and phases of the I and Q channels corrupt the down-converted signal and cause errors in the information being sent. Inspection of the complex envelope representations for the I and Q components reveals that any mismatches will create differences in the amplitudes for the in-phase and quadrature signals. The phase mismatches occur due to unequal path lengths in the two channels [13]. The problem of I and Q mismatch can be eliminated by using higher levels of integration [21].

The third problem for the direct conversion architecture arises from the nonlinearities experienced by the strong interferers in a low-noise amplifier (LNA). The mixing process of two signals was described in Equation (3.1). For direct conversion after the mixing process, the low-frequency term given on the left-hand side of Equation (3.1) is produced. This term indicates that two high-frequency interferers generate a low-frequency beat in the presence of second-order distortion. Another source of the second-order nonlinearity is the second harmonic of the desired RF signal, which is down-converted to the baseband if mixed with the second harmonic of the LO output. This may occur for higher harmonics as well, but it is negligible in differential mixers since the magnitude of the harmonics for both the RF signal and the LO signal is inversely proportional to the frequency. Second-order nonlinearities can produce unwanted components which fall within the desired band of frequencies. This situation is illustrated in Figure 15. Second-order nonlinearity can be characterized using the "second intercept point," IP_2. To obtain IP_2, two equal amplitude interferers are applied at the input and their low-frequency beat signal is observed at the output. Then, IP_2 is obtained by the extrapolation of the results after plotting the beat signal power versus the input power [21].

32
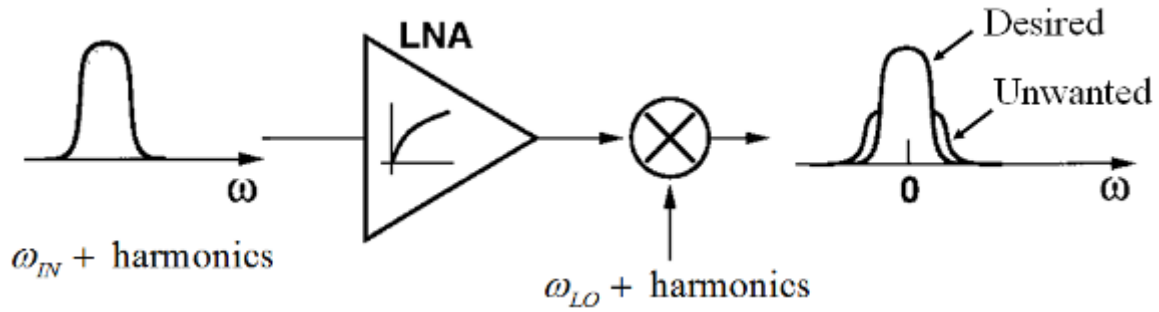
Figure 15.   Down-conversion of signal harmonics (From [21]).

The last problem that will be discussed is the potential for flicker noise. Considering a gain of roughly 30 decibels (dB) in the LNA/mixer combination in a direct conversion architecture, the down-converted signal amplitude has a range on the order of tens of microvolts. This situation makes the input noise of the following stages (e.g., filters) critical. The $1/f$ noise of devices has a profound effect on the signal because of the down-converted signal spectrum being located around zero frequency. The magnitude of flicker noise can be reduced by the incorporation of very large devices (on the order of thousands of microns) by the stages following the mixer since they operate at relatively low frequencies.

D.   SUMMARY

In this chapter, the direct conversion receiver architecture was discussed. The quadrature detection theory was introduced, and the I/Q signal down-conversion process was described. Finally, the advantages and associated problems of the direct conversion architecture were discussed.

In Chapter IV, the video signal formats will be described, followed by the modulation and demodulation techniques used for the transmission and reception of video data.

THIS PAGE INTENTIONALLY LEFT BLANK

IV. UAV VIDEO SIGNAL PROCESSING

When the acquisition and tracking of the video signal coming from a UAV are achieved, the next step is to retrieve the video data from the incoming signal. In order to retrieve the video data successfully, the structure of the incoming signal must be known. The video data, which is captured by the UAV's onboard camera, is first encoded using a particular analog video format. This encoded data is then modulated on a carrier frequency and transmitted to the GCS. After the signal is received successfully by the GCS, the signal is processed in a backwards order compared to the process before the transmission. First the signal is demodulated using an appropriate method and then the demodulated signal is decoded to retrieve the captured video data. In this chapter, the structure and formats of video signals are described in detail and the modulation, and demodulation techniques for video signals are summarized.

A. VIDEO SIGNALS

Video signals are essential parts of most applications in the world today. They are used commonly in various fields and in both military and civilian applications. Military applications include surveillance, communications and navigation. Some common civilian applications are TV broadcasting, security surveillance and gaming. Video signals can be classified into two main categories: analog and digital. Analog video is continuous in form while digital video takes on the form of several discrete values that represent the information content of the original data. Analog video is an older technology compared to digital. Digital video offers advantages in compatibility with digital equipment and signal processing methods. To date, most of the video signals transmitted through free space have been analog video signals. The most commonly used analog video format in the United States is the NTSC format. In addition to NTSC, there are the Phase Alternating Line (PAL) and Systeme Electronic Pour Avec Memoire (SECAM) formats. These formats differ in image size, line rate, frame rate and vertical

line resolution. The video data transmission to a GCS from a UAV, as considered in this research, is in NTSC analog video format as well. For this reason, NTSC analog video signals were examined in more detail.

1.   NTSC Video Signals

Standard NTSC video signal is designed to be displayed on a television screen. For this process, the incoming video signal needs to be converted to the individual pixel values of the display. This conversion is done by a scanning scheme which is called a left-to-right and top-to-bottom scan [22]. This scheme is demonstrated in Figure 16.
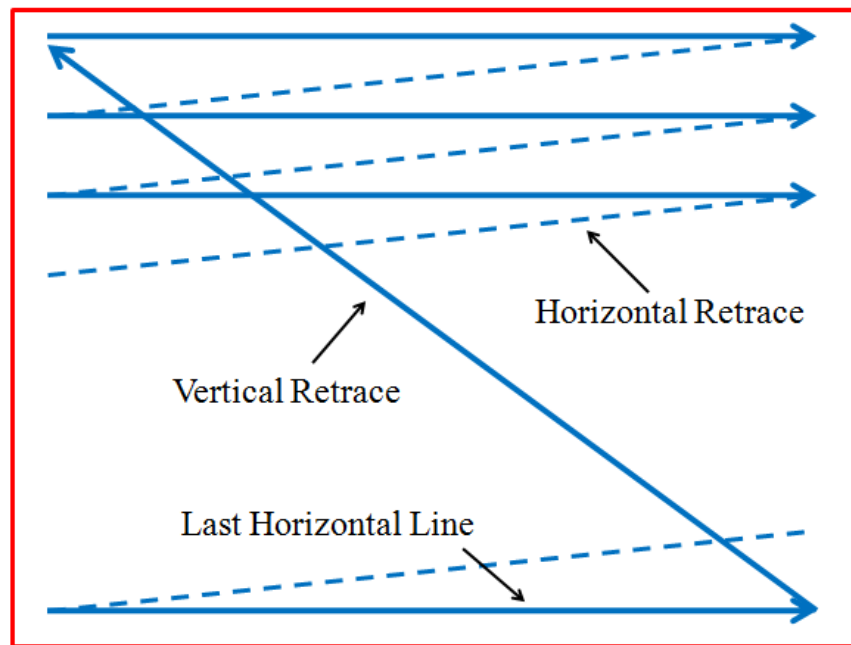
Figure 16.   Left-to-right, top-to-bottom video scanning scheme (After [22]).

In most systems today, a method called interlaced scanning is used in order to prevent the human eye from perceiving a flicker as the screen is updated at a rate of 30 frames per second. Here, the image frame is divided into two fields, one containing the odd-numbered lines and the other containing the even-numbered lines. Odd-numbered lines are scanned before the even-numbered lines, and the display is updated at a rate of

60 fields per second. The human eye cannot detect a flicker at this update rate, which is the desired result. The interlaced scanning process is shown in Figure 17.
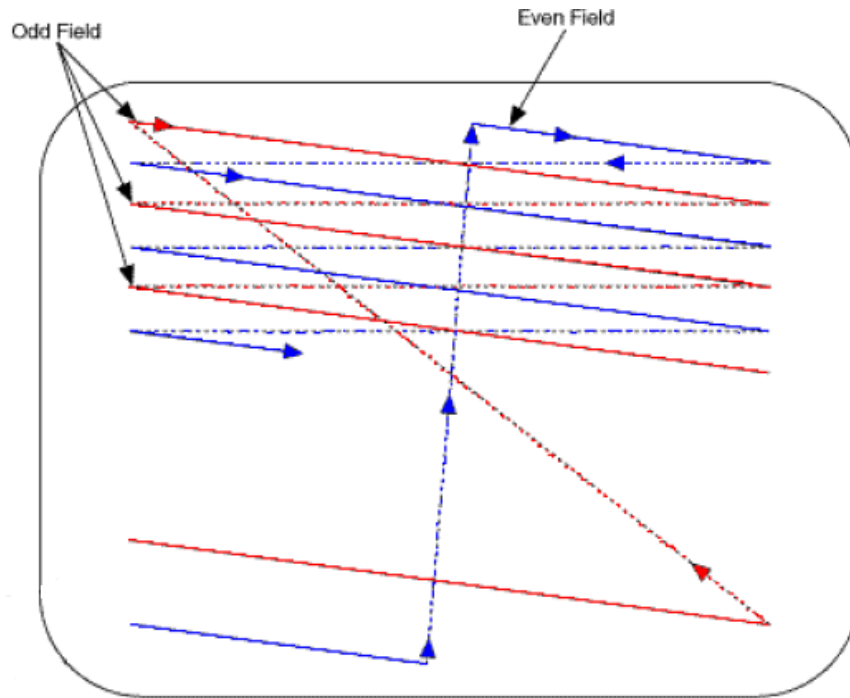
Figure 17.   Interlaced scanning process (From [23]).

The structure of a single line of an NTSC analog video signal is given in Figure 18. The components of the signal are back porch, front porch, active pixel region and horizontal sync. Back porch is used as a reference level to remove any dc components from the video signal. In the active region, the intensity information for each of the lines is represented by a low-voltage signal that is synchronized with the display device. This signal is also called the luma (luminance) signal and provides a reference for the brightness of the image. Another signal embedded within the active region of a single video signal is the chroma signal, which contains the color information of the image. The phase and amplitude reference for the color is provided by a color burst located in the video signal.

37
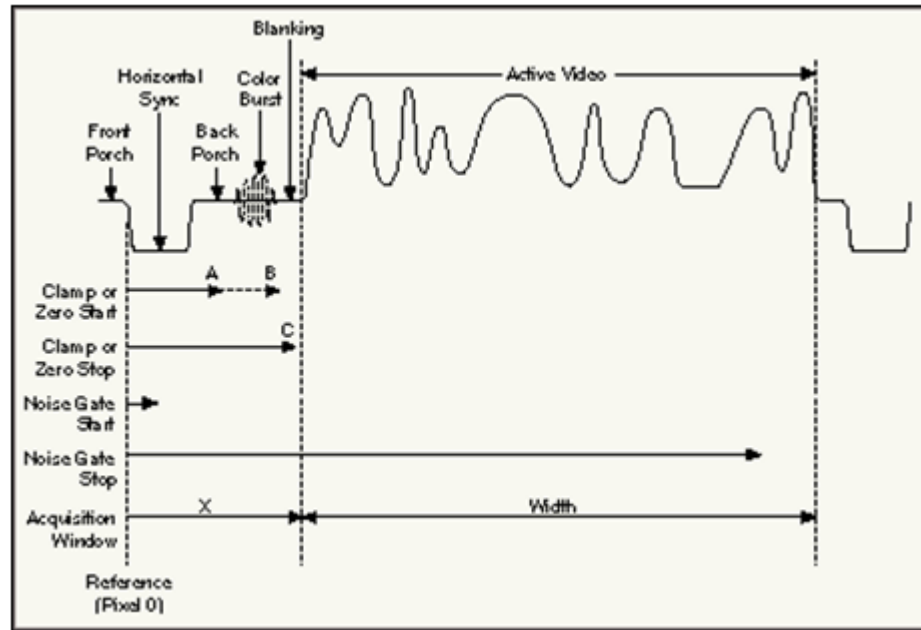
Figure 18.   NTSC analog video signal for a single horizontal line (From [22]).

There are horizontal synchronization (sync) signals at the beginning of each new video line, which indicate the next stream of pixels forming the next line. In the left-to-right top-to-bottom scanning scheme mentioned earlier, this signal dictates when the image should be scanned from left to right. The top-to-bottom scanning is dictated by the vertical sync signal. The utilization of horizontal and vertical sync signals are demonstrated in Figure 19.

As seen from Figure 19, horizontal sync signals are located between every line in a field, while the vertical sync signals are located only between the fields. Also noticed is that more than one pulse is used in vertical sync to indicate the start of a new field.
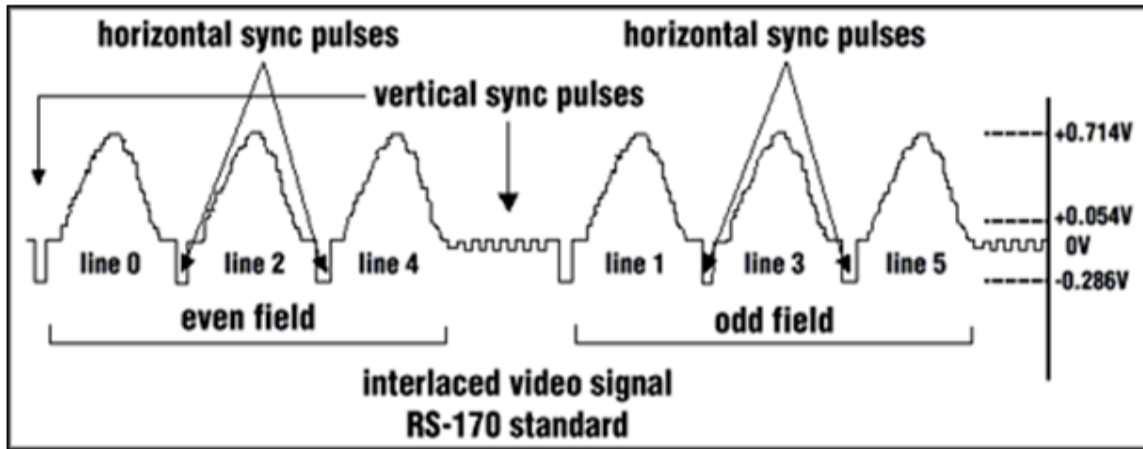
Figure 19.   Utilization of horizontal and vertical sync signals
                     in a video signal (From [22]).

2.   Video Frame Format

In NTSC analog video format , there are 525 lines per frame. Of these, 485 lines are used for display and the remaining 40 lines are used for vertical sync signals. The 485 display lines are separated into two fields with 263 lines in the first and 262 lines in the other. There are 20 vertical sync pulses at the beginning of each field, therefore making a total of 40 pulses. The line frequency for a color NTSC signal is 15,734 kilohertz (kHz). Therefore, the line duration is calculated as 63.556 microseconds (µsec). The active horizontal signal duration for the same signal is 52.66 µsec. For a better understanding of these time intervals, detailed timing of a video line is given in Figure 20.
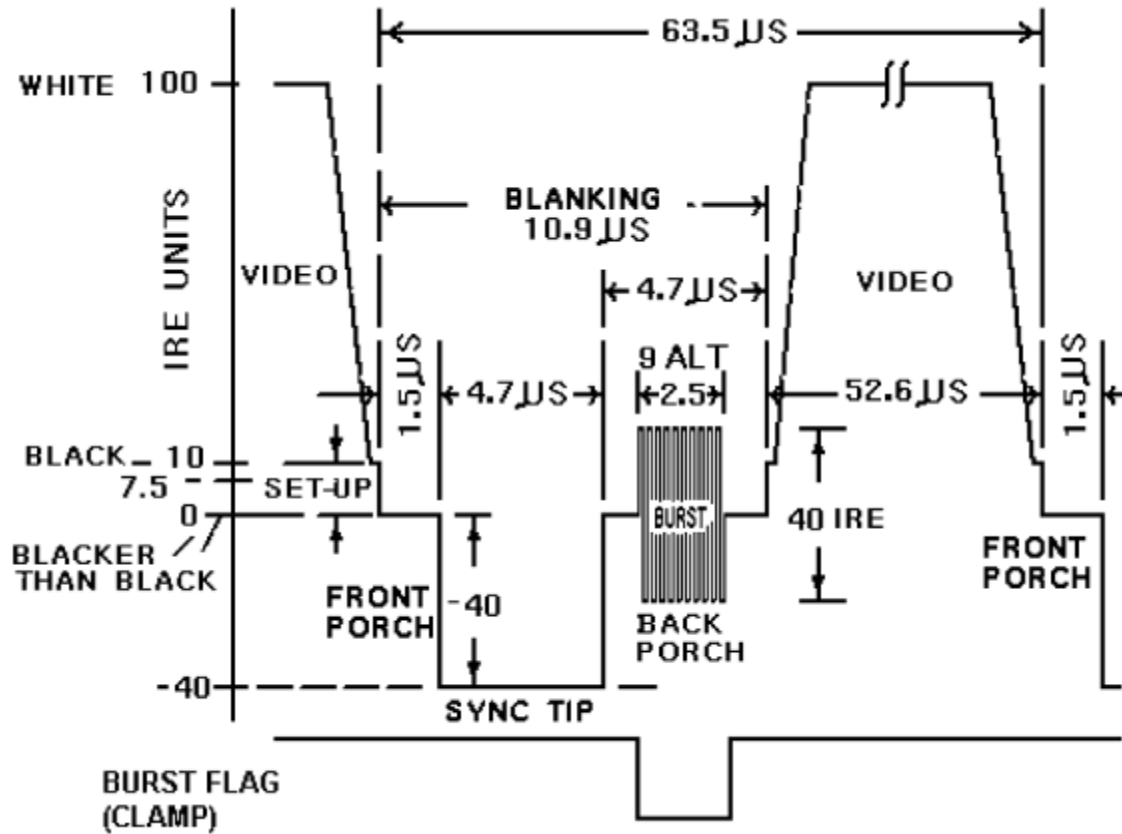
Figure 20.　　Timing of an NTSC video line (From [13])

Also seen in Figure 20 are the video levels and ranges for the different parts of the video signal. The unit used to define video levels is the IRE (Institute of Radio Engineers). The blanking level refers to 0 IRE and the white level refers to +100 IRE. The blanking level is the reference level for the video signal but it differs from the black level when a setup is applied to the signal. For NTSC, a setup of 7.5 IRE is usually applied. This moves the black level to +7.5 IRE.

3.   Digital Video Signals

Digital video signals are not used as commonly as analog video signals. However, they are chosen for applications which require high spatial resolution, high-intensity resolution, high speed and noise immunity. Because the signal is already digitized, the timing of the digital video is easier than the analog video. The timing signals for digital video are pixel clock, line enable and frame enable. These are shown briefly in Figure 21.
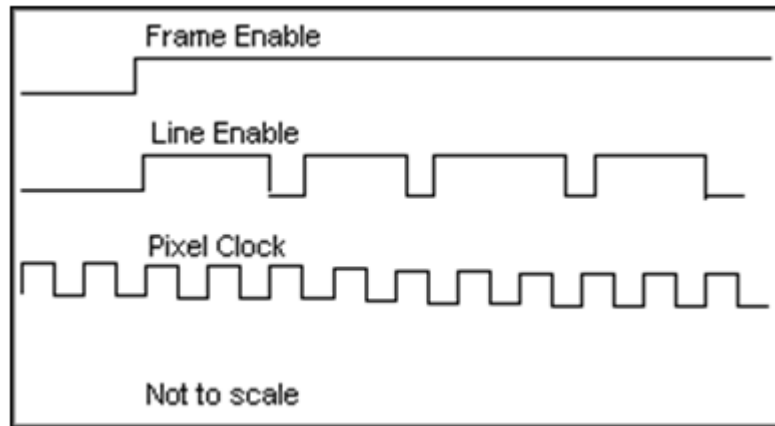
Figure 21.   Timing signals for digital video (From [22]).

The pixel clock sets the timing of the data transfer. The line enable signal indicates the beginning and end of each video data line. Finally, the frame enable signal indicates the start and completion of each frame [22].

B. VIDEO SIGNAL MODULATION AND DEMODULATION

There are three properties of an analog signal that can be changed by a message signal. These are frequency, amplitude and phase. Changing these properties of an analog signal using a message signal is called modulation. When the frequency, amplitude and phase of an analog signal are changed, the modulation is called frequency modulation (FM), phase modulation (PM) and amplitude modulation (AM), respectively. Frequency and phase modulation are also called angle modulation. Angle modulation has some advantages over amplitude modulation but there are also disadvantages. Advantages include noise reduction, improved system fidelity and more efficient use of power, while disadvantages include a requirement for a wider bandwidth and utilization of complex circuits in transmitters and receivers. Today, angle modulation is used extensively for commercial radio broadcasting, television sound transmission, two-way mobile radio, cellular radio, and microwave and satellite communication systems [24].

The video data transmission to the GCS from the UAV also utilizes FM. The video data captured by the onboard camera is first encoded and then FM modulated on a carrier before being transmitted to the GCS. When the transmitted signal is received by the GCS, it is down-converted to baseband and demodulated. After the demodulation, the resulting signal is decoded and the video is obtained. For the purpose of this thesis, emphasis will be placed on FM and its associated demodulation procedures.

1. Frequency Modulation (FM)

As mentioned earlier, frequency modulation is a form of angle modulation. In angle modulation, the instantaneous phase angle of a sinusoidal wave is varied with respect to time. Mathematically, an angle modulated wave can be expressed as [24]

$$x(t) = V_c \cos[\omega_c t + \theta(t)] \qquad (4.1)$$

where $x(t)$ = angle modulated waveform, Vc = peak carrier amplitude, $\omega_c = 2\pi f_c$ = carrier radian frequency, and $\theta(t)$ = instantaneous phase deviation (radians).

In order to achieve angle modulation, it is required that $\theta(t)$ be a function of the modulating signal amplitude. In our particular application, the NTSC video signal is the modulating signal. However, to illustrate the FM characteristics, we often consider the modulating signal as a sinusoid with amplitude V_m and frequency ω_m. It can be represented as [24]

$$s_m(t) = V_m \sin(\omega_m t). \tag{4.2}$$

FM and PM both occur at the same time and are related to each other. That is, when FM occurs PM occurs as well. The difference between FM and PM lies in which property of the carrier is directly varied by the modulating signal. If the frequency of the carrier signal is varied directly, it is called FM. If the phase of the carrier signal is varied directly, it is called PM [24].

In Figure 22, an FM modulated signal is shown in the frequency domain. The magnitude and direction of the maximum frequency shift Δf which is also known as the peak frequency deviation, is determined by the amplitude and polarity of the modulating signal V_m which is shown in the lower section of Figure 22. As shown, the frequency can vary about the carrier continuously assuming any value between $+/- \Delta f$. The rate of change of the carrier frequency is equal to the frequency of the modulating signal. The instantaneous frequency deviation is found by taking the first derivative of the instantaneous phase deviation $\theta(t)$ as

$$\Delta f = \theta'(t) \text{ rad/s} \tag{4.3}$$

where the prime $(')$ is used to represent the first derivative with respect to time.

43
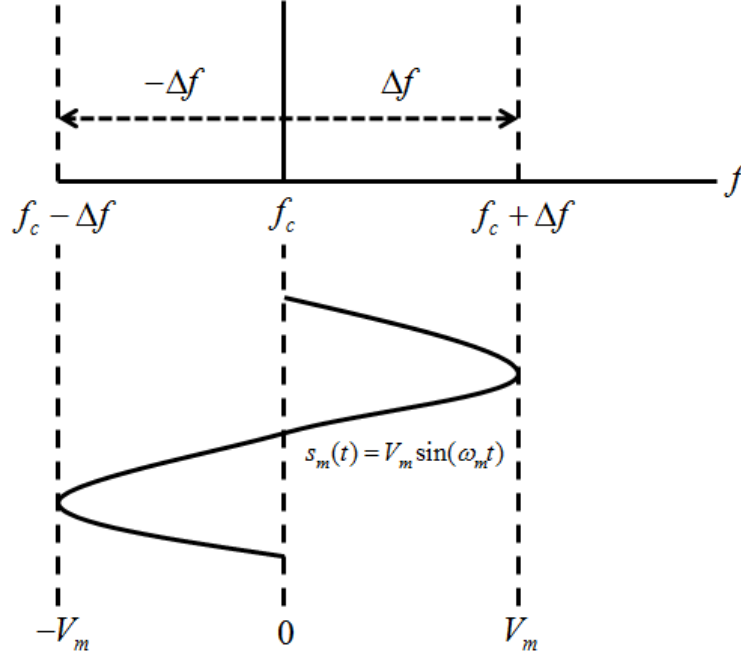
Figure 22.   Angle modulated waveform in the frequency domain (After [24]).

The frequency deviation Δf is proportional to the amplitude of the modulating signal. Therefore, it can be represented as

$$\theta'(t) = K s_m(t) \text{ rad/s} \tag{4.4}$$

where K is a constant, which is called the deviation sensitivity of the frequency modulator. The unit used for K is Hz/volt.

The ratio of the frequency deviation to the frequency of the message signal is known as the modulation index. Modulation index is a unitless quantity and indicates the depth of modulation achieved. Using Equation (4.4) for the frequency deviation, we find the modulating index from

$$m = \frac{\theta'(t)}{f_m} = \frac{K V_m}{f_m} = \frac{\Delta f}{f_m} \text{ (unitless)} \tag{4.5}$$

where m = modulation index (unitless), K = deviation sensitivity (Hz/volt), V_m = peak modulating signal amplitude, and f_m = message signal frequency.

Finally, using the relationships above, we can rewrite Equation (4.1) for an FM signal as [24]

$$x(t) = V_c \cos[\omega_c t + \frac{KV_m}{f_m}\sin(\omega_m t)]$$

$$x(t) = V_c \cos[\omega_c t + \frac{\Delta f}{f_m}\sin(\omega_m t)] \qquad (4.6)$$

$$x(t) = V_c \cos[\omega_c t + m\sin(\omega_m t)].$$

2.   FM Demodulation Techniques

With FM, the information is impressed onto the carrier in the form of frequency variations. On the receiver side, this FM signal is demodulated using one of several FM demodulation methods. FM demodulators produce an output voltage, which is proportional to the instantaneous frequency at their outputs [24]. Of interest in this thesis is the demodulation of FM modulated signals received from a UAV, with video information encoded using the NTSC format prior to modulation.

Hui [25] studied three practical implementations of the FM demodulators. These are: (1) digital phase locked loop (PLL) quadrature detector, (2) local oscillator with no feedback and (3) Billotti's quadrature demodulator.

In a PLL, a phase comparator is used to generate an error voltage signal proportional to the difference between the voltage-controlled oscillator (VCO) and the signal at the input. This error voltage is fed back to the input of the VCO. This process is repeated continuously so that the VCO can keep track of the frequency changes in the input signal. The demodulated information signal can be obtained from the output of the phase comparator since it will be proportional to the frequency deviation.

The local oscillator with no feedback has a similar structure but it lacks the feedback to the VCO. It is assumed that the FM signal can be demodulated if the local oscillator frequency and the input signal frequency are sufficiently close.

Bilotti's quadrature demodulator applies a $90°$ phase shift to the FM signal. A tuned circuit converts frequency variations to phase variations. The phase shift that occurs is greater or smaller than $90°$ depending on the direction of the frequency deviation. The output of the phase detector is applied to the input of a PM detector.

In [25], the three methods mentioned above were compared using simulations that utilized digital beamforming. It was concluded that local oscillator with no feedback showed similar performance as the other two detectors with less circuitry. Furthermore, it was found to be tolerant to the expected frequency offset between the FM transmission source and the LO. For this reason, this detector was selected for the FM demodulation process in this thesis.

The demodulation of FM modulated video signals is performed in software by the antenna processor, i.e., by digital signal processing (DSP). Three types of demodulation schemes were studied. They are: (1) baseband demodulation, (2) tangent-type demodulation and (3) demodulation using a Kalman filter. These demodulation schemes are described in the following sections.

a.   *Baseband Demodulation*

The array architecture that is employed in this research uses in-phase and quadrature components for single-stage down-conversion from RF to baseband. Assuming $x(t)$ is the received signal, we can obtain the in-phase and quadrature components as

$$
\begin{aligned}
x(t) &= V_c \cos\left[\omega_c t + \theta(t)\right] \\
&= V_c \cos\left[2\pi f_c t + 2\pi\Delta ft + \theta(t)\right] \\
&= V_c \cos\left[2\pi\Delta ft + \theta(t)\right]\cos(2\pi f_c t) - V_c \sin\left[2\pi\Delta ft + \theta(t)\right]\sin(2\pi f_c t)
\end{aligned}
\tag{4.7}
$$

where

$$I(t) = \cos\left[2\pi\Delta ft + \theta(t)\right] \tag{4.8}$$

$$Q(t) = \sin\left[2\pi\Delta ft + \theta(t)\right] \tag{4.9}$$

and $\theta(t) = K\int\limits_{-\infty}^{t} s_m(t)dt$.

Since the change in the frequency leads to a change in phase of the signal, the original signal can be retrieved by taking the first derivative of the $I(t)$ and $Q(t)$:

$$\frac{dI(t)}{dt} = -\sin\left[2\pi\Delta ft + K\int\limits_{-\infty}^{t} s_m(t)dt\right]\left(2\pi\Delta f + Ks_m(t)\right)$$

$$\frac{dQ(t)}{dt} = \cos\left[2\pi\Delta ft + K\int\limits_{-\infty}^{t} s_m(t)dt\right]\left(2\pi\Delta f + Ks_m(t)\right). \tag{4.10}$$

Finally, the message signal $s_m(t)$ is retrieved by the expression $I(t)Q'(t) - Q(t)I'(t)$. This process is shown with a block diagram in Figure 23.
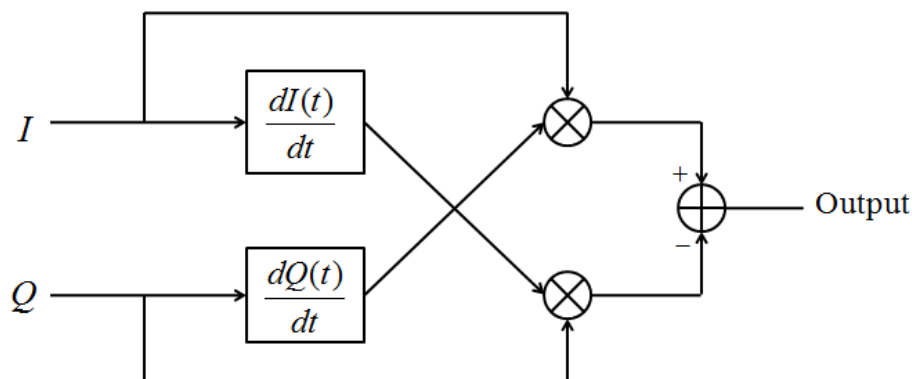
Figure 23.   Baseband Demodulation with I and Q signals.

Equation (4.10) can be obtained from a mathematical evaluation of the block diagram given in Figure 23:

47

$$I \frac{dQ(t)}{dt} - Q \frac{dI(t)}{dt} = \cos^2 \left[2\pi\Delta ft + K \int_{-\infty}^{t} s_m(t)dt \right] \left(2\pi\Delta f + Ks_m(t) \right)$$

$$+ \sin^2 \left[2\pi\Delta ft + K \int_{-\infty}^{t} s_m(t)dt \right] \left(2\pi\Delta f + Ks_m(t) \right)$$

$$= \left(2\pi\Delta f + Ks_m(t) \right) \tag{4.11}$$

$$\underbrace{\left\{ \cos^2 \left[2\pi\Delta ft + K \int_{-\infty}^{t} s_m(t)dt \right] + \sin^2 \left[2\pi\Delta ft + K \int_{-\infty}^{t} s_m(t)dt \right] \right\}}_{1}$$

$$= 2\pi\Delta f + Ks_m(t).$$

The first component $2\pi\Delta f$ in the final expression is the dc offset, which occurs as a result of the difference between the carrier frequency and the local oscillator frequency used during the down-conversion of the signal to baseband.

b.   Tangent-Type Demodulation

The tangent-type FM demodulator using DSP is shown in Figure 24. In this figure, $S_1(k)$ is the detected output of a conventional tangent-type FM demodulator. The circuit components that are used to construct this conventional tangent-type demodulator are a $90°$ phase shifter, analog-to-digital (A/D) converter, memory element, delay element, adder and subtractor [26]. The block that is shown inside the dashed lines is used for improvement of the detection range and will be described in detail in later paragraphs.
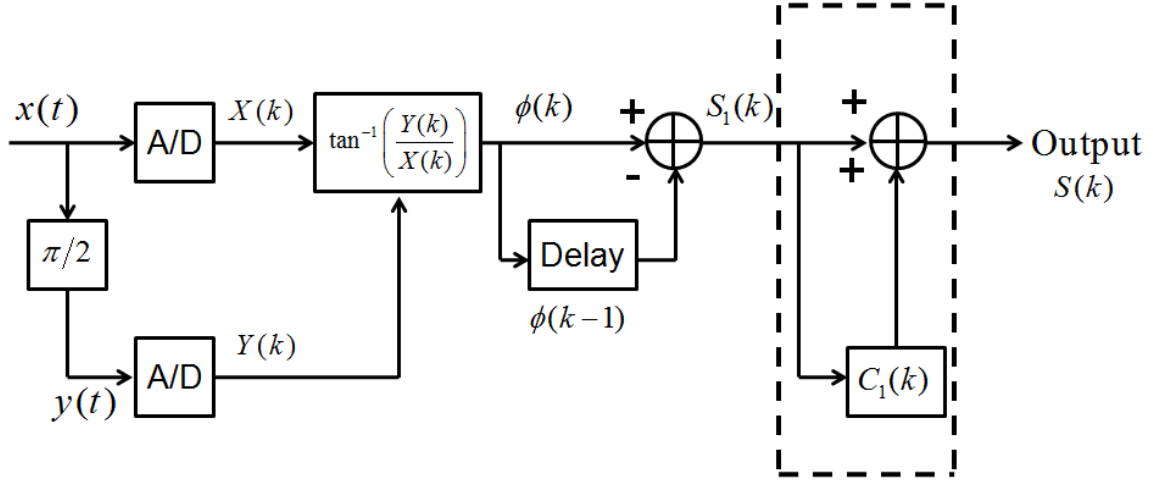
Figure 24.   Tangent-type FM demodulator using DSP (After [26]).

The input analog FM signal $x(t)$ and noise can be expressed as

$$x(t) = \sqrt{2P}\cos\left[2\pi f_c t + \theta(t)\right] + n(t) \tag{4.12}$$

where $\theta(t) = m\sin\left[2\pi f_m t\right]$, f_m = message frequency, P = signal power, and $n(t) =$ Gaussian noise. Here it is assumed that the sine wave used to represent $\theta(t)$ is actually the integral of a cosine function, which is the message signal described in Equation (4.2).

The signal $y(t)$ is obtained from passing $x(t)$ through the phase shifter. Hence ,

$$y(t) = \sqrt{2P}\sin\left[2\pi f_c t + \theta(t)\right] + n'(t) \tag{4.13}$$

where $n'(t)$ is the noise phase-shifted by $90°$. After passing through the A/D converters (i.e., sampling and quantization), the signals take the form

$$X(k) = \sqrt{2P}\cos\left[2\pi f_c kT + \theta(k)\right] + n(k) \tag{4.14}$$

and

$$Y(k) = \sqrt{2P}\sin\left[2\pi f_c kT + \theta(k)\right] + n'(k). \tag{4.15}$$

Here $t(k) = kT = k/f_s$, $\theta(k) = \theta\{t(k)\}$, $n(k) = n\{t(k)\}$, $n'(k) = n'\{t(k)\}$, T is the period of the signal and f_s is the sampling frequency.

49

The output of the phase detector is given by

$$\phi(k) = \tan^{-1}\left[\frac{Y(k)}{X(k)}\right]. \tag{4.16}$$

If we assume the noise $n(k) = 0$, this expression reduces to

$$\begin{aligned}
\phi(k) &= \tan^{-1}\left[\frac{Y(k)}{X(k)}\right] = \tan^{-1}\left[\frac{\sqrt{2P}\sin\left[2\pi f_c t + \theta(t)\right]}{\sqrt{2P}\cos\left[2\pi f_c t + \theta(t)\right]}\right] \\
&= \tan^{-1}\left(\tan\left[2\pi f_c t + \theta(t)\right]\right) \\
&= 2\pi f_c t + \theta(t).
\end{aligned} \tag{4.17}$$

Including the noise in the signal, we can write this expression as

$$\phi(k) = \tan^{-1}\left[\frac{Y(k)}{X(k)}\right] = \mathrm{mod}\left[2\pi f_c kT + \theta(k) + \eta(k)\right] \tag{4.18}$$

where $\eta(k)$ is the phase dispersion caused by the input noise, and $\mathrm{mod}\left[\,\right]$ expresses the remainder when the argument is divided by 2π [26].

Finally, the demodulated output of the tangent-type demodulator $S_1(k)$ becomes

$$S_1(k) = \frac{\Delta\phi}{\Delta t} = \phi(k) - \phi(k-1). \tag{4.19}$$

The circuit that is shown between dashed lines in Figure 24 is used to widen the detection range of the tangent-type FM demodulator. In this process, the demodulated signal $S_1(k)$ is compensated with $C_1(k)$, which is given as

$$C_1(k) = \begin{cases} 0, & S_1(k) \geq 0 \\ 2\pi, & S_1(k) < 0 \end{cases}. \tag{4.20}$$

Hence, the output $S(k)$ becomes

$$\begin{aligned}
S(k) &= S_1(k) + C_1(k) \\
&= \phi(k) - \phi(k-1) + C_1(k) \\
&= \mathrm{mod}\left[2\pi f_c T\right] + \Delta\theta(k) + \Delta\eta(k)
\end{aligned} \tag{4.21}$$

50

where $\Delta\eta(k) = \eta(k) - \eta(k-1)$. It is noticed that the first term obtained is a dc term as was the case for baseband demodulation in the previous section. The second term is the demodulated signal [26]. If the detection condition is taken as $\eta(k) = 0$, then the following condition is satisfied:

$$0 \le \mathrm{mod}\left[2\pi f_c T\right] + \Delta\theta(k) < 2\pi. \tag{4.22}$$

Thus, the improved detection range becomes $[0, 2\pi]$.

c. Demodulation Using a Kalman Filter

In [27] it is discussed that the instantaneous phase and frequency of the I and Q signals can be estimated by using a Kalman filter. State space representation is used for the estimation of the state variables. The current state is calculated as a weighted mean of the last estimated state and the current state. This means that the estimation depends on the uncertainty of the previous state and the measurement noise. For example, when a noisy measurement is done for the current state, it is expected that the influence of the previous estimated state will be higher than the measurements. For the demodulation of I and Q baseband signals, the state variables are the phase ϕ_k and the angular frequency ω_k.

In [27] it is concluded that the Kalman filter shows a significant improvement in noise performance. However, since the Kalman filter approach involves complex computations such as calculation of state vector, state uncertainty vector and covariance matrix, it is expected that it will perform slower compared to the other methods. For this reason, demodulation of FM modulated baseband signals with Kalman filtering was not implemented in the digital tracking array.

C. SUMMARY

In this chapter, the properties of analog and digital video signals were described and analog video formats were introduced. The modulation and demodulation techniques for baseband I and Q signals were discussed.

In the next chapter, the hardware and software components that are used in the digital tracking array system will be discussed.

V. ANTENNA SYSTEM STRUCTURE AND COMPONENTS

In this chapter, the general structure of the antenna system is given and the hardware and software components of the system are described in detail. The performance analyses of the commercial components are also provided.

A. SYSTEM STRUCTURE

The general block diagram of the system is given in Figure 25. As illustrated in Figure 25, the system is a combination of hardware and software components. The hardware components consist of the antenna, down-conversion block, A/D converter and the LO. The receiver architecture used is the direct conversion architecture discussed in Chapter III. The processor was implemented in the software and includes software modules for tracking, FM demodulation and decoding of the video signals. In the following sections, the functions and properties of each hardware and software component are discussed in detail.
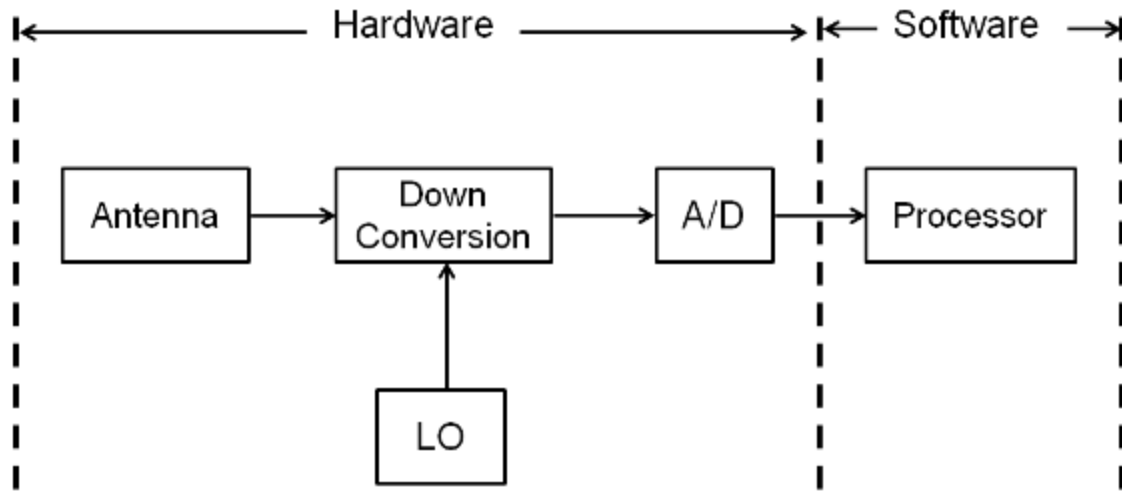
Figure 25. System generic block diagram.

B. HARDWARE COMPONENTS

The main function of the hardware portion of the system shown in Figure 25 is to receive and down-convert the analog waveform coming from the UAV and provide it to the processor as a digital signal after quantization. The incoming signal is demodulated by mixing it with a local oscillator signal that has the same frequency as the carrier signal. The mixing process provides the outputs, which were described in Equation (3.1). The high-frequency component is rejected by the low-pass filters and the low-frequency component provides the baseband envelope of the desired signal. This desired signal is then provided to the A/D to be digitized. After digitization, the resulting signal is provided to the processor block for additional signal processing, which will be discussed in later sections. The descriptions of the hardware components are provided in the following sub-sections.

1. Antenna

The array consists of six two-element subarrays over a ground plane. An image of the array is shown in Figure 26.
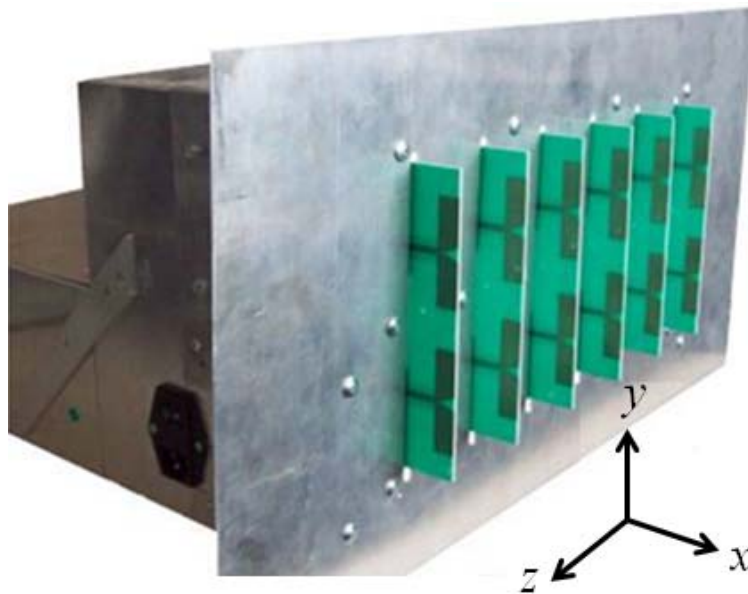
Figure 26.   Image of the phased array antenna.

Each subarray was fabricated from a Rogers RO4003C substrate and consists of two half-wave dipole antennas stacked in the elevation plane for increased directivity. The two-element structure provides a higher signal level at the input of the demodulator, therefore, allowing longer range operation. The dipole arms are fed by power splitters, as shown in Figure 27.
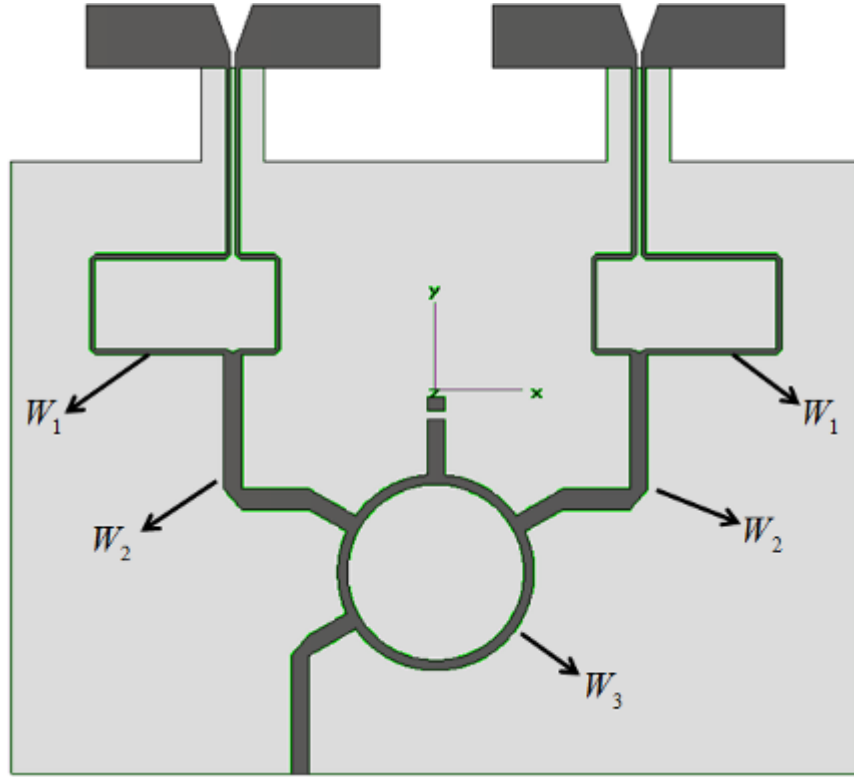
Figure 27.   PCB layout of the two element subarray (After [13])

In order to keep the current on the two arms of each dipole in phase with each other, a $180°$ phase shift is applied to one of the arms of the splitter. This is done by making one arm $\lambda/2$ longer than the other. The width W of the microstrip lines is an important parameter in terms of the operation of the dipoles. In [13], a MATLAB program is provided for the calculation of the widths used in the printed circuit board (PCB) of each subarray. The widths used in the subarrays are given in Table 2, along with some other microstrip circuit parameters.

Table 2.   Properties of the PCB layout of the two-element sub arrays (From [13]).

Dielectric constant (ε_r)	3.38
Thickness (d)	60 mils (1.52 mm)
Trace width of the $180°$ splitter (W_1)	35.7 mils (0.91 mm)
Line width of the rat-race hybrid feed lines (W_2)	139 mils (3.53 mm)
Line width of the rat-race hybrid (W_3)	76.3 mils (1.94 mm)

The approximate gain of a single subarray can be calculated by multiplying the gain of a single dipole by a factor of $2 \times 2 = 4$, to include the fact that there are two dipoles and the contribution from the ground plane image. Hence, the gain of each subarray is found to be

$$G_{subarray} = G_{dipole} \times 2 \times 2 = 6.56 = 8.17 \text{ dB} \tag{5.1}$$

where $G_{dipole} = 1.64 = 2.15$ dB [28]. The gain of the antenna subarrays was measured by Tan and Pandya [13] in an anechoic chamber by using a Narda 645 standard gain horn antenna as the reference antenna. The gain of the two-element subarray was estimated to be around 10 dB, which is sufficiently close to the calculated value in Equation (5.1). Tan and Pandya also provide simulations of the pattern of a subarray in CST Microwave Studio.

The gain of the whole array can be obtained by multiplying the gain of a single subarray by the total number of subarrays, which is six. Hence, using the result obtained in (5.1), the gain of the array is found as

$$G_{array} = G_{subarray} \times 6 = 6.56 \times 6 = 39.36 = 15.95 \text{ dB}. \tag{5.2}$$

The gain pattern of the six-element array is shown in Figure 28. It is observed that the measured gain is two decibels lower than the calculated value. This difference is considered to occur because of the cable losses from the output of the antenna to the network analyzer used to measure the received power [13]. The asymmetrical pattern is due to the chamber layout, which is also asymmetrical.
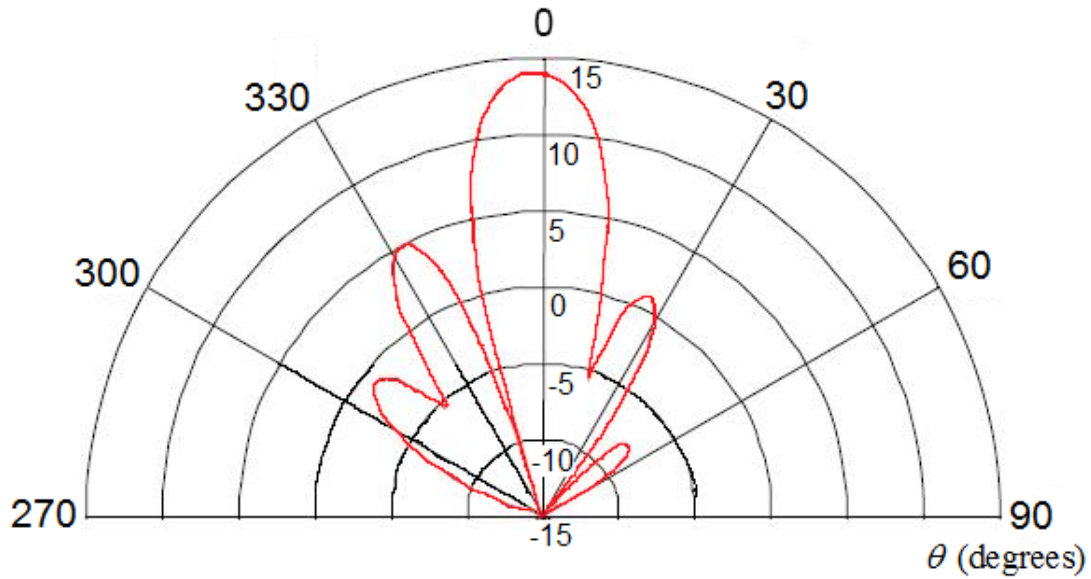
Figure 28.   Measured azimuth gain pattern of the six-element array (From [13]).

2.   Down-conversion Block

The block diagram of the down-conversion process is shown in Figure 29. The input signal coming from the antenna is down-converted into baseband I and Q signals as the outputs. Three main components are used within the down-conversion process: (1) the low-noise amplifier (LNA), (2) the quadrature demodulator and (3) a differential amplifier. These components are discussed in the following sub-sections.
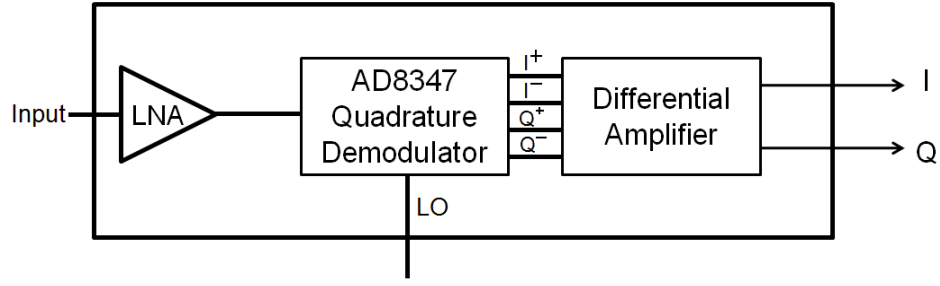
Figure 29.   Down-conversion block detailed block
diagram of an array channel.

a.   *Low-Noise Amplifier (LNA)*

One of the key factors in achieving superior sensitivity in receiver systems is to have a low noise figure. Devices such as amplifiers add noise to the signal. When there are N devices in cascade, the noise figure of the overall system is calculated as [29]

$$F_{overall} = F_1 + \frac{F_2 - 1}{G_1} + \frac{F_3 - 1}{G_1 G_2} + \cdots + \frac{F_N - 1}{G_1 G_2 \cdots G_N} \qquad (5.3)$$

where F_n and G_n are the noise figure and gain of the nth $(1 \leq n \leq N)$ component, respectively.

As is seen from Equation (5.3), the first element in the system has the biggest contribution to the noise figure since it does not have a gain factor in the denominator. The purpose of an LNA in a receiver system is to decrease the overall noise figure. This can best be achieved by placing the LNA at the front end of the receiver so that the noise contributions of the subsequent devices are much lower.

The LNA used in the system is the LNA-2700, which is produced by RF Bay Inc. The LNA-2700 has a low noise figure (1.7 dB) and high gain (23 dB). The operating frequency of the LNA-2700 ranges from 2.2 GHz to 3.2 GHz, which is consistent with the receiver system used. The LNAs are located as close as possible to the antenna elements in order to prevent cable losses and reduce mismatch.

b.　　*Quadrature Demodulator*

The quadrature demodulator used in the system is the AD8347 Direct Conversion Quadrature Demodulator integrated circuit (IC) by Analog Devices. Quadrature demodulators are used in the receiver system in order to down-convert the RF signal received by the antenna to baseband frequencies. A simplified diagram of this process is illustrated in Figure 30. The baseband I and Q signals are then sent to the A/D converters.
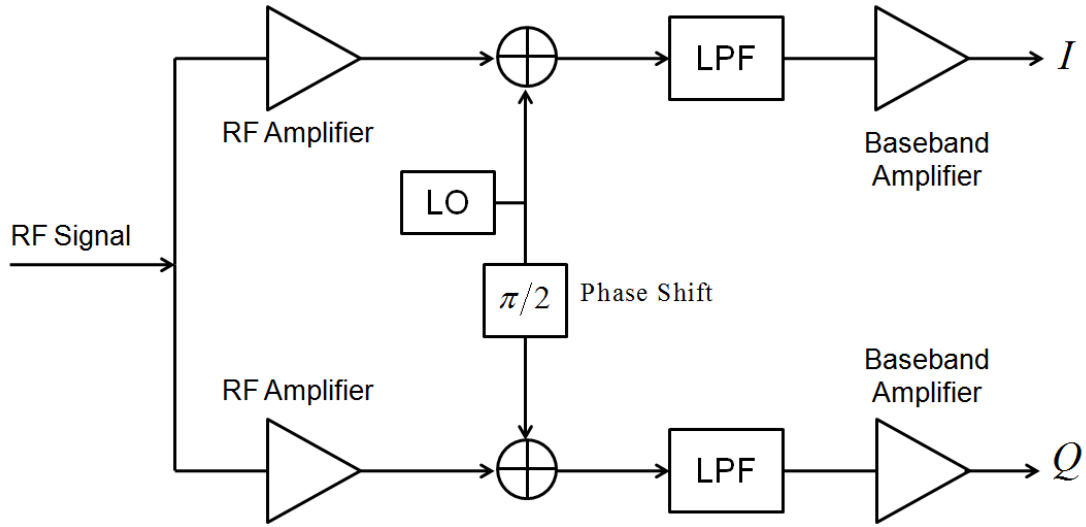
Figure 30.　　Quadrature demodulator operation block diagram.

As mentioned in Chapter III, the high-frequency components that are created from the mixing process are rejected by the filters and the baseband signals are passed. Baseband amplification is also performed.

From Figure 29, it can be seen that the AD8347 Direct Conversion Quadrature Demodulator IC produces four differential outputs, which are indicated as I$^+$, I$^-$, Q$^+$ and Q$^-$. This gives rise to the requirement that four ADCs are required for further signal processing. However, this requirement is eliminated by using the differential amplifiers described in the next sub-section.

An important issue with regard to the quadrature demodulators is that they have a dc voltage offset which affects the accuracy of the I and Q voltages. An automated calibration process was developed in [30] in order to find this offset. The calibration is done by a LabView program that uses the NI PXI-5112 digitizers on the NI PXI-1044 chassis. The PXI-5112 digitizers also need to be internally calibrated using a LabView calibration program distributed by National Instruments (NI).

In the demodulator calibration process, a loop in which the RF phase is shifted by $10°$ within the range $[0°, 360°]$ is executed by the LabView program. The phase shifts are introduced by using an AD8346 modulator board. It is required that the AD8346 modulator and the AD8347 demodulator should be frequency synchronized during the calibration process. For this purpose, the Vaunix Technology Lab Brick LSG-402 signal generator is used. The signal out of the LSG-402 is provided to the LO inputs of the AD8346 modulator and the AD8347 demodulator via a power splitter.

After the phase-stepping loop is executed, the I/Q plot, which is also known as the I/Q circle, is generated using the values obtained at each $10°$ phase shift. The dc offsets are calculated as the offset values that are required to center the I/Q circle at zero.

In Figure 31, the user interface of the LabView calibration program is shown. The user interface has an LO control section that is used to set the necessary parameters (e.g., frequency, power) of the LSG-402 signal generator. As outputs, the user interface displays information about the calibration process, such as the PXI-5112 digitizer calibration progress status, instantaneous I and Q signal plots, the calculated offset values and plots of the I/Q circles. Both the uncalibrated and calibrated (i.e., centered to zero) I/Q circles are displayed (on the upper and lower right of the screen, respectively) in the program. Examples of these plots are also shown in Figure 32.

60
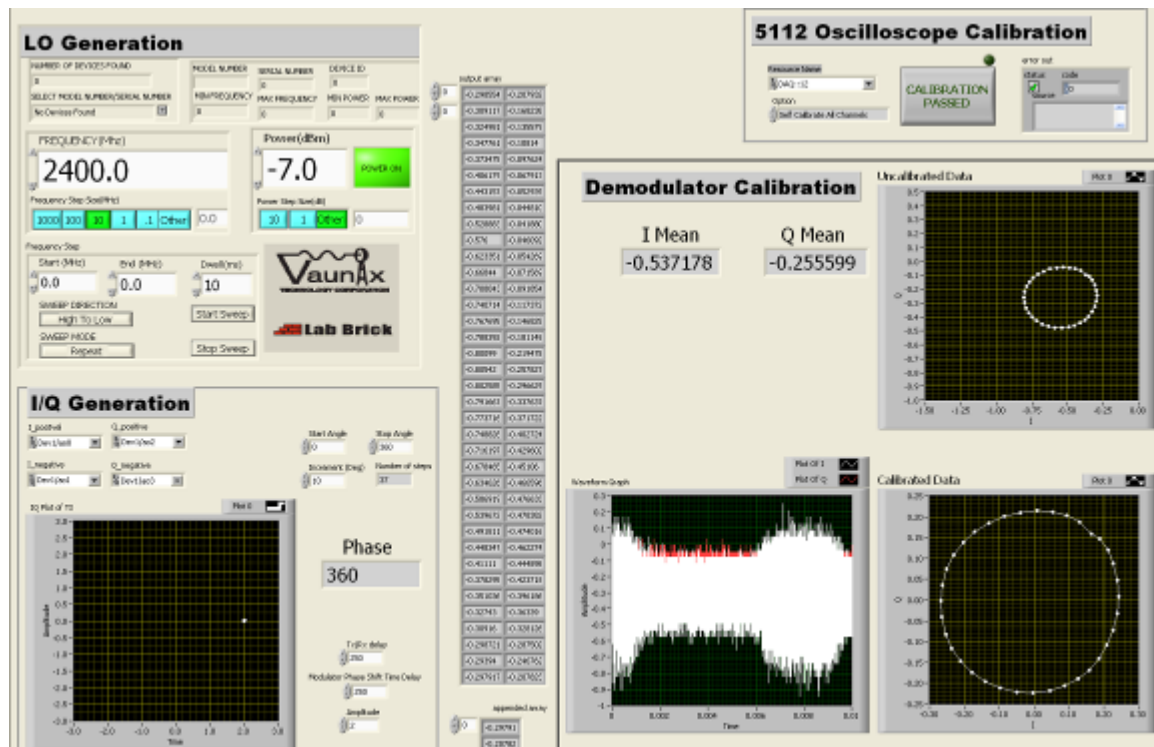
Figure 31.   LabView automated dc offset calibration program user interface.
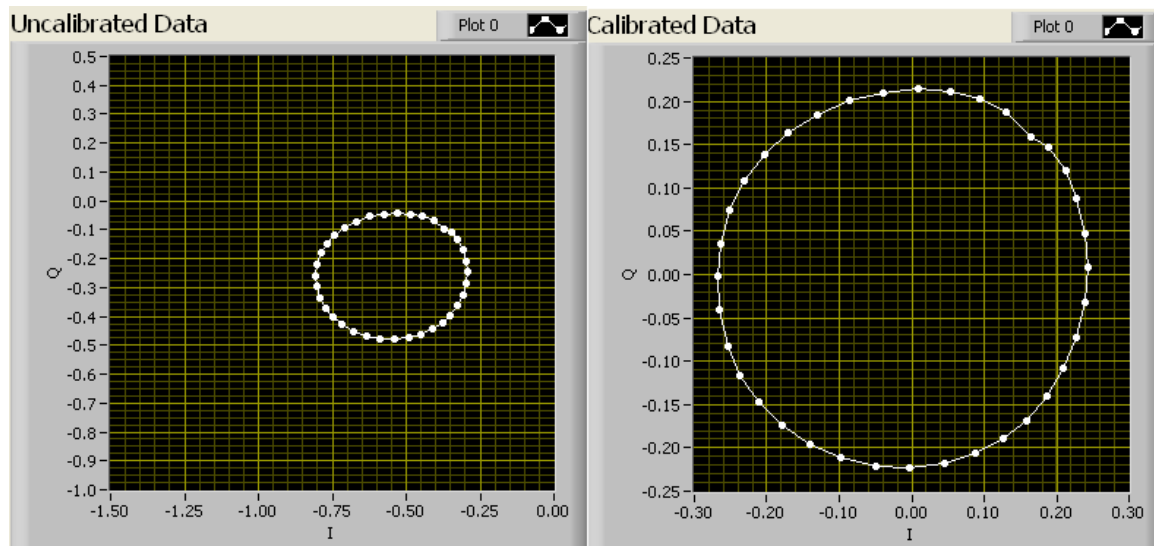
Figure 32.   Uncalibrated (left) and calibrated (right) I/Q circle plots.

61

c. *Differential Amplifier*

The differential amplifier block is built on the operational amplifier (Op-amp) chip LM622 from National Semiconductor. The differential amplifier is composed of three main stages, which have different functions and provide different advantages.

As mentioned previously, using the four differential outputs from the AD8347 quadrature demodulators would require four ADCs for further signal processing. The first stage of the differential amplifier block converts the four differential outputs of the quadrature demodulators into two outputs by combining I^+ with I^- and Q^+ with Q^- using [10]

$$I = I^+ - I^-$$
$$Q = Q^+ - Q^-.$$

(5.4)

Thus, the required number of ADCs is reduced as well as the cost to build the circuit.

The second stage of the differential amplifier block provides a voltage gain of 10 dB to the baseband signal. The third stage includes a low-pass filter that contributes to the elimination of the high-frequency components produced during the down-conversion process. The 3-dB cutoff frequency of the filter was chosen as 10 megahertz (MHz) in accordance with the bandwidth of the NTSC video signal, which is 6 MHz.

3. Local Oscillator (LO)

The LO provides a signal source to the quadrature demodulators during the down-conversion process. The LO used in the antenna system is the Lab Brick signal generator (LSG-402) by Vaunix Technology Corporation. In Figure 33, the connection between the device and the quadrature demodulator board is shown. The Lab Brick signal generator has a frequency range between 1000 and 4000 MHz, which makes it suitable for use in the antenna system. The device also has the capability to provide an

output level up to 20 decibels per miliwatt (dBm). The power and control of the device is provided by a Windows-based computer using a Universal Serial Bus (USB) port.

Figure 33.   LO (Lab Brick signal generator) connected to the
quadrature demodulator.

4.   A/D Converter

National Instruments PXI-5112 high-speed digitizers are used as A/D converters in the receiver system. The PXI-5112 uses a high-speed Peripheral Component Interconnect (PCI) bus, and therefore provides acquisition and processing of waveforms at higher speeds compared to General Purpose Interface Bus (GPIB)-based devices.

Nyquist's sampling theory states that the sampling frequency of a signal must be at least twice that of the highest frequency component. The PXI-5112 A/D converters provide a sampling rate up to 100 MS/s (mega samples per second), which means that signals with frequencies up to 50 MHz can be acquired without aliasing.

Another important feature of the PXI-5112 is that it has 8-bit resolution with an adjustable voltage range (0 to 10 V). This means that $2^8 = 256$ different levels can be used for the quantization of an analog signal. Hence, it provides lower quantization noise and high sensitivity compared to lower resolution A/D converters.

C.   SOFTWARE COMPONENTS

The block diagram of the receiver system was shown in Figure 25. It was mentioned that most of the signal processing is done with software. In order to receive video data successfully from a UAV, the UAV signals should be tracked and the video data within the received signals should be retrieved. The software portion of the system shown in Figure 25 includes software modules, which have specific functions for this purpose. The modular approach was used for the development of the software components in order to make testing and further development of the system easier. Each module can be upgraded separately or replaced by new versions in the future.

The software components consist of three software modules, which were implemented according to the principles that were discussed in Chapters II, III and IV. These modules are namely: (1) Tracking module, (2) FM demodulation module and (3) NTSC decoding module. Since these modules were developed using NI LabView software, familiarity with the LabView programming environment is necessary. In this section, the LabView programming principles are briefly introduced and the implementation of the software modules discussed. The testing of the modules is discussed in Chapter VI.

1.   NI LabView Software Overview

NI LabView is a graphical programming environment that is used to develop sophisticated engineering applications. It is crucial to understand the basic structure and principles in LabView since most of the signal processing in the receiver system was created in LabView programming environment.

Programs in LabView are developed using intuitive graphical icons and wires that resemble a flowchart. Programs created using LabView are called virtual instruments (VIs). This is because the appearance and operation of these programs imitate physical instruments. The VIs in LabView contain two main components: the front panel and the block diagram. The front panel is the user interface of the VI. The controls and indicators are implemented in the front panel. After building the front panel, graphical representations and functions are used to add code to control the objects in the front panel. This graphical code is built in the block diagram. An example of a VI front panel and the corresponding block diagram is shown in Figure 34.
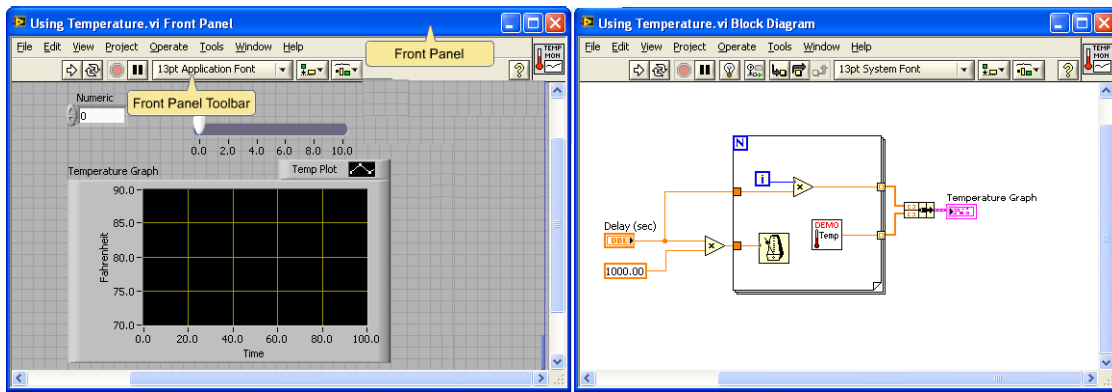
Figure 34.   VI front panel (left) and block diagram (right).

As the block diagrams get filled with several function blocks, it becomes hard to follow the algorithm. This problem can be eliminated by creating VIs that are used within other VIs. These kinds of VIs are called subVIs. SubVIs make the programs more modular and more understandable. It is important to understand the terms "VI", "subVI", "front panel" and "block diagram" since they will be used frequently in further sections.

2.   Tracking Module

The principles of tracking in phased array antennas were discussed in Chapter II. The tracking module used in the receiver system is an implementation of the RSNS and DBF. The design of the tracking module was made by Tan and Pandya [13].

Two separate DBF methods were implemented in the tracking module. The first method utilizes RSNS for tracking. The RSNS system with moduli [5, 9], which was described in Section B.3 of Chapter II, was implemented. This RSNS sequence provides a dynamic range of 36 bins and a resolution of $5°$ at broadside. The second method uses RSNS to obtain an initial scan angle and then utilizes monopulse DBF for target tracking.

In order to start tracking, the signal that is of interest needs to be acquired. This acquisition involves the calculation of the initial scan angle. It was mentioned in Chapter II that for monopulse tracking, both sum and difference beams are used during reception. If the target is not located at the boresight of the antenna, the difference beam output will be non-zero. Hence, an error signal can be obtained by using the slope of the linear region of the difference beam. In [13], the maximum initial scan angle that can be used for efficient use of monopulse DBF was calculated by computing the angular range of the linear region in MATLAB. It was observed that the linear region has a span of approximately $20°$. Hence, it was concluded that the initial scan angle must not be greater than $20°$ off from the true direction of the signal. Since RSNS provides an angular resolution of $5°$, it can be used for finding the initial scan angle before monopulse DBF is used for tracking.

The process flowchart of the tracking module is shown in Figure 35. The output of the demodulator boards are sampled by the PXI-5112 A/D converters. Since there are six array elements, there are six PXI-5112s and, hence, six array channels. Each PXI-5112 board has two data channels (channel 0 for *I* data and channel 1 for *Q* data). One of these boards is selected arbitrarily as the master, in order to act as a reference triggering. The other boards are called slaves. This is done to ensure that the data sampled from each channel is correlated. In Figure 36, a portion of the VI block diagram that is used for this process is shown.
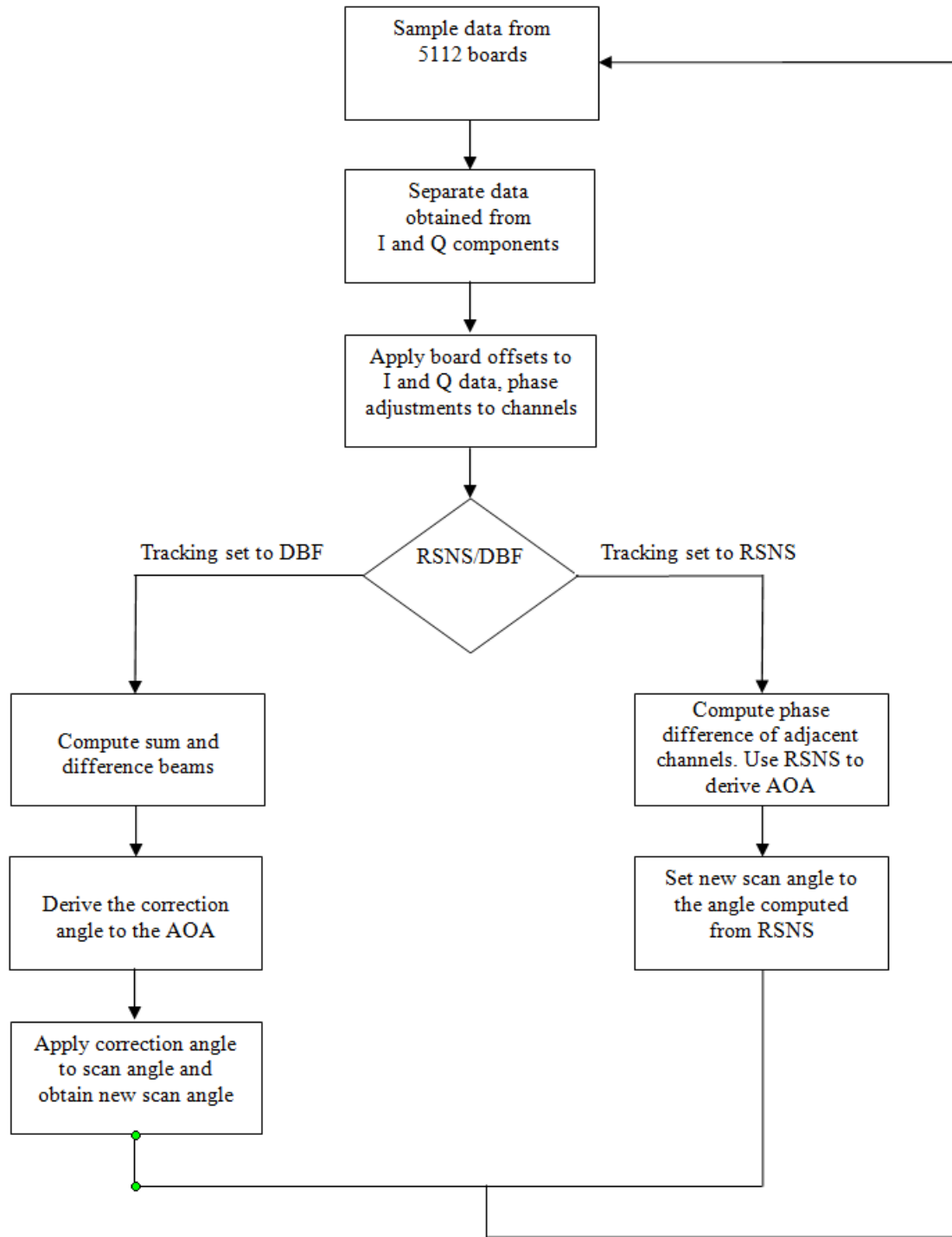
Figure 35.   Tracking module process flow chart (After [13]).
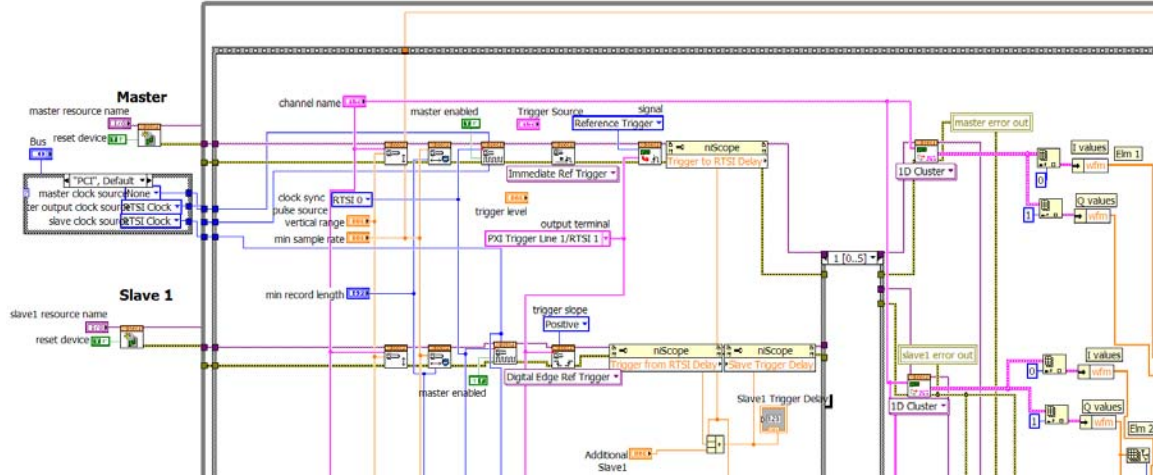
Figure 36.   Data acquisition from demodulator boards by the PXI-5112 board.
(Only the master and a single slave channel shown.)

In the next step, the individual I and Q components are separated and each board's dc offsets are applied. This process removes any dc offset that is introduced by the quadrature demodulators. The application of the dc offsets in the software is shown in Figure 37 for two array channels. The board dc offsets are calculated with the AD8347 calibration software.

After the offsets are applied, a calibration process needs to be conducted in order to account for the phase differences between the RF portions of the array channels. Ideally, when a plane wave is incident normal to the array elements, it is expected that each channel will have the same phase value. However, the test conducted in [13] revealed that the channels did not have the same phase values. This was attributed to variations in the phase of the connectors and the RF cables used. As a result, the phase differences between the channels need to be adjusted by measuring each channel relative to a common phase reference. The differences are removed in the digital beamforming.

68
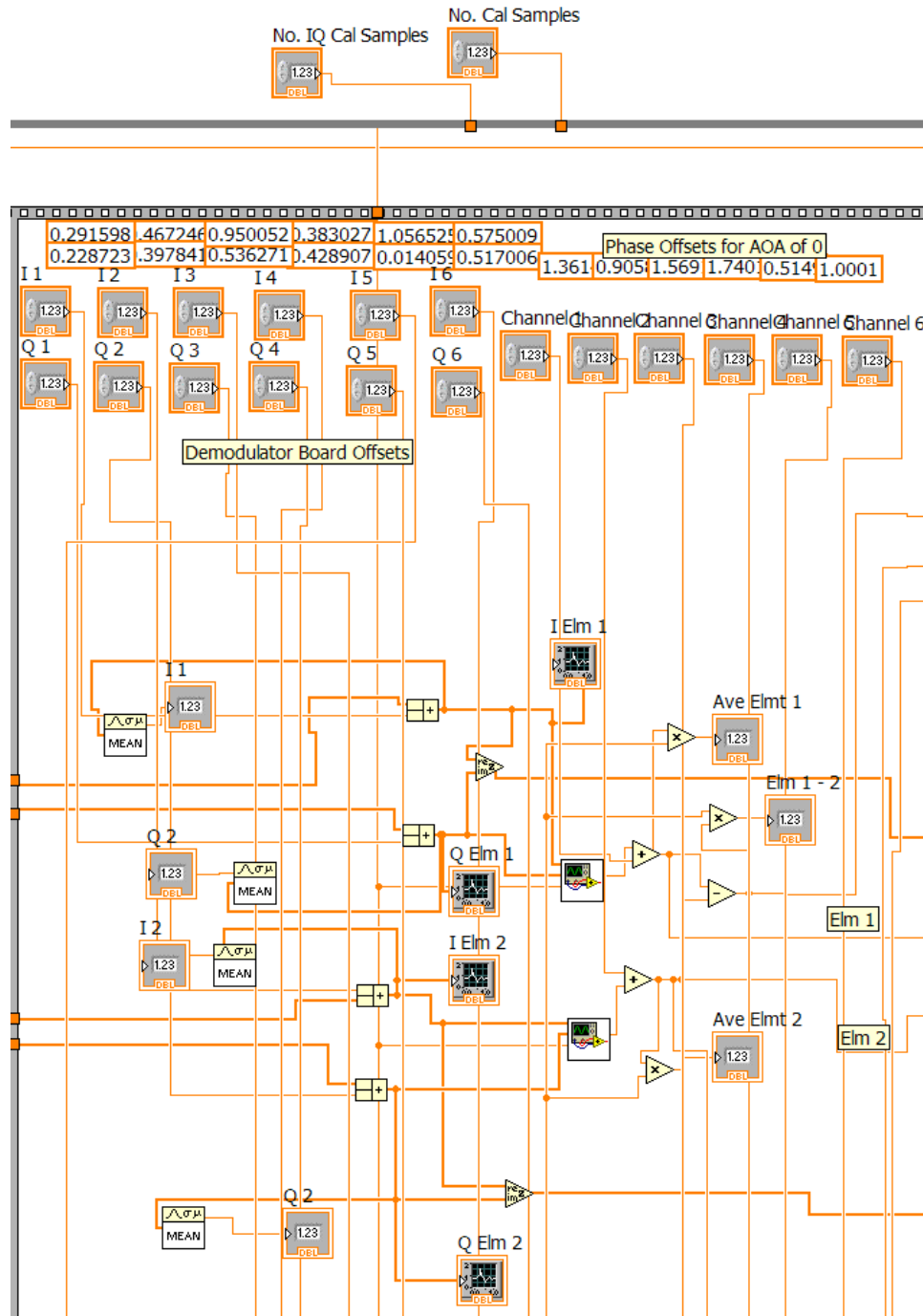
Figure 37.   Application of dc offsets for channel 0 and channel 1
of the six array channels.

The next step of the algorithm is the calculation of the scan angle. The tracking module allows the users to choose between two tracking methods: (1) RSNS and (2) monopulse DBF. When RSNS is selected, the phase difference between adjacent elements (1–2, 3–4, 5–6) is computed. The three values obtained from this process are averaged, and the result is used to calculate the AOA. The reason for the averaging process is that even though the RSNS requires only two elements to compute the AOA, by averaging over the three pairs, the phase errors will average out.

When monopulse DBF is selected for tracking, the initial scan angle is calculated with RSNS and then monopulse DBF takes over for the rest of the computation. The array factors are computed based on Equation (2.16), which was given in Chapter II. After the array factors are obtained, the sum and difference outputs are computed. Using these values and the monopulse slope constant given in Equation (2.2), we compute the correction angle for the direction of scan. The implementation of this process in software is shown in Figure 38. The current scan angle is updated by using the correction angle and the result obtained is used for the computation of the array factor in the next iteration. The module continuously computes the pointing error in order to make the correction angle approach to zero.

Figure 38.   Computation of correction angle from array factor
and sum/difference beams.

Finally, the front panel of the tracking algorithm is shown in Figure 39. It is required that the necessary settings (e.g., delays) for the PXI-5112 A/D converters, board offset values, phase adjustments and tracking method selection be made before running the program.
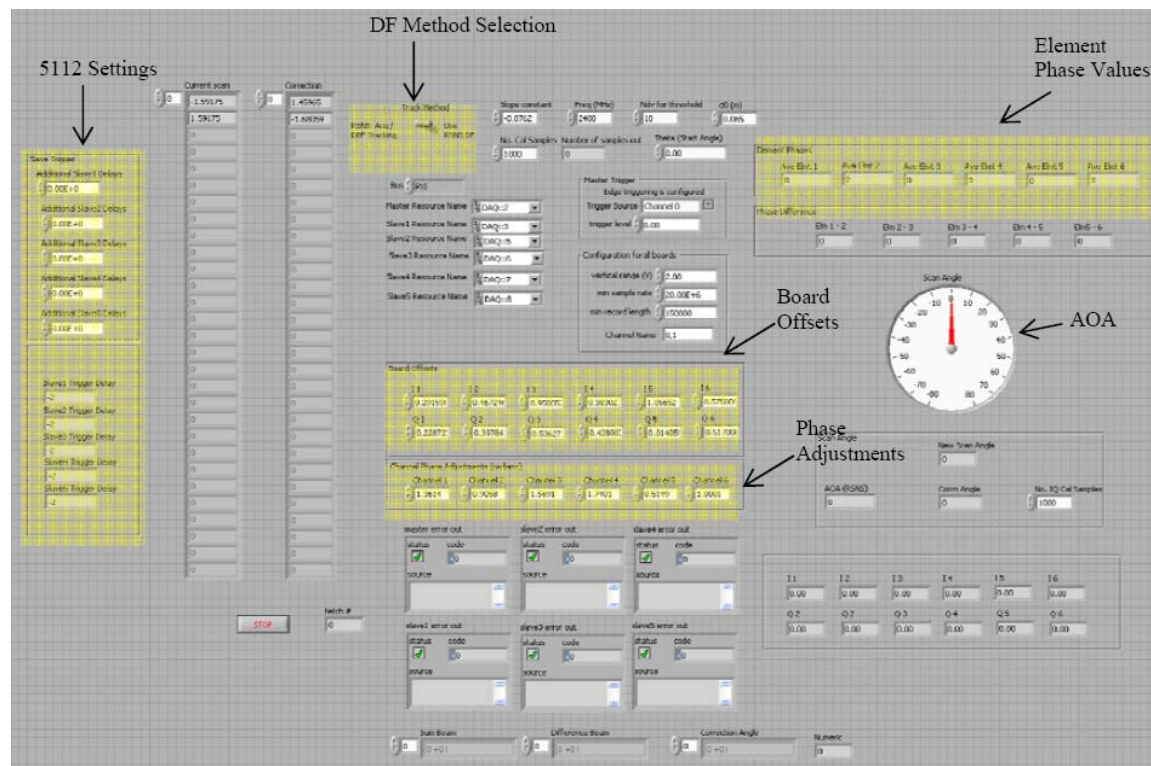
Figure 39.　　Front panel of the tracking algorithm (From [13]).

3.　NTSC Decoding Module

Of interest in this research, is the reception of video signals that are in NTSC format. After the FM modulated signals are received and demodulated, they need to be decoded in order to be displayed on a video screen. For this purpose, a VI for NTSC video signal decoding for a single channel was developed by Professor David C. Jenn (Naval Postgraduate School) and modified for use in the UAV digital tracking array hardware. The VI was named as "*NTSC Video Decode*" and consists of three subVIs,

which are, namely: (1) *Open and Fetch from 5112*, (2) *Fetch from 5112* and (3) *NTSC Processor*. The functions of these subVIs are illustrated in the process flow diagram shown in Figure 40.
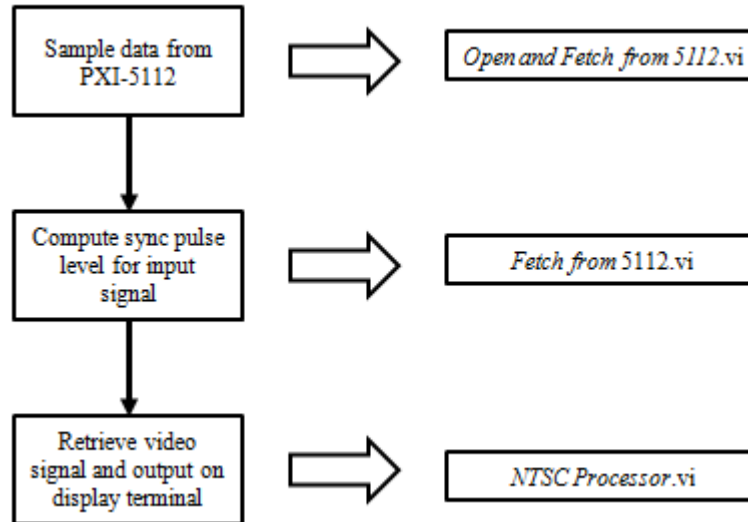
Figure 40.   Process flow diagram for the NTSC decoding module (After [13]).

The VI block diagram for *NTSC Video Decode* VI is given in Figure 41. The program takes several inputs for the configuration of the settings for sampling of the 5112 boards and the decoding process. These include minimum sample rate, minimum record length, vertical range, brightness level, horizontal sync adjust and trigger coupling. Once the program is run, the data is obtained by the *Open and Fetch from 5112* subVI, which is called within *Fetch from 5112* subVI. After sampling, the vertical sync level (Vsync) is computed in *Fetch from 5112* subVI and sent to the *NTSC Processor* subVI along with the sampled video data. The data obtained by this subVI is processed and the video image is recovered and displayed on the front panel screen.
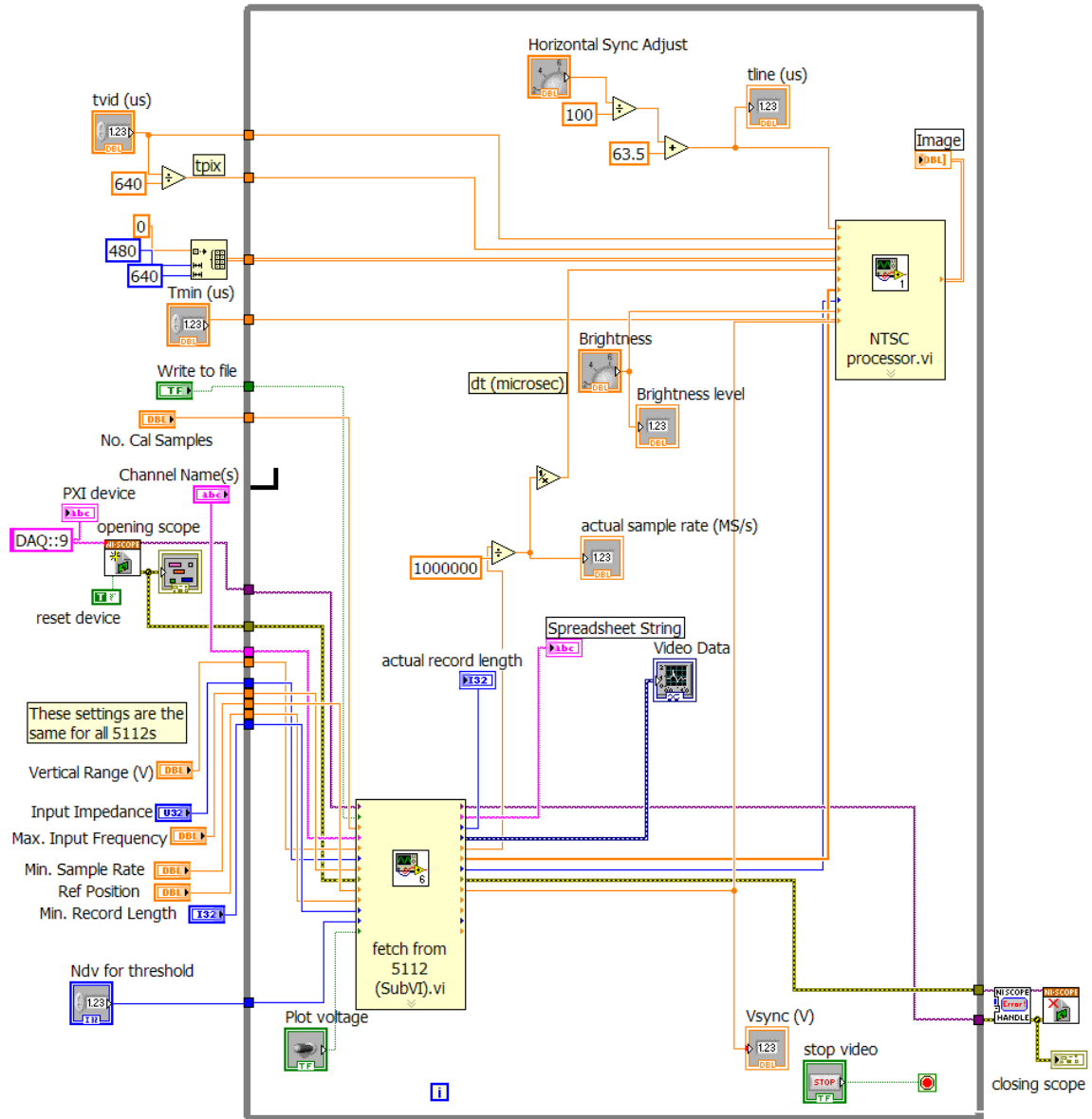
Figure 41.　　　NTSC decoding module VI block diagram.

In the following sections, the subVIs used in *NTSC Video Decode* VI are described.

a. Open and Fetch from 5112 SubVI

The VI block diagram of *Open and Fetch from 5112* subVI is shown in Figure 42. The main function of this subVI is to obtain the I and Q signals from the corresponding channels of the A/D converter according to the configuration settings. The trigger coupling is set to "dc" and the trigger source is set to "immediate" to acquire data continuously. The minimum sampling rate used is 20 MS/s and the vertical range used is 2 volts.
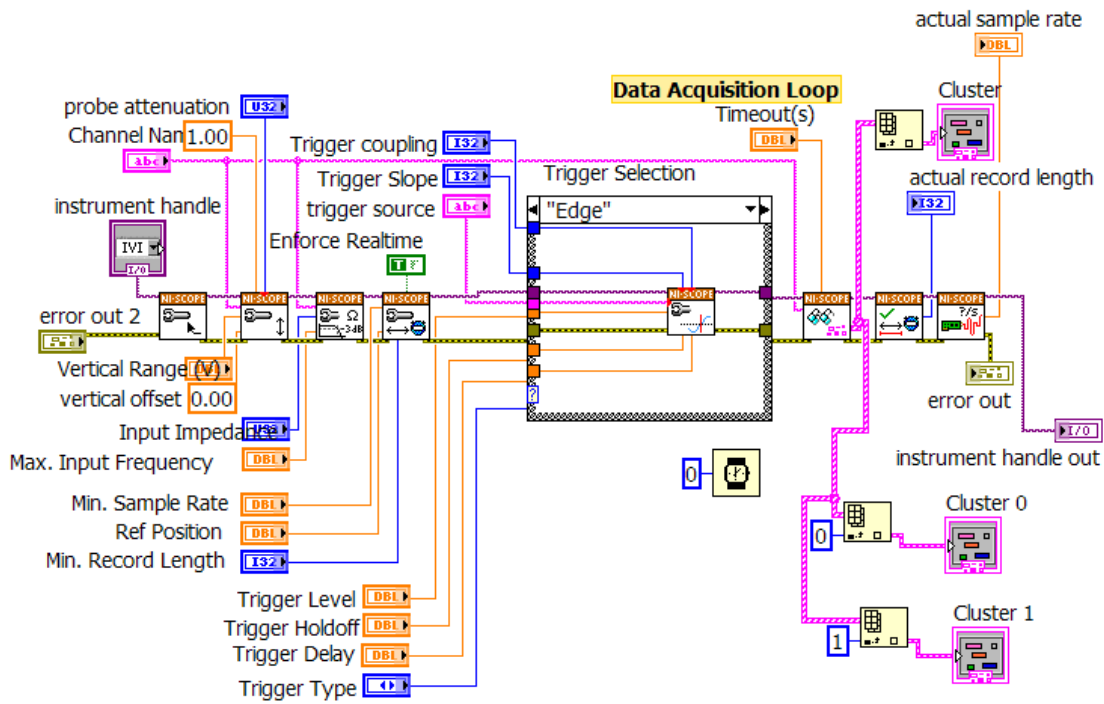
Figure 42.   Open and Fetch from 5112 subVI block diagram.

Since *Open and Fetch from 5112* is used as a subVI, the front panel is not used as a user interface and will not be shown in this section.

b. Fetch From 5112 SubVI

Fetch from 5112 subVI uses *Open and Fetch from 5112* subVI to acquire data from the PXI-5112 A/D converter. This process is shown in Figure 43. Also it is seen that some of the inputs that are entered to *NTSC Video Decode* VI are used in *Fetch from 5112* subVI.
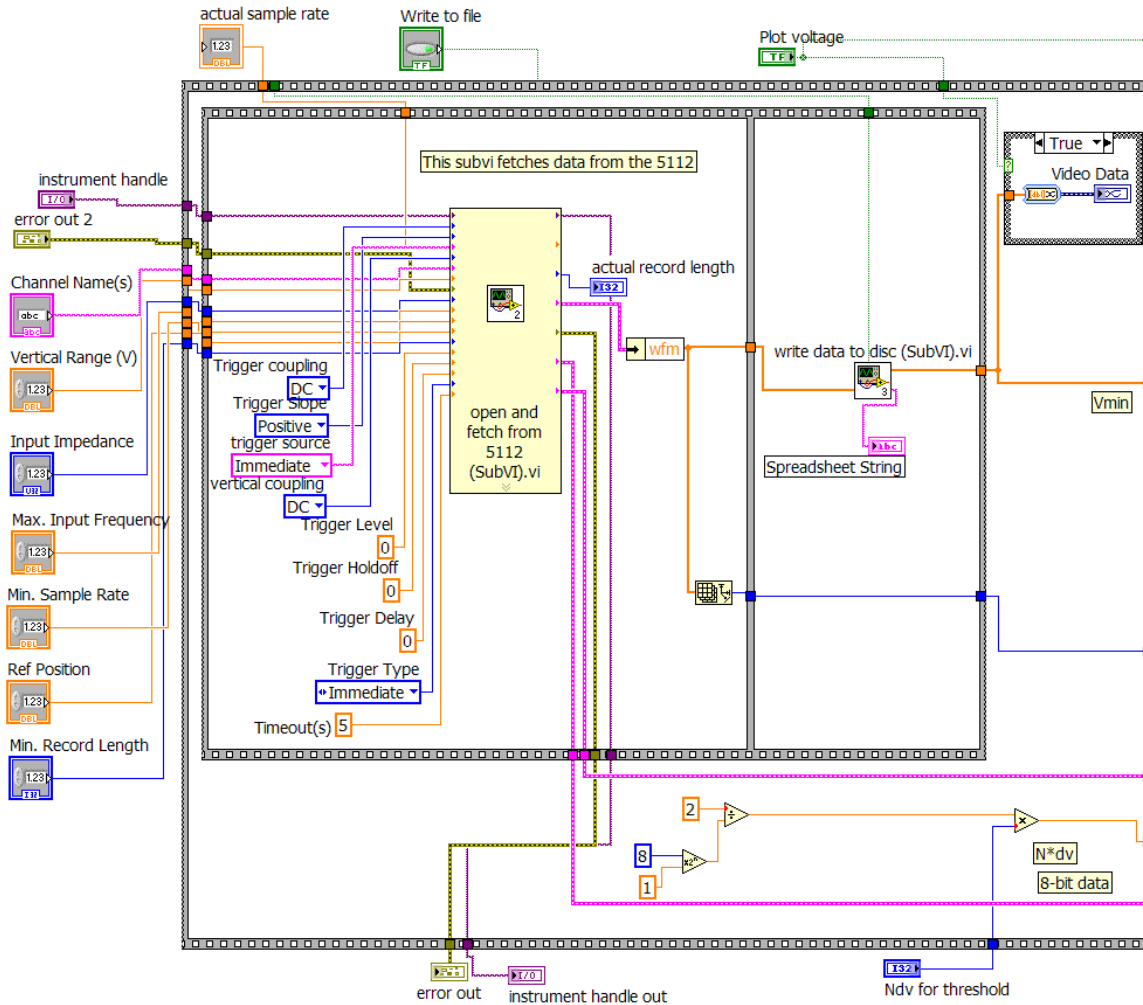
Figure 43.   *Fetch from 5112* subVI block diagram data acquisition section.

Since *Fetch from 5112* is used as a subVI, the front panel is not used as a user interface and will not be shown in this section.

76

Once the data is acquired, a calibration process is utilized for the calculation of the vertical sync threshold value, Vsync. This threshold value is used for the determination of a new synchronization pulse by the *NTSC Processor* VI. The details for this process are discussed in the next section.
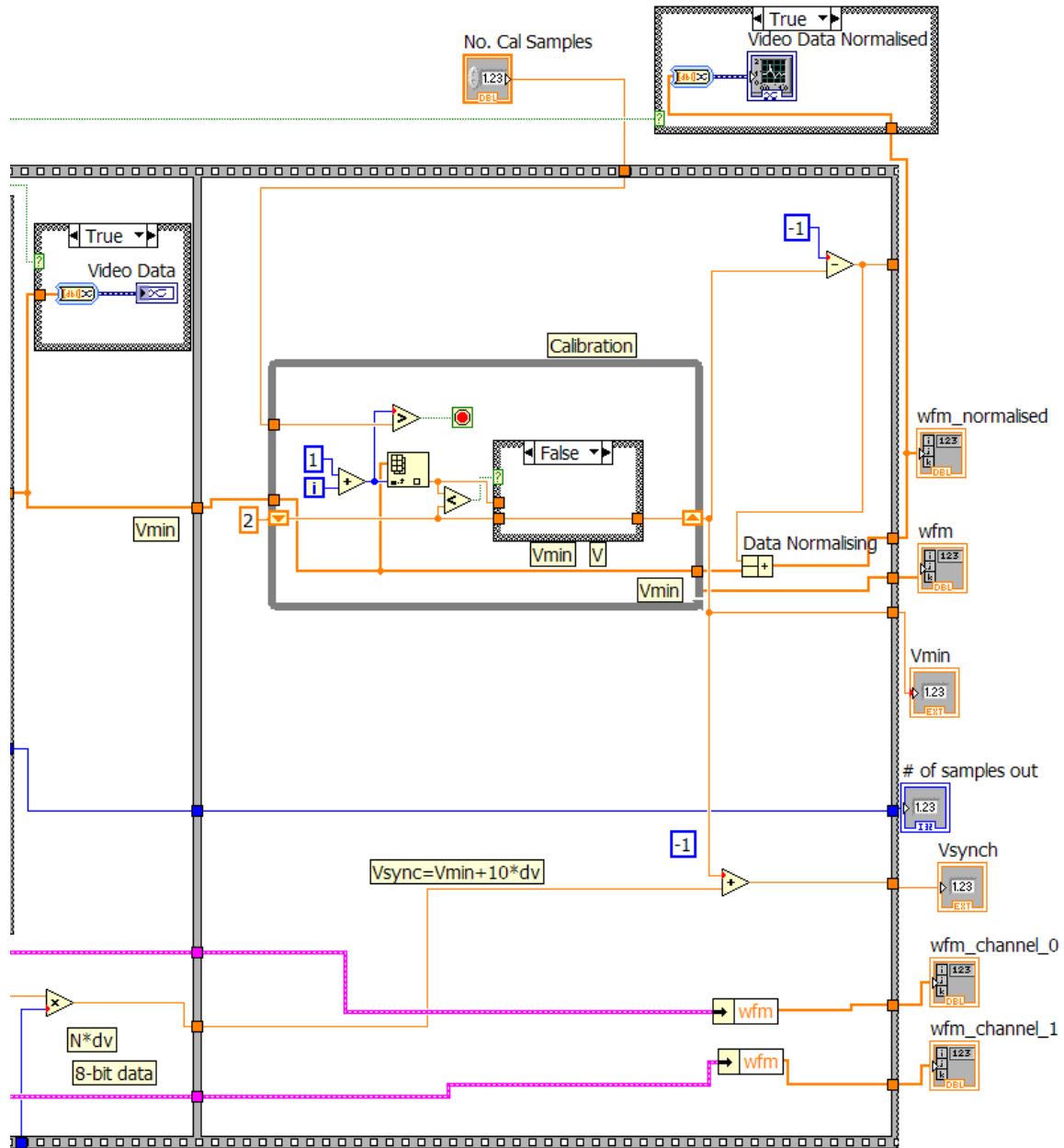
Figure 44.   *Fetch from 5112* subVI block diagram, calculation of vertical sync.

c. *NTSC Processor SubVI*

NTSC Processor subVI is the most important and complex subVI within the *NTSC Video Decode* VI. The NTSC-encoded video signal is retrieved and video data is displayed by this subVI. It was mentioned that the video signals are acquired and the threshold Vsync is calculated by the *Fetch from 5112* subVI. *NTSC Processor* subVI takes the video data along with the Vsync value and tries to find a valid sync pulse. The location of this process in the video signal is illustrated in the timing diagram given in Figure 45. The validation starts by comparing the amplitudes of each data point with Vsync. After a data point with amplitude less than Vsync is found, another comparison process starts to find a data point that has larger amplitude than Vsync. If this data point is found as well, the time between the two data points is calculated and compared with the time considered to be the minimum duration for a valid sync pulse. This duration is represented by *Tmin*. If the calculated time is greater than *Tmin*, the pulse is validated as a sync pulse. If it is less than *Tmin*, the pulse is considered as noise.
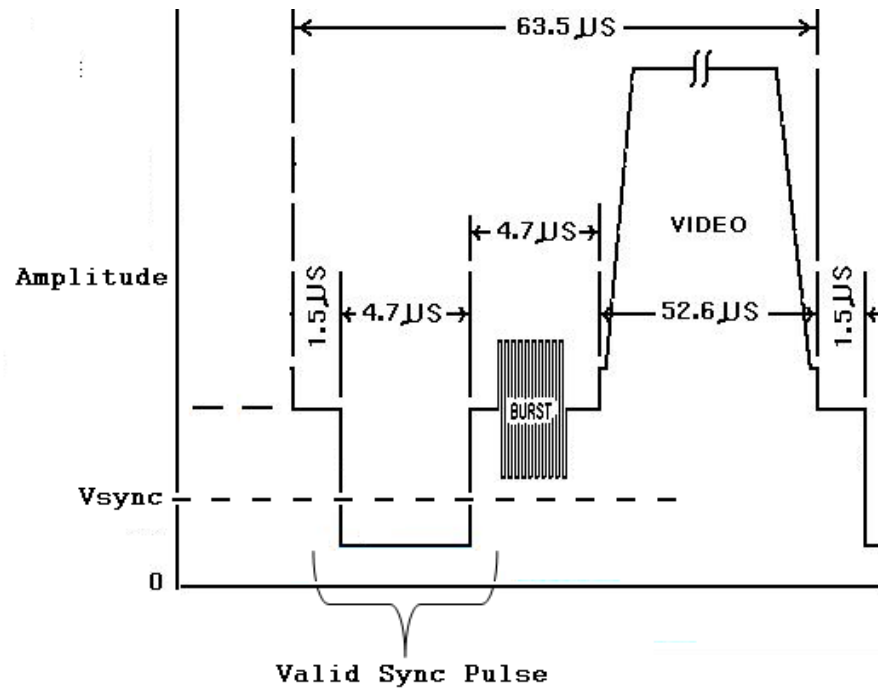
Figure 45.   NTSC video signal timing diagram (After [13]).

78

In Figure 46, the software implementation of the sync pulse validation process within the *NTSC Processor* subVI is shown.
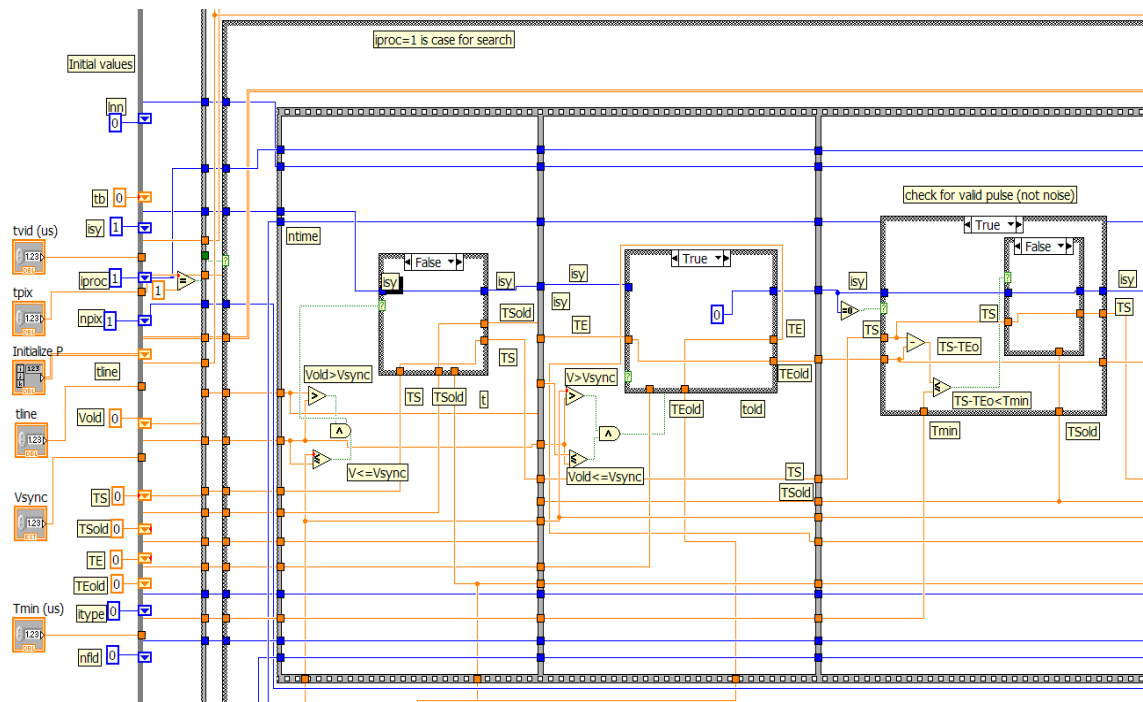
Figure 46.　　*NTSC Processor* subVI block diagram section for sync pulse detection.

The calculated duration of the sync pulse is also used for determining whether the field found is odd or even. This process is done in the section of the *NTSC Processor* subVI block diagram shown in Figure 47. Also implemented in this section is the configuration of several parameters for the video decoding process that is done next.

Figure 47.   Field type determination and parameter configuration in *NTSC Processor* subVI.

In the next step, the data portion of the video signal is read. The odd and even fields are read and the video image is constructed. There are 259 lines read until the end of each field and 640 pixels until the end of each line. The odd field is read first and the even field is read afterwards. When both fields are read successfully, the video image is constructed and displayed in the video screen located on the front panel of the *NTSC Video Decode* VI. The software implementation of the video data read process is shown in Figure 48.

80

Figure 48.   Video data stream reading process in *NTSC Processor* subVI.

Since *NTSC Processor* is used as a subVI, the front panel is not used as a user interface and is not shown in this section.

4.   FM Demodulation Module

There are two versions of this module used in the digital tracking array hardware, which are, namely, *FM Demod Single Fetch* VI and *FM Demod Single Fetch Tangent* VI. The *FM Demod Single Fetch* VI was designed and built by Tan and Pandya [13] in 2009. It is based on the *FM Demodulation* function included in the Signal Processing toolkit in LabView. The *Fetch from 5112* subVI, introduced previously, is used within this module in order to obtain data from the PXI-5112 channels. The settings that are required for this subVI are the same as what was given previously in Section 3 of this chapter and adjusted from the front panel of the *FM Demod Single Fetch* VI. The front panel of this VI was modified from its original version to provide a better user interface. The modified front panel is shown in Figure 49.

81
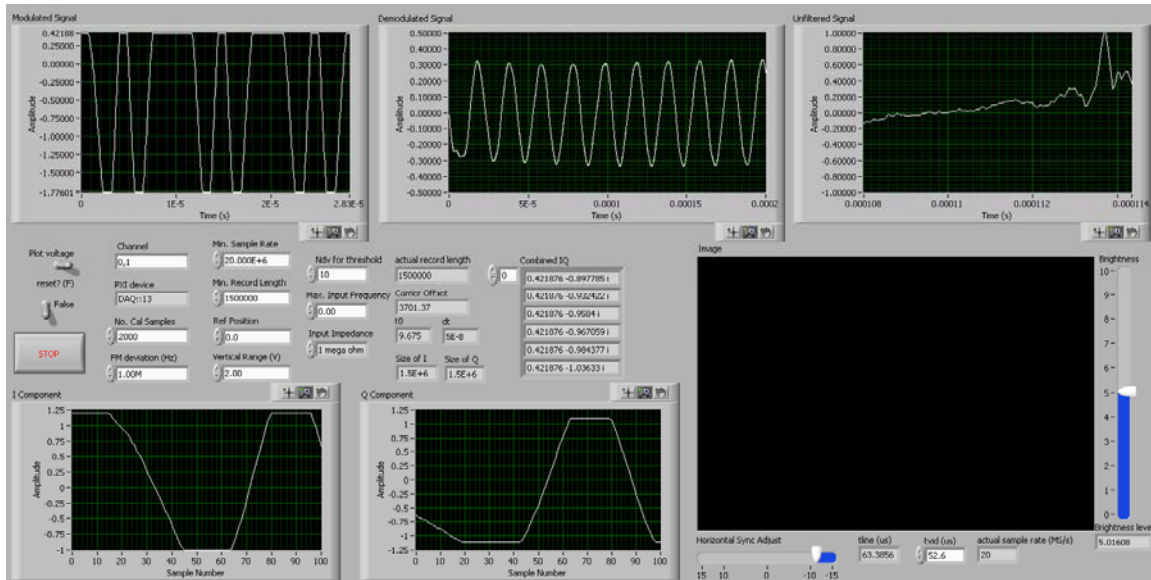
Figure 49.   *FM Demod Single Fetch* VI front panel.

There are five waveform charts in the front panel used for displaying the following components: (1) modulated signal ($I + jQ$, upper left), (2) demodulated signal before filtering (upper middle), (3) demodulated signal after filtering (upper right), (4) in-phase component of the incoming signal (lower left), (5) quadrature component of the incoming signal (lower middle). The display located on the lower right of the front panel is used for displaying the demodulated video data after being decoded.

The block diagram of *FM Demod Single Fetch* VI is shown in Figure 50. It is noticed that the NTSC decoding module is embedded within the demodulation module for displaying the video image after demodulation. When the program is run, the data is fetched from the 5112 channel by the *Fetch from 5112* subVI. This subVI provides I and Q components of the signal at its output. These components are bundled together along with the timing and sampling information and sent to the *MT Demodulate FM* function. The location of this function is marked with a circle in Figure 50. The demodulated data is then sent to the *NTSC Processor* subVI for decoding and displaying the video data.

82
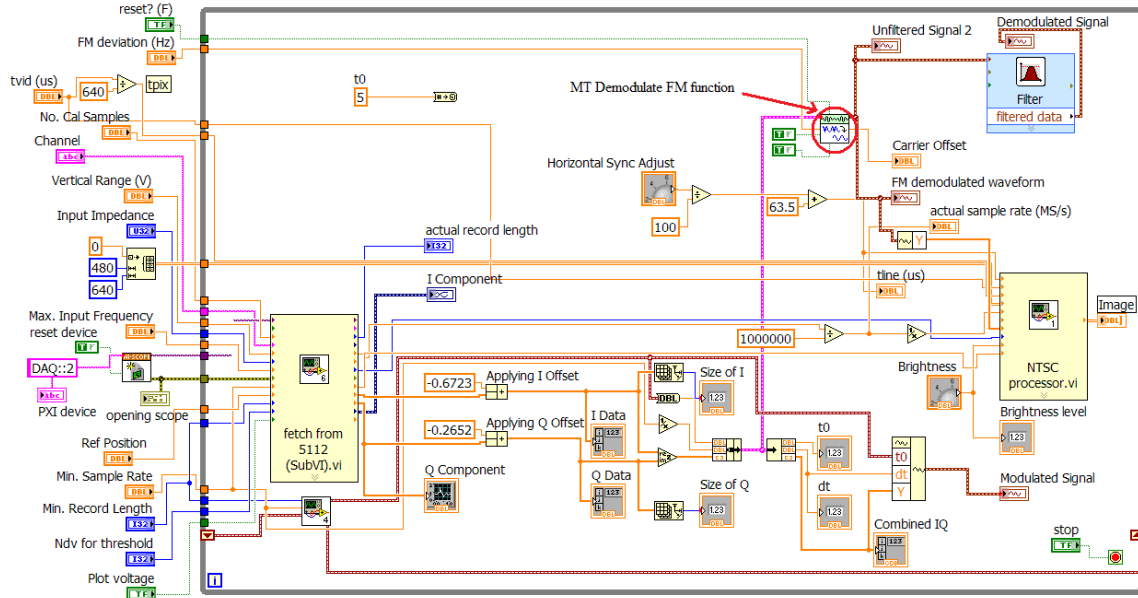
Figure 50. *FM Demod Single Fetch* VI block diagram.

The second version of the FM demodulation module is the *FM Demod Single Fetch Tangent* VI, which is built by the modification of *FM Demod Single Fetch* VI. The difference in this VI is that the *MT Demodulate FM* function in the previous version was replaced with a subVI called *Tangent Demod*. This subVI was designed to implement tangent-type demodulation of the baseband I and Q signals. The implementation is based on the theory that was given in Chapter IV Section B. The front panel of this VI is the same as the one that was shown in Figure 49. The block diagram of this subVI is shown in Figure 52. The inputs of the subVI are the I and Q components delivered by the *Fetch from 5112* subVI. The output of the subVI is connected to the Butterworth filter, where the signal is filtered and displayed.
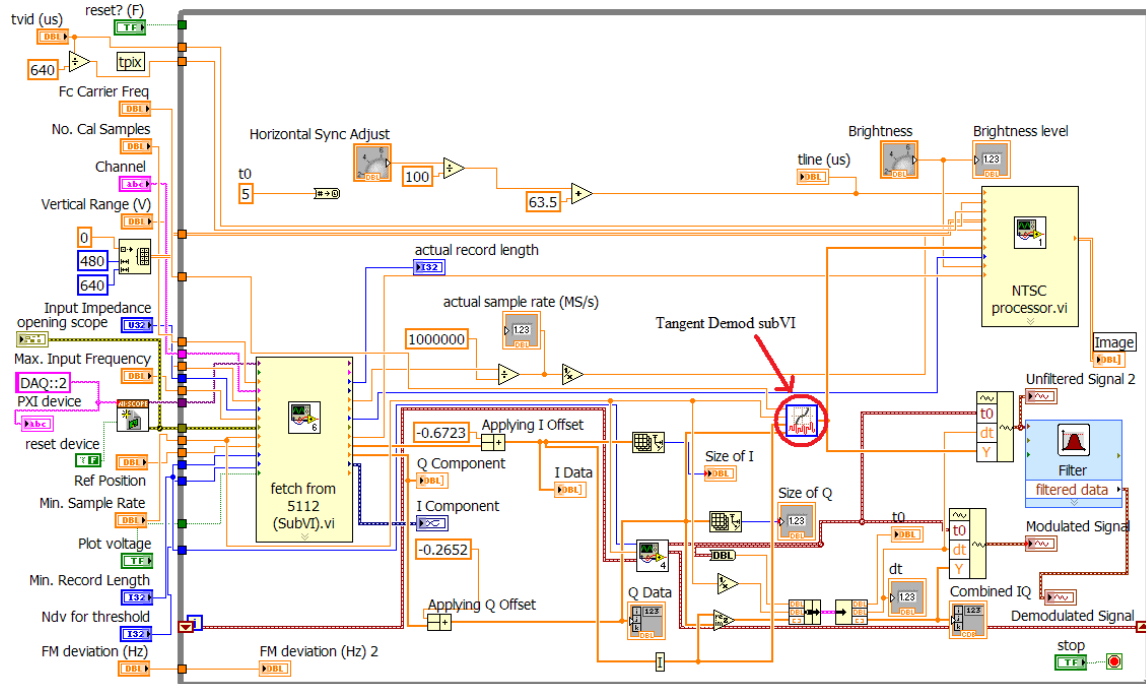
Figure 51.   *FM Demod Single Fetch Tangent* VI block diagram.
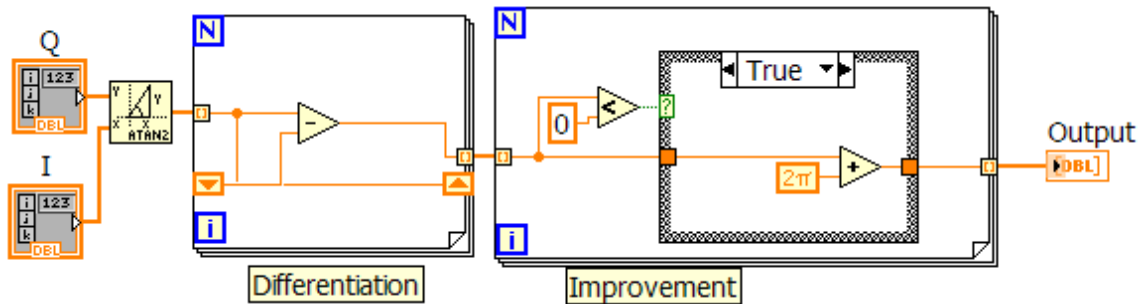
Figure 52.   *Tangent Demod* subVI block diagram.

D.   SYSTEM POWER SPECIFICATIONS

In [13], the performance analysis of the antenna system is given. The minimum power that can be received by each channel is given as

$$P_{\min_{ch}}(\text{dB}) = P_{\min_{demod}}(\text{dB}) - G_{LNA}(\text{dB}) = -90 \text{ dBm} = -120 \text{ dB} \tag{5.5}$$

where $P_{\min_{demod}} = -65$ dBm is the start of linear region of TPC30 on the AD8347 datasheet [31] and $G_{LNA} = 25$ dB is the gain of the LNA located after the antenna. Using the $P_{\min_{ch}}$ value obtained, we find the maximum range of the array system as

$$R = \sqrt{\frac{P_t G_t G_r \lambda^2}{(4\pi)^2 P_{\min_{ch}}}} = 34.4 \text{ km} \tag{5.6}$$

where $P_t = 0.1$ W and $G_t = 3$ dB are the UAV transmitted power and antenna gain, respectively, and $G_r = 10$ dB is the array element gain. Using the same equation, we calculate the maximum range without the LNA (i.e. $P_{\min_{ch}} = -95$ dB) as 1705.8 m. Comparing the maximum ranges with and without the LNA, we see that the LNA is an essential part of the receiver in order to achieve practical maximum ranges. It also eliminates the need to transmit higher power at the UAV to achieve longer ranges and controls the receiver noise.

The minimum SNR is calculated by

$$SNR_{ch} = \frac{P_{\min_{ch}}}{N_{sys}} N = 12.2 \text{ dB} \tag{5.7}$$

where $N_{sys} = kT_{sys}B = -124.4$ dB is the system noise calculated in [13] and $N = 6 = 7.8$ dB is the number of array elements.

E.   SUMMARY

In this chapter, the hardware and software components of the UAV digital tracking array system were introduced. The performance parameters for some of the hardware (e.g., antenna) were also given. LabView programming environment was introduced and details of the software modules were presented.

In the next chapter, the results of the simulations done for the validation of the demodulation techniques and bench-top tests conducted for the verification of the software modules are presented.

VI. DESIGN VALIDATION AND VERIFICATION

In this chapter, the validation and verification process of the software components developed for the digital tracking array receiver processor are discussed. In [32], the definitions of validation and verification are given. Validation is associated with the question, "Are we building the right solution?" and verification is associated with the question "Are we building the solution right?" The validation and verification processes discussed in this chapter are based on these questions. In Section A, simulations, which were done to validate the software components, are explained. In Section B, the tests that were made for the verification of these software components on the hardware are discussed.

A. VALIDATION OF FM DEMODULATION TECHNIQUES

The FM demodulation techniques that are used to demodulate video signals transmitted from a UAV were discussed in Chapter IV Section B. These techniques included demodulation at baseband, tangent-type demodulation and demodulation using Kalman filters. It was mentioned that the Kalman filter approach is expected to be slow and have a higher complexity compared to the other approaches. Hence, it was not implemented for the proposed system.

A good method for simulation is to use simple inputs at the beginning and more complex inputs, which are similar to real inputs, later. For this purpose, there were two waveforms used for the simulation of each demodulation technique. One of these waveforms was selected to be a simple sine wave with 50-kHz frequency. The second waveform chosen was a video signal that was captured using a video camera with LabView. The video signal captured was saved as a text file that included the sampled video data. This text file was then fed to the simulation programs as the input (i.e., modulating signal). The simulations were done separately in MATLAB and LabView. The results of the simulations are discussed in the following sub-sections.

1. Baseband FM Demodulation Simulations

The baseband FM demodulation technique which was given theoretically in Equation (4.11), was simulated using MATLAB and LabView. The demodulation process was illustrated in Figure 23. The generic block diagram for the simulation of baseband demodulation is given in Figure 53. The following sections include discussions about the simulations based on this block diagram.

| Create Waveform | → | Apply FM Modulation | → | Construct I and Q | → | Apply Baseband FM Demodulation | → | Plot Input vs. Output |
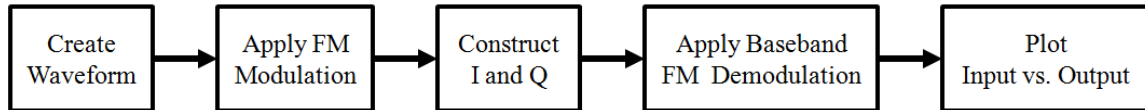
Figure 53.   Block diagram for baseband demodulation simulation.

a. MATLAB Simulations

As mentioned previously, a 50 kHz sine wave and a data file including real video data captured from a video camera were used as modulating signals for the simulations.

The MATLAB code used to simulate the demodulation of the sine wave is given in Appendix Section A. For the 50-kHz sine wave, the sampling frequency used is 1.5 MHz and the frequency deviation applied is 20 kHz. The result of the simulation is shown in Figure 54. It is seen that the frequency of the message signal was recovered successfully. However, the demodulated signal had to be amplified to match the original signal since the output of the demodulator produced very low voltages.
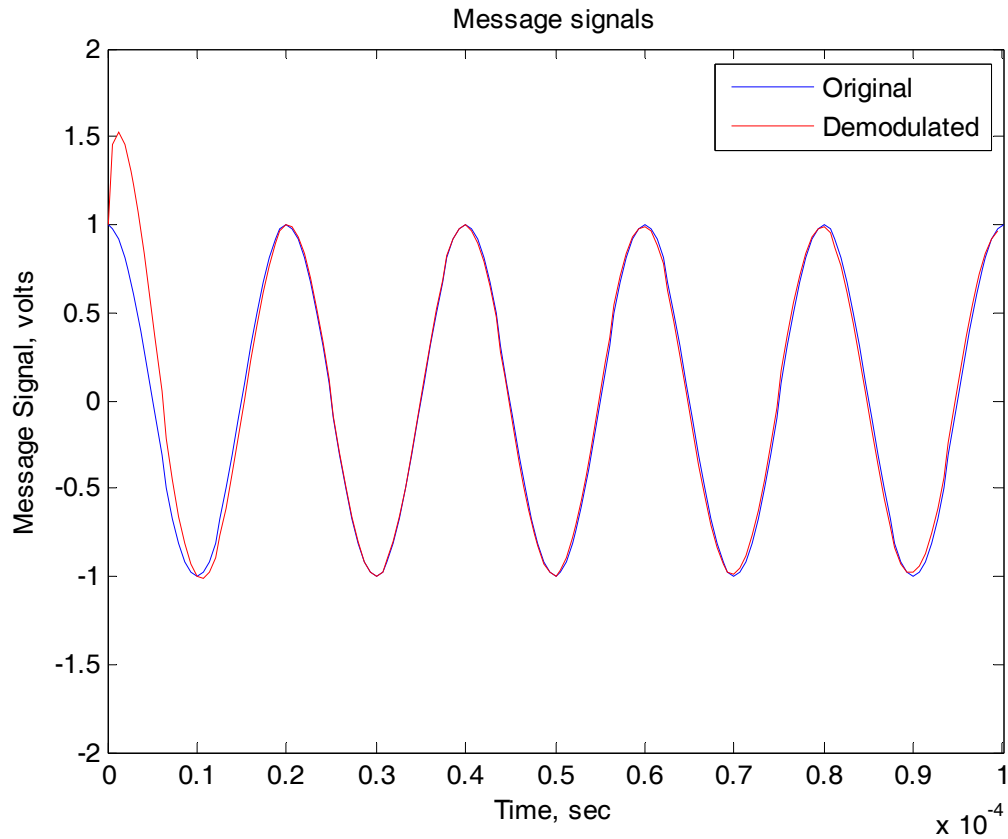
Figure 54.   Comparison of original and demodulated signals using baseband
demodulation in MATLAB.

In the second part of the simulation, real-time video data was used as the
modulating signal. A MATLAB program, which is given in Appendix Section B, was
used to display the video frames. The original video frame displayed using this program
is shown in Figure 55.

Figure 55.   Original video frame used as the modulating signal.

The MATLAB code for the simulation is given in Appendix Section C. In the simulation, the input signal (i.e., video) needs to be integrated and frequency modulated before sending it to the demodulator. The video signal that was used as the modulating signal in the simulation is plotted in Figure 56. The output obtained from the demodulation of the FM video signal is shown in Figure 57. Also, the demodulated video frame is shown in Figure 58. The results show that FM video signal was demodulated successfully using the baseband demodulation approach discussed in Chapter IV. However, the amplitude of the demodulated signal was very low, which reveals the need for amplification or rescaling in the processor.

90
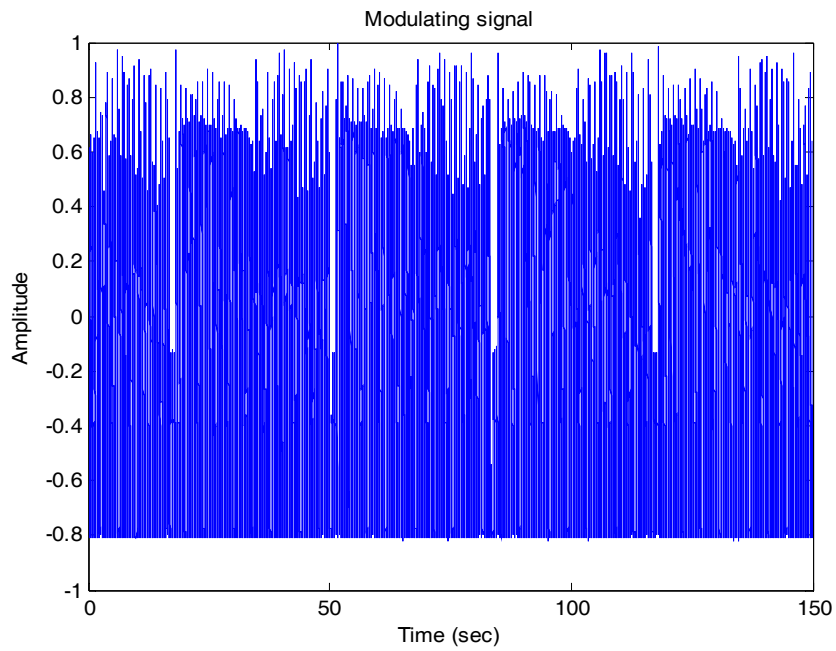
Figure 56.   Video signal used as the modulating signal.
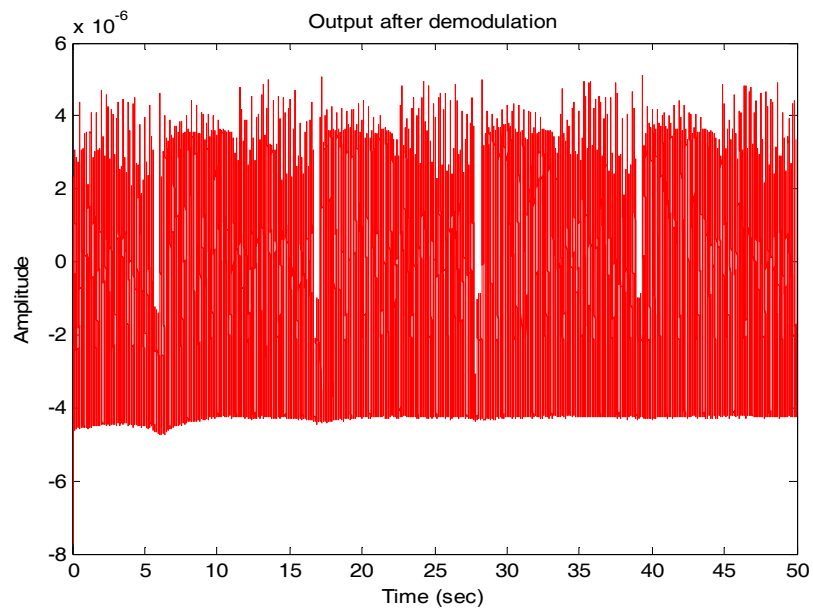
Figure 57.   Demodulated video signal.

Figure 58.   Demodulated video frame.

The phase and amplitude of the signal for every shifted RF phase degree is determined by plotting the baseband I and Q values. A good phase response from the RF signal fed to the demodulator is expected to give a circle with equally distributed RF input signal samples for every phase degree [10]. The phase response obtained from the video signal is shown in Figure 59. It is seen that the I and Q values are distributed on a symmetrical circle as expected.
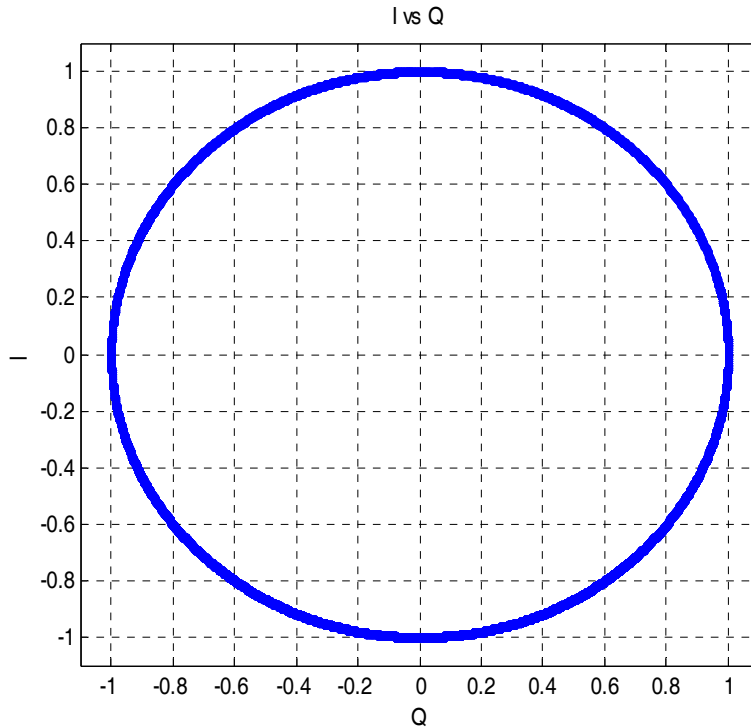
Figure 59.   *I* vs. *Q* plot for the video signal.

b.   *LabView Simulations*

The video signal demodulation simulation that was performed in the previous section was repeated in LabView in order to verify the results obtained from MATLAB. Moreover, LabView performs faster than MATLAB in most situations where arrays of data are processed using loops. With this feature of LabView, long calculation times encountered in MATLAB were avoided.

A LabView VI was developed for performing the baseband demodulation simulation. The algorithm of the program was developed based on the block diagram given in Figure 53. The construction of the video signal from a data file is illustrated in the partial VI block diagram shown in Figure 60. The other portion of the VI block diagram, which performs modulation, mixing, demodulation and amplification is shown in Figure 61.

93
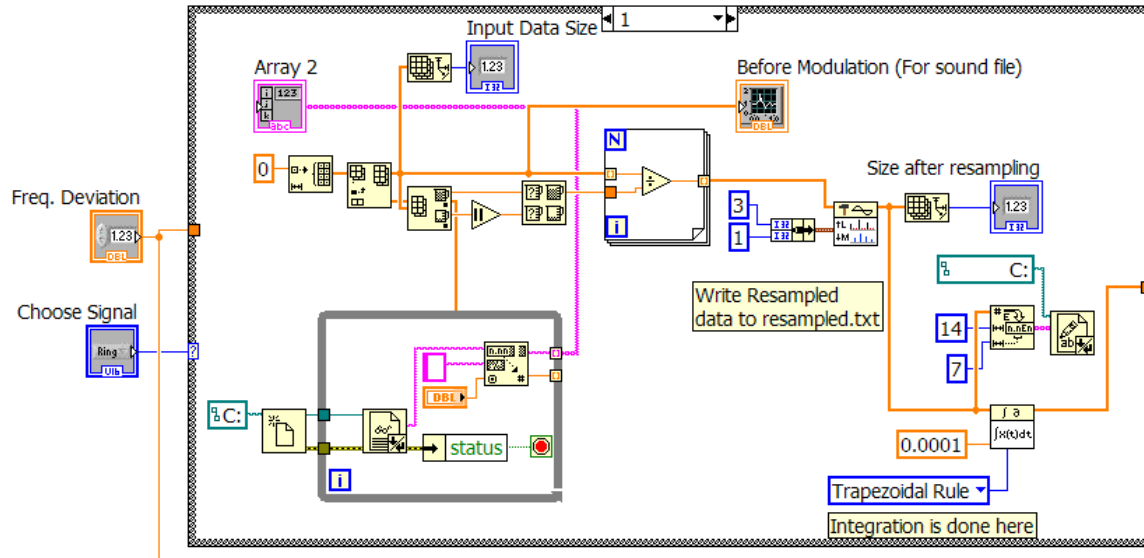
Figure 60. Video signal construction from data file in LabView.
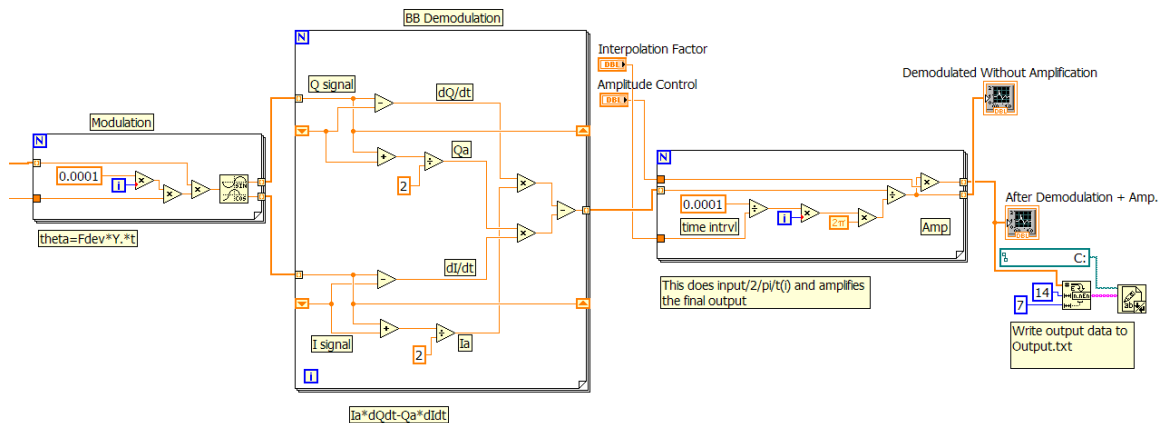
Figure 61. Modulation, mixing, demodulation and amplification process.

In the simulation, the video data file that was used previously is used to create the modulating signal. The modulating signal obtained from the file is shown in Figure 62. The resulting video signal after the demodulation process is given in Figure 63. Comparing the two figures, we see that the video signal was recovered successfully using the baseband demodulation method.

94
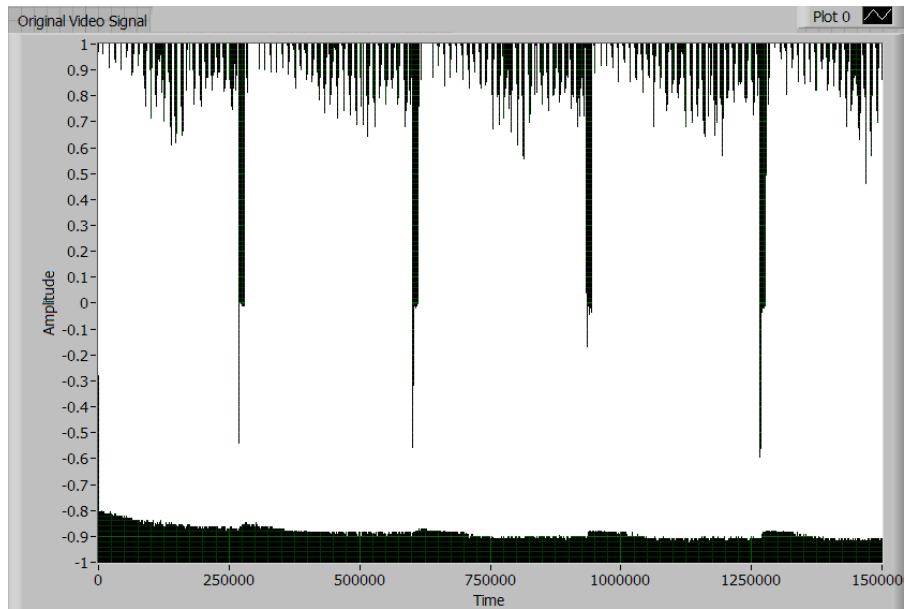
Figure 62.   Video signal used as the modulating signal.
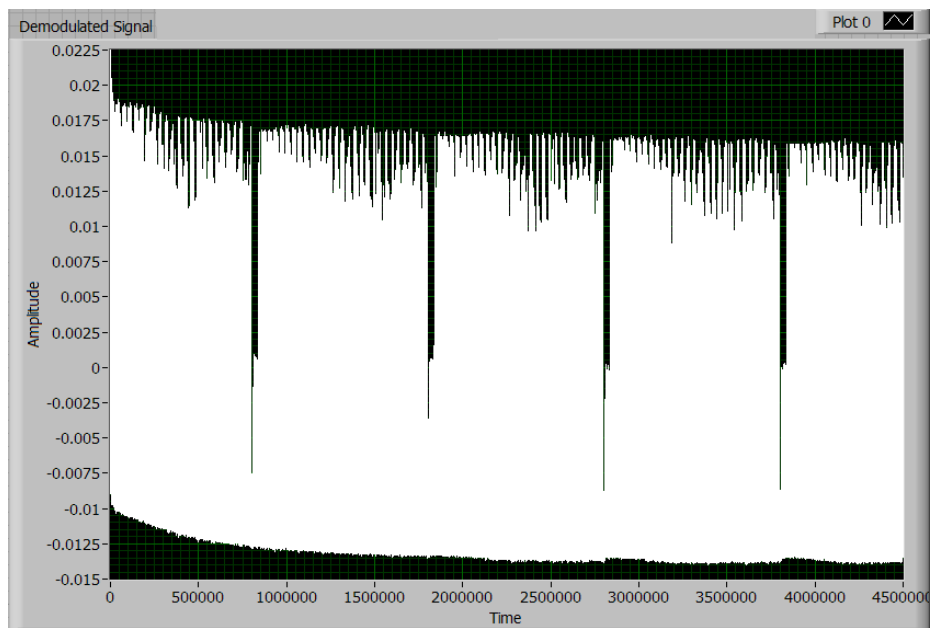
Figure 63.   Demodulated video signal.

The only problem that was encountered with this simulation program was that the frequency deviation had to be selected as a very low value [i.e., 100 Hz] since high attenuation of the signals over time was encountered with high-frequency deviation. An example of this attenuation is shown in Figure 64.
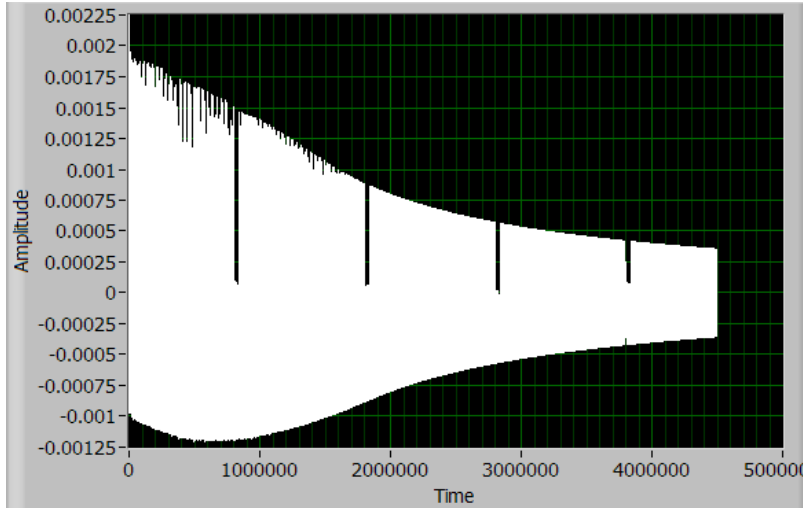
Figure 64.   Attenuation of demodulated signal in the simulation due to high-frequency deviation.

2.   Tangent-type FM Demodulation Simulations

The tangent-type FM demodulation of baseband I and Q signals was discussed in Chapter IV. The demodulation process, which was illustrated in Figure 24, is simulated using MATLAB and LabView. The generic block diagram for the simulation program of tangent-type baseband demodulation is given in Figure 65. Two simulations for two different cases were performed, as was done for the baseband demodulation. Also, the simulations were first done with MATLAB and then verified with LabView. The following sections include discussions about the simulations based on the block diagram given in Figure 65.

96
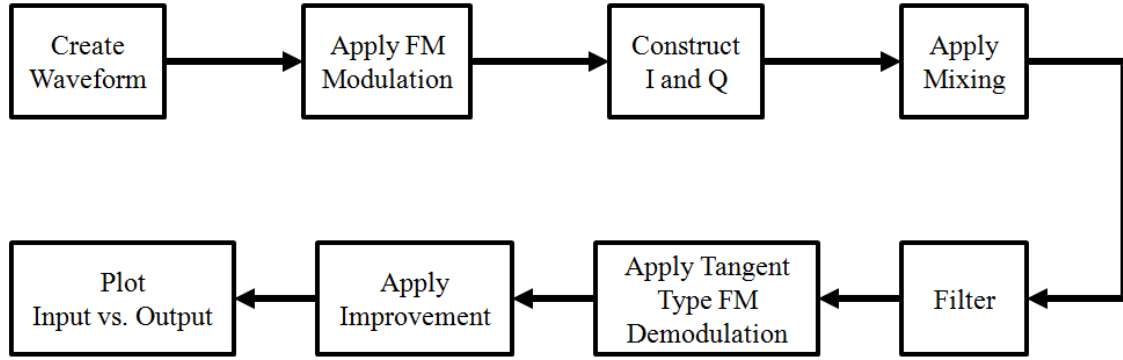
Figure 65.   Block diagram for tangent-type FM demodulation simulation.

a.   *MATLAB Simulations*

The procedure given in Figure 65 was implemented in MATLAB to simulate the two scenarios for demodulation. Similar to the method used for baseband demodulation, a 50-kHz sine wave and a video signal were used as modulating signals.

The MATLAB code for the first scenario is given in Appendix Section E. In this scenario, a 50-kHz sine wave was formed as the modulating signal. The carrier frequency and the frequency deviation used were 1.5 MHz and 10 kHz, respectively. The sampling frequency was set to be at least five times the sum of the message and carrier frequencies (i.e., $f_s = 5 \cdot (f_m + f_c)$). The 50-kHz sine wave was formed and impressed on the carrier. It was then split into two channels (I and Q), which were then down-converted by mixing and filtering. The baseband I and Q signals obtained after this process were then input to the demodulator. The high-frequency components created by the mixing process were suppressed by using a third-order Butterworth low-pass filter with a cut-off frequency equal to 2/5 of the message frequency (i.e., $f_{cut-off} = 0.4 \cdot f_m$).

97

The result of the demodulation process is given in Figure 66. It is seen that the frequency of the modulating signal was successfully recovered. However, the amplitude of the demodulated signal had to be amplified 32 dB to match the original signal since the output of the tangent-type demodulator provided very low amplitudes. Also seen is a small phase shift between the original signal and the demodulated signal. This phase shift is created by the filter used. Additional tests performed with different parameters showed that, as the cut-off frequency of the filter is increased, the phase shift becomes larger.
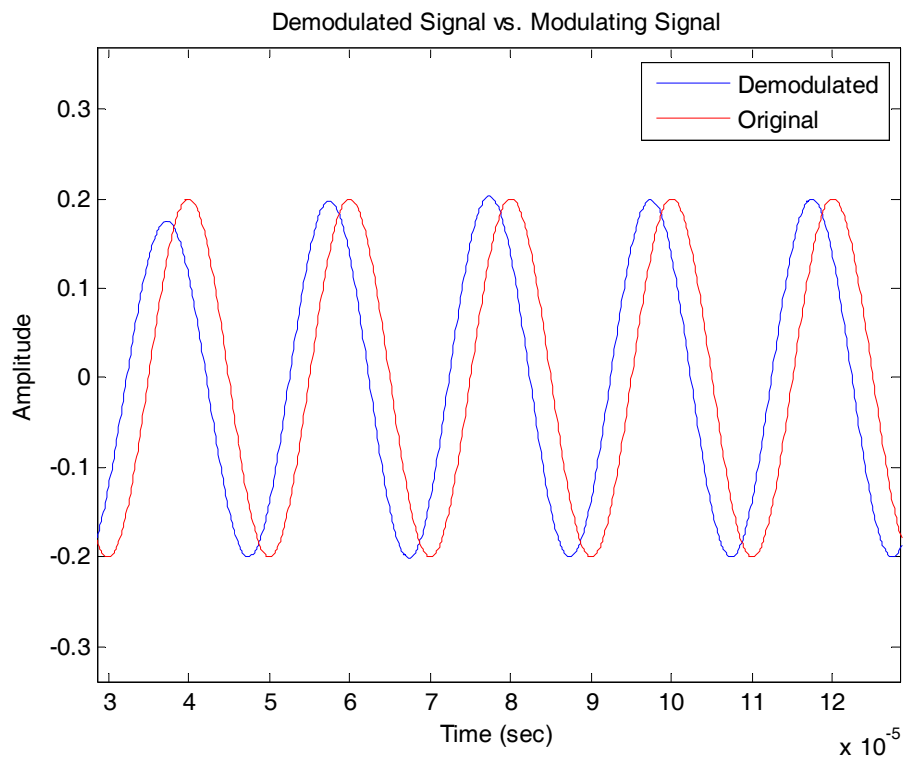
Figure 66.   Demodulated vs. original message signal
            for tangent-type demodulation.

In the second scenario, the video signal used previously was applied to the demodulation procedure described in Figure 65. The MATLAB code for this process is given in Appendix Section F. The video data read from a text file was impressed on a carrier with a frequency of 20 kHz. The sampling rate and the frequency deviation used were 100 kHz and 1 kHz, respectively. The modulation was done with MATLAB's *fmmod* function. The modulated signal was separated into two channels to form *I* and *Q* signals. These channels were then down-converted to baseband by mixing and filtering. The filter used was a third-order Butterworth low-pass filter with a cut-off frequency equal to the carrier frequency (i.e., $f_{cut-off} = f_c$). After this process, the baseband *I* and *Q* signals were fed to the input of the arctangent block. The output of the arctangent block was fed into a differentiator and the demodulated signal was obtained at the output. The demodulated signal was then put through the improvement process. Finally, the resulting signal was plotted. It was noticed that the demodulated video signal obtained from the improvement section had a dc offset of 0.8375 volts. Also, the amplitude of the demodulated video signal was lower than the original video signal. Hence, to compensate for these conditions, a dc offset of -0.8375 was applied to the demodulated video signal first and 12-dB amplification was applied to the resulting signal.

The comparison of the modulated (i.e., original) video signal and the demodulated video signal is made in Figure 67 and Figure 68. It is seen that the original video signal was successfully recovered. In addition to these figures, the demodulated video frame, which was obtained from the MATLAB program given in Appendix Section B, is shown in Figure 69.
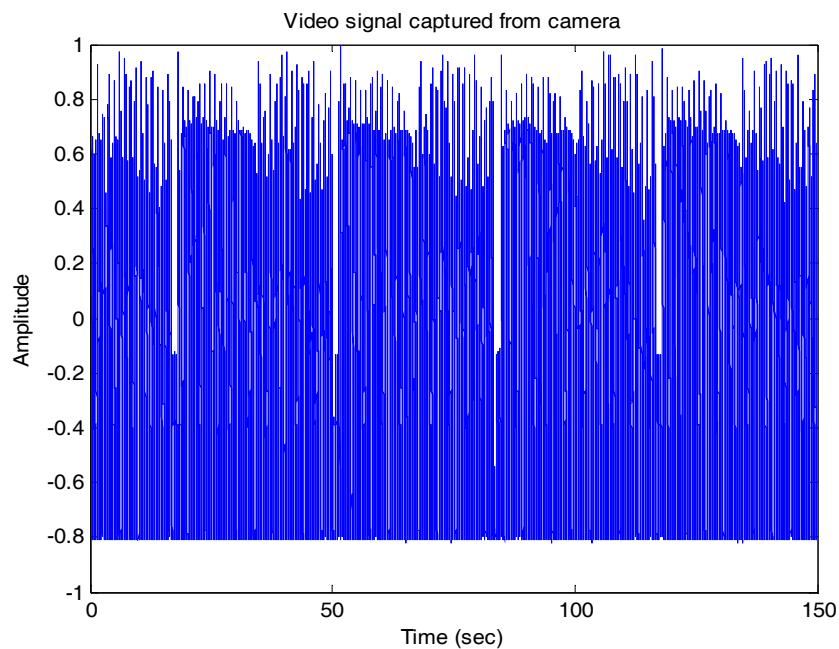
Figure 67.   Original video signal.
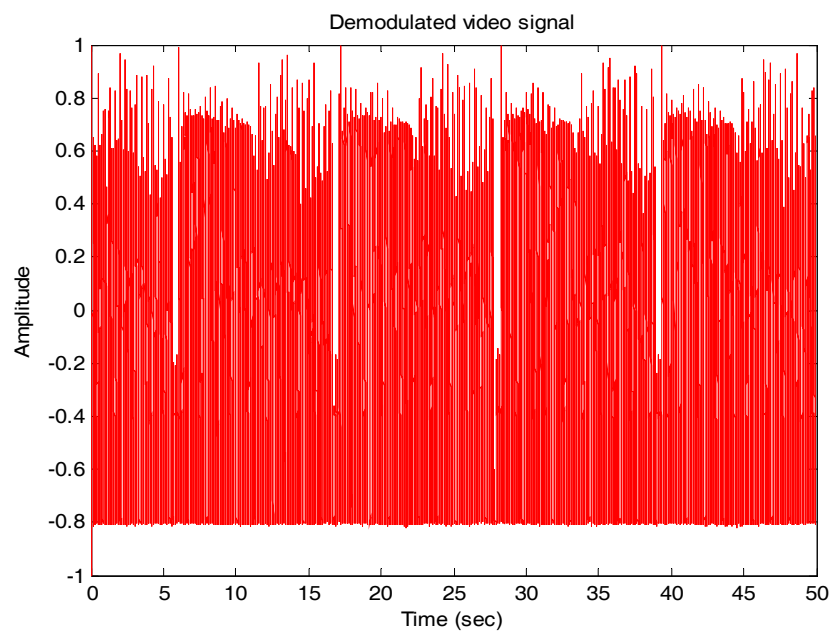
Figure 68.   Demodulated video signal (tangent-type demodulator).

100

Figure 69.   Demodulated video frame.

The phase response obtained from the video signal is shown in Figure 70. It is seen that the I and Q values are distributed on a symmetrical circle as expected. However, the circle obtained is not a perfect circle. There are even four points where the values are not on the circle. These points and the overall shape of the circle are attributed to the distortion introduced by the low-pass filtering process.
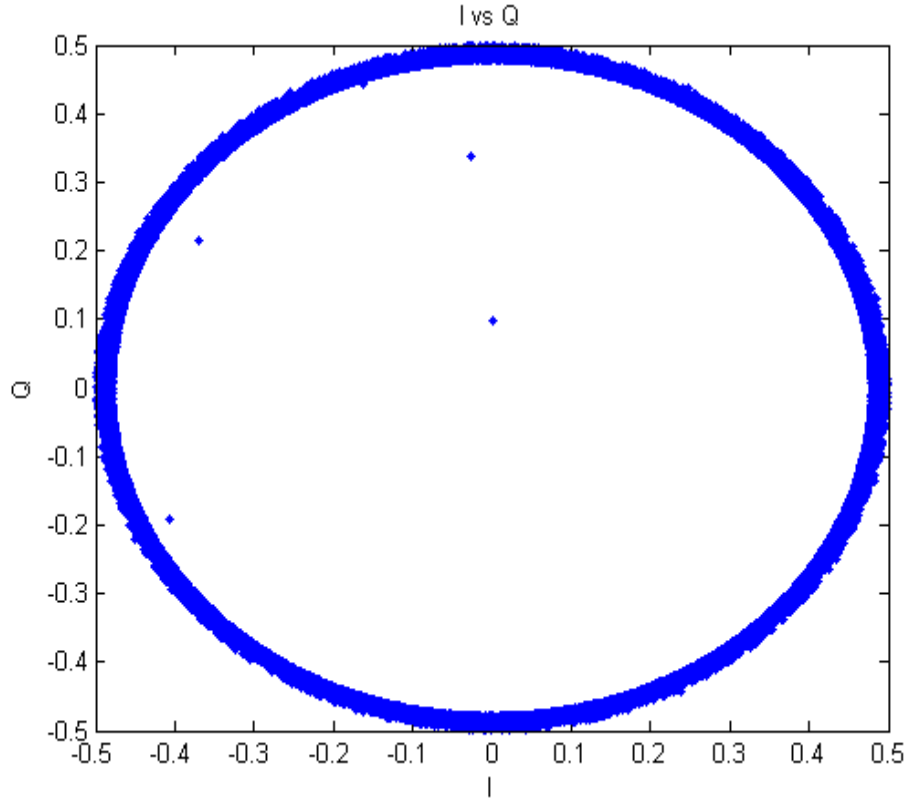
Figure 70.   *I / Q* circle obtained from tangent-type demodulation of the video signal.

b.   *LabView Simulations*

The video signal demodulation simulation that was performed in the previous section was repeated in LabView in order to verify the results obtained from MATLAB. A LabView VI was developed for performing the simulation of the tangent-type demodulator. The VI was developed based on the block diagram given in Figure 65. Different than the previous simulations, modulated video data is used as an input in this program. The modulation is done in MATLAB and the modulated video data is saved in a text file. This text file is then fed to the LabView VI and the data is used as the modulated video signal.

In the program, the modulated video signal is down-converted and *I* and *Q* channels are formed by the mixing and filtering processes. The implementation of file reading and signal mixing process is illustrated in the first part of the VI block diagram given in Figure 71. The VI also includes a single block which reads the original video data from the unmodulated video data file to plot the original video signal in order to compare with the demodulated signal. This block can be seen in the upper left section of Figure 71.
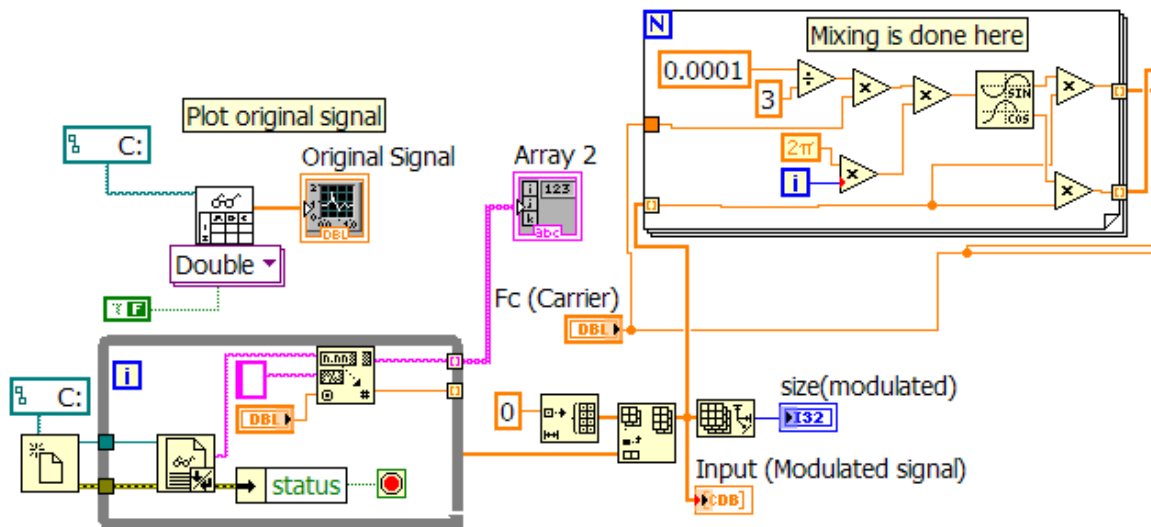
Figure 71.   Partial VI block diagram (Part 1) showing the file read and signal mixing process.

The *I* and *Q* channels obtained from the down-conversion process are then fed to the tangent-type demodulator. The output of the demodulator is differentiated and sent to another block for the improvement process. Finally, the dc offset that occurs in the demodulation process is removed and the resulting signal is amplified. The implementation of these processes is shown in the partial VI block diagram given in Figure 72.
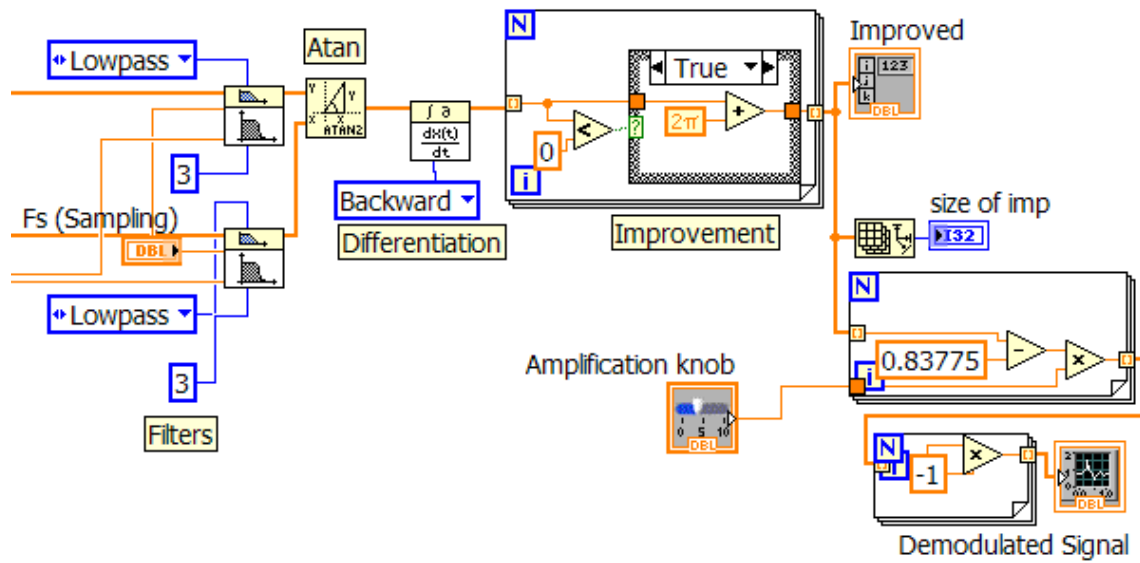
Figure 72. Partial VI block diagram (Part 2) showing the filtering, demodulation, improvement, dc offset and amplification process.

Similar to the MATLAB simulation, the carrier frequency, sampling rate and the frequency deviation used in the LabView simulation were 20 kHz, 100 kHz and 1 kHz, respectively. The modulation was done with MATLAB's *fmmod* function. The original video signal is plotted in Figure 73 and the demodulated video signal obtained from the tangent-type demodulator is shown in Figure 74. Comparing the two figures, we see that the video signal was recovered successfully using the tangent-type demodulation method.
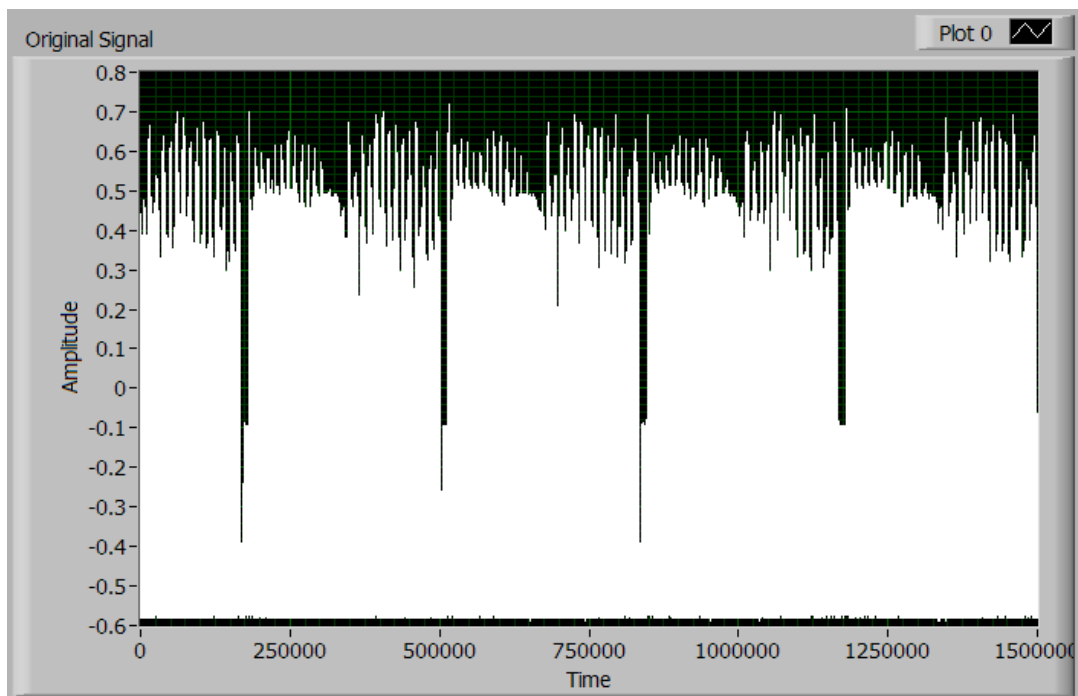
Figure 73.   Original video signal before modulation and demodulation.
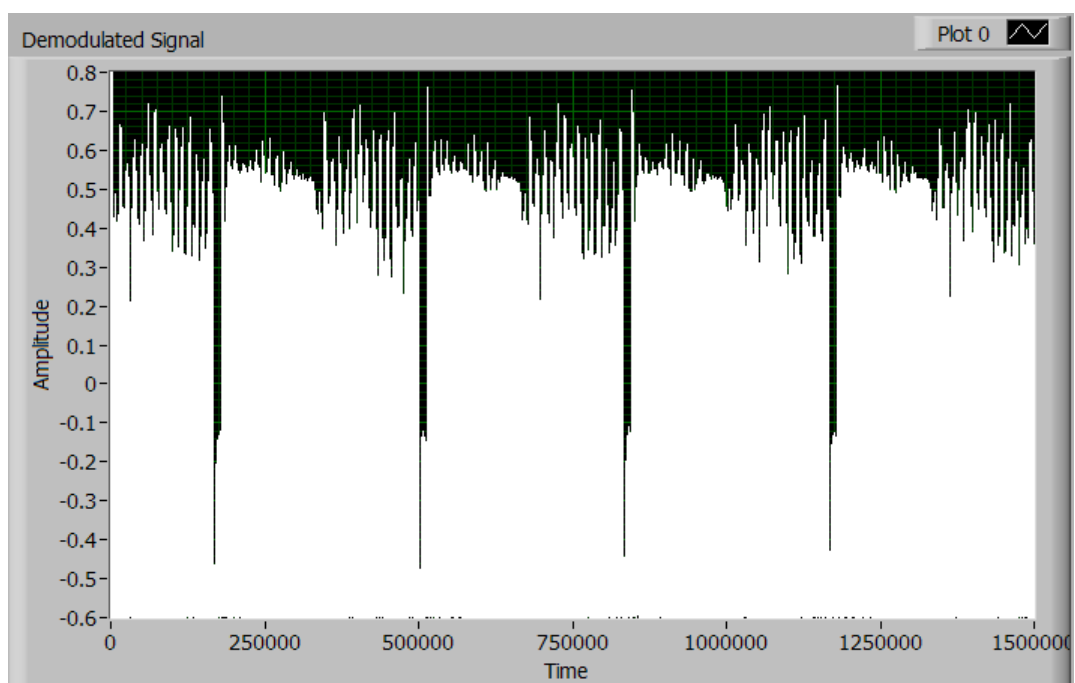
Figure 74.   Demodulated video signal obtained from tangent-type demodulator.

105

B. **SOFTWARE MODULES PERFORMANCE VERIFICATION TESTS AND RESULTS**

In Section A, the validation of the FM demodulation techniques were made. In this section, the verification of the software modules developed using these demodulation techniques is done by performing bench-top tests using the hardware. The user interfaces of the NTSC decoding module and the baseband demodulation module described in Chapter V were modified from their original version, which were given in [13], in order to provide more user friendliness.

1. **NTSC Decoding Module Tests**

The NTSC Decoding Module test was performed by using a video camera to acquire real-time video into the module. The test measures the ability of the module to receive a video data stream and display it on the screen. The output of the video camera was input into the PXI-5112 digitizers and the *NTSC Video Decode* VI introduced in Chapter V was run. In this test only one channel (i.e., channel 0) of the PXI-5112 digitizer was used.

The modified front panel of the NTSC decoding module is shown in Figure 75. The setup parameters needed for the sampling of the data from the PXI-5112 digitizers and displaying the video signal are located on the upper left of the front panel. The module has two displays on the right. The upper display shows the real-time video stream captured by the video camera. Below the display are the two settings required for the appropriate screening of the video stream. These are the "brightness level" and the "horizontal sync adjust." The horizontal sync adjust is an important setting, since an inappropriate setting of this parameter causes tilting of the image. An example of this tilting effect due to inadequate horizontal sync adjust is shown in Figure 76. The lower display shows the amplitude plot of the streaming video. This plot can be enabled or disabled by using the button located on the left of the front panel.
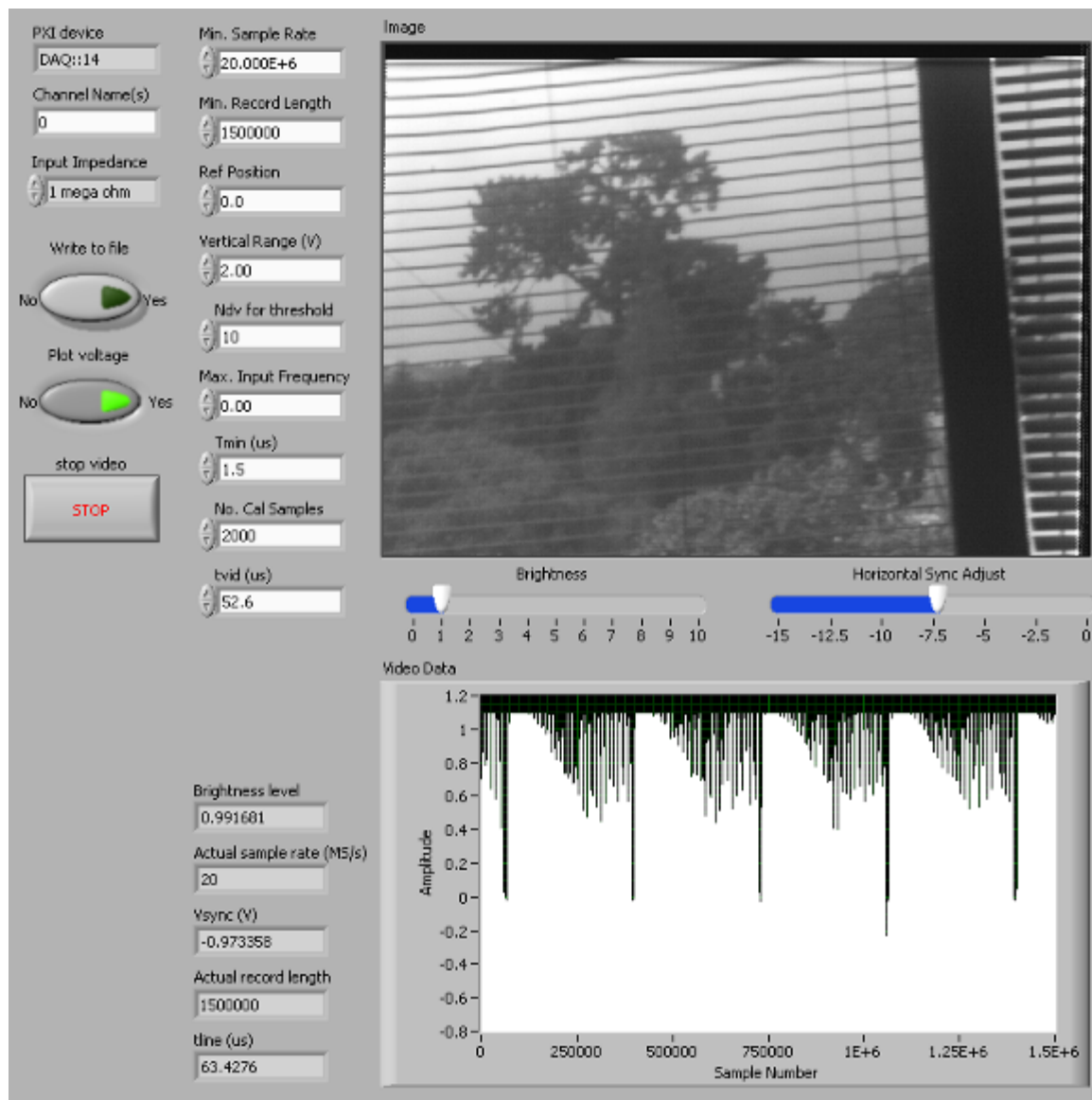
Figure 75.   Snapshot of the NTSC decoding module front panel while running.

Analyzing the video data plot verifies most of the features of the NTSC video signals discussed in Chapter IV. A close-up view of one of the vertical blanks seen in the video signal plot is shown in Figure 77. Here, the horizontal sync and the back porch regions that indicate the beginning of a new line can easily be observed. The sync pulses in the video signal region located to the right of the back porch region are also seen.

107

Figure 76.   Tilted video image due to inappropriate setting of
the horizontal sync adjust.
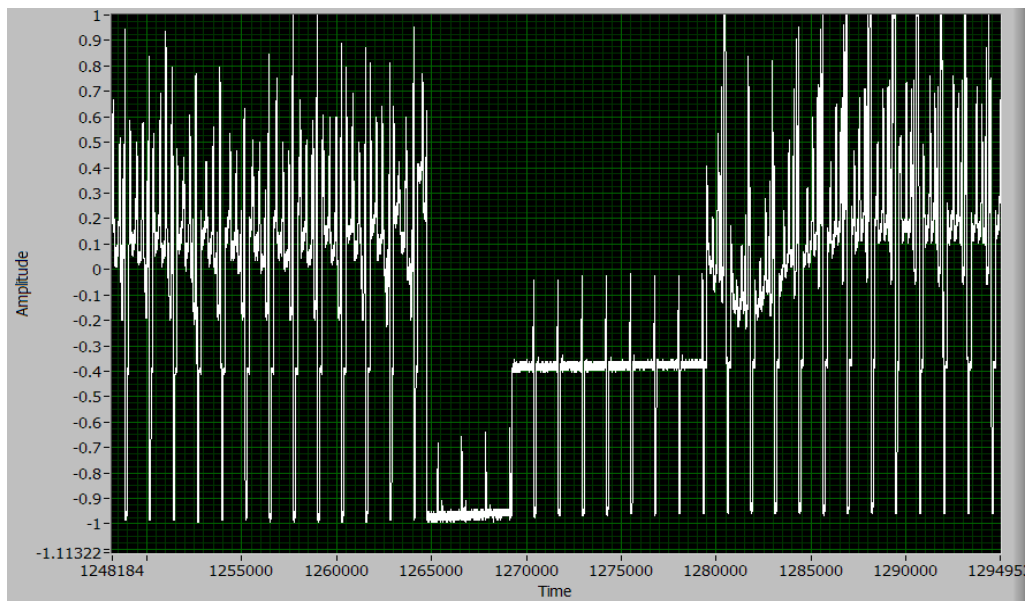
Figure 77.   Video signal region showing the beginning of a new field.

108

During the test process, we used a frame in which all objects were stationary for demonstrational purposes. The output obtained from the module was shown in Figure 75. For comparison, a still image of the same location was taken with a digital camera. This image is shown in Figure 78. It is seen that the module displays the image with enough accuracy. However, the quality of the image was traded off for frame-processing speed. To achieve faster processing, only one sample per pixel is used during the decoding process, which decreases the quality of the image.

Figure 78.   Digital camera image of the location captured by the video camera.

2.   FM Demodulation Module Tests

In this section, the operational testing of the two demodulation modules (i.e., baseband and tangent-type demodulation modules) introduced in Chapter V is given. Both modules were tested using only one array channel. Two different test procedures were performed. The antenna elements were not used in these tests. The setup diagram for the tests is shown in Figure 79. As shown in the setup diagram, the only difference between the two test procedures was the source of the modulating signal. In the first test, a signal generator was used to generate simple waveforms (e.g., sine, square, ramp waves). In the second test, a real-time video signal captured by a video camera was input into the synthesizer for FM modulation. In both tests, the modulated signal was up-converted to 2.4 GHz in order to simulate a transmission from a UAV. The FM signal obtained at the output of the synthesizer was input into the quadrature demodulator for frequency down-conversion to baseband. The quadrature demodulator was frequency synchronized by using an LO. The four signals obtained at the output of the quadrature demodulator were combined to construct I and Q signals and then sampled by the PXI-5112 digitizers. The digitized signals were then processed by the LabView VI for final demodulation. The details of the tests and the results obtained are discussed in the following sections.
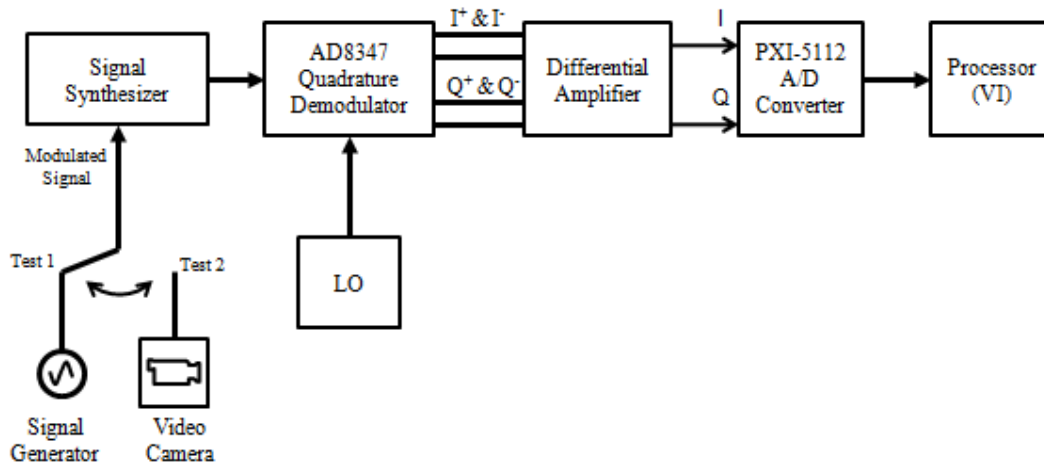
Figure 79.   Demodulation test set up.

a. *Baseband Demodulation Module Tests*

The baseband demodulation module introduced in Chapter V was tested as described in Figure 79. In the first test, a sine wave with a frequency of 50 kHz and amplitude 0.6 V peak-to-peak was generated using the signal generator. The amplitude of the signal was adjusted to prevent over-modulation. This signal was then fed into the signal synthesizer, which modulated the sine wave using FM, up-converting the signal to RF at 2.4 GHz. The baseband *I* and *Q* signals obtained from the quadrature demodulator were input into channels 0 and 1 of the PXI-5112 digitizers, respectively. The output obtained from the *FM Demod Single Fetch* VI is shown in Figure 80. An expanded version of the demodulated signal is shown in Figure 81.

Figure 80.   Output obtained from the *FM Demod Single Fetch* VI.

It is seen that the sine wave was recovered successfully by the module. The filter used in this test was a third-order Butterworth filter with 100-kHz cut-off frequency.
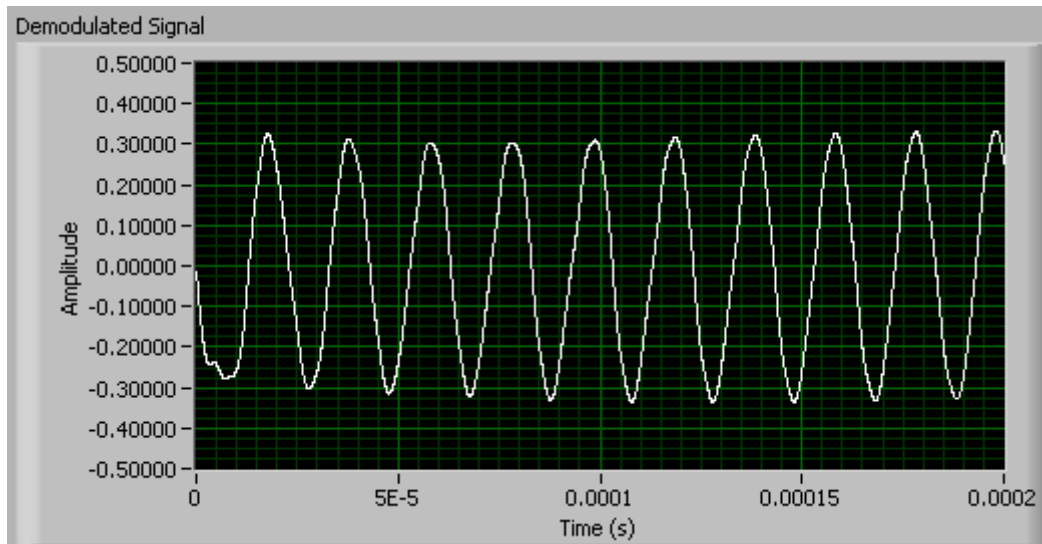
Figure 81.   Demodulated sine wave with 50-kHz frequency
and 0.6-V amplitude.

Since forming different waveforms is easy by using a signal generator, a square wave and a ramp wave were also tested. When 50 kHz was used as the frequency for these signals, the demodulated signals were distorted and looked more like a sine wave. For this reason a lower frequency (i.e., 20 kHz) was tried for the square and ramp waves. The outputs obtained from the module are given in Figure 82 and Figure 83. It is seen that the waves were not recovered accurately. However, for both waveforms, the fundamental frequencies of the input signals could be retrieved successfully. For the square wave, there were ripples with high magnitudes observed. However, these were attributed to the attenuation of the high-frequency components by the filter used in the module. Although the cut-off frequency was increased to several times the message frequency, the module failed to provide an accurate square wave. Similarly, with the ramp wave, there were distortions on the signal recovered. These distortions could not be eliminated by different filter settings either.

112

Figure 82.   Demodulated square wave obtained from
the baseband demodulation module.
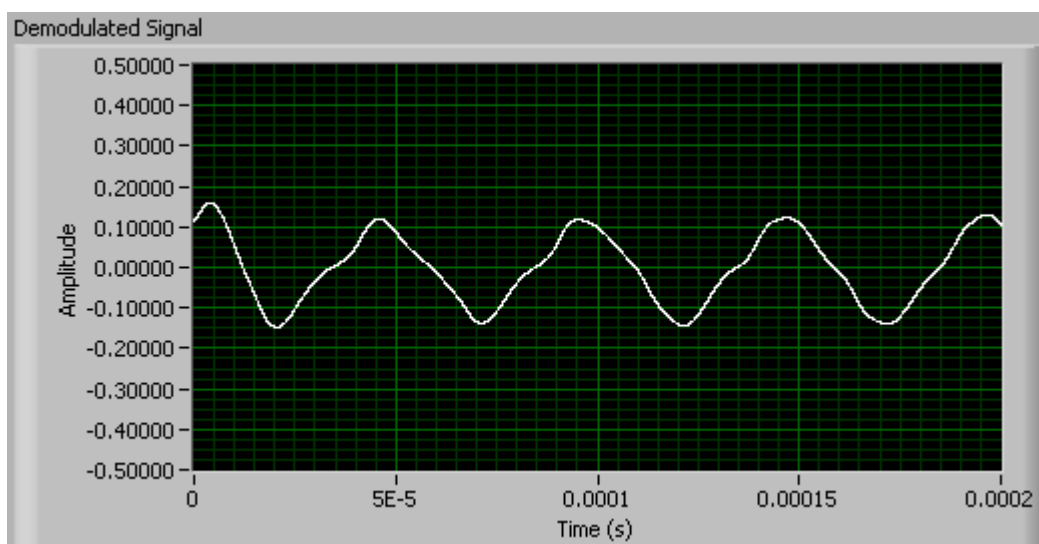
Figure 83.   Demodulated ramp wave obtained from
the baseband demodulation module.

The next tests performed consisted of using a real-time streaming video signal as the modulating signal. The video signal is known to be an NTSC-decoded video signal with 6-MHz bandwidth. For this reason, the filter used in the module was adjusted to have a low cut-off frequency of 9 MHz. It was also expected that the demodulated signal could be displayed by the *NTSC Processor* subVI located in the module.

When the test described in Figure 79 was run, it was seen that the output amplitude level of the video camera caused over-modulation in the signal synthesizer. In order to overcome this issue, a variable signal attenuator was placed between the video camera and the synthesizer. It was observed that 3-dB attenuation was sufficient to prevent over-modulation. A snapshot of the module while running is shown in Figure 84. An expanded view of the video signal obtained and a zoomed version, showing the horizontal sync and back porch regions, are shown in Figure 85 and Figure 86, respectively. It was seen that the video signal could not be recovered as expected from the simulations. The demodulated signal obtained had distortions, which caused the NTSC decoding module fail to decode and display the video stream.
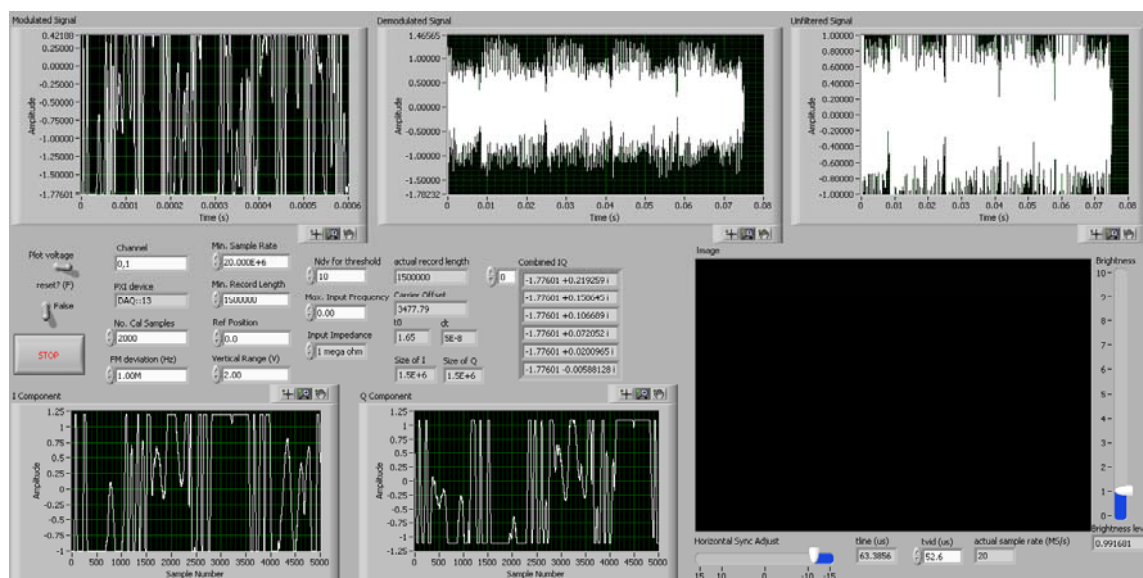
Figure 84.   Snapshot of the baseband demodulation module
running with video signal input.

114
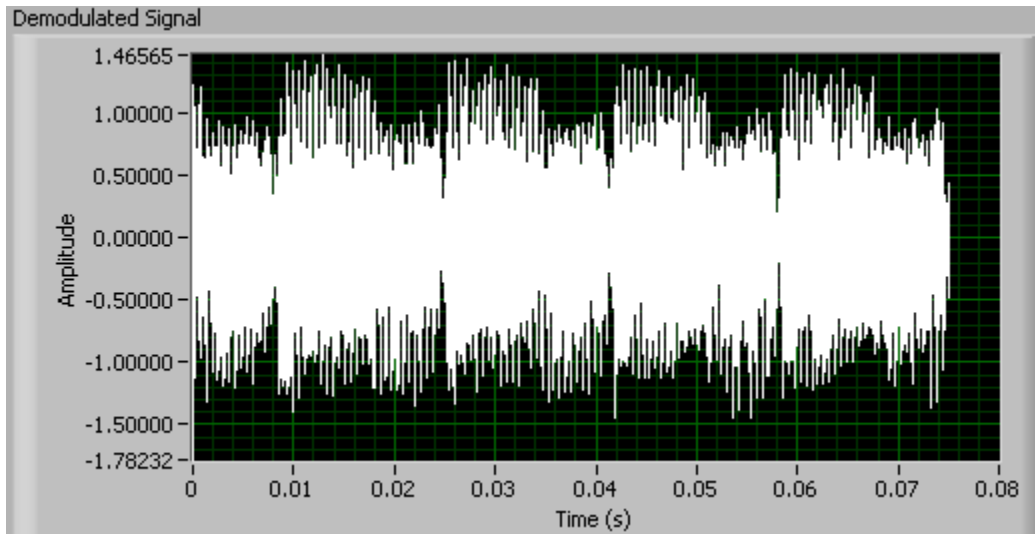
Figure 85. Demodulated video signal obtained from the baseband demodulation module with $f_{cut\text{-}off}$ = 9 MHz.
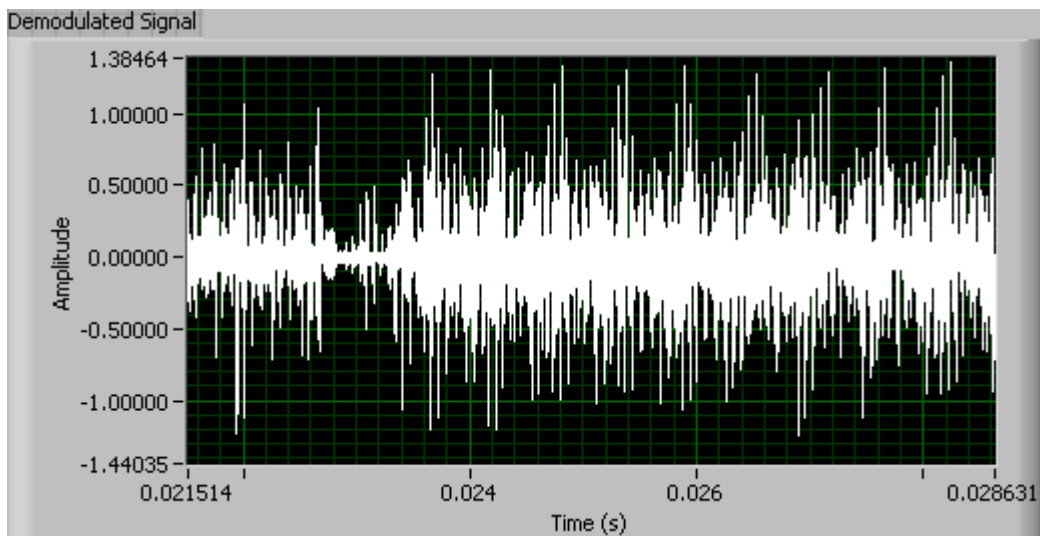
Figure 86. Zoomed video signal obtained from the baseband demodulation module with $f_{cut\text{-}off}$ = 9 MHz.

115

The distortion observed in Figure 85 and Figure 86 was attributed to the filter cut-off frequency being too high to filter the noise affecting the signal. In order to resolve this issue, the cut-off frequency was then decreased to 6 MHz and the test was repeated. The resulting video signal obtained is shown in Figure 87.
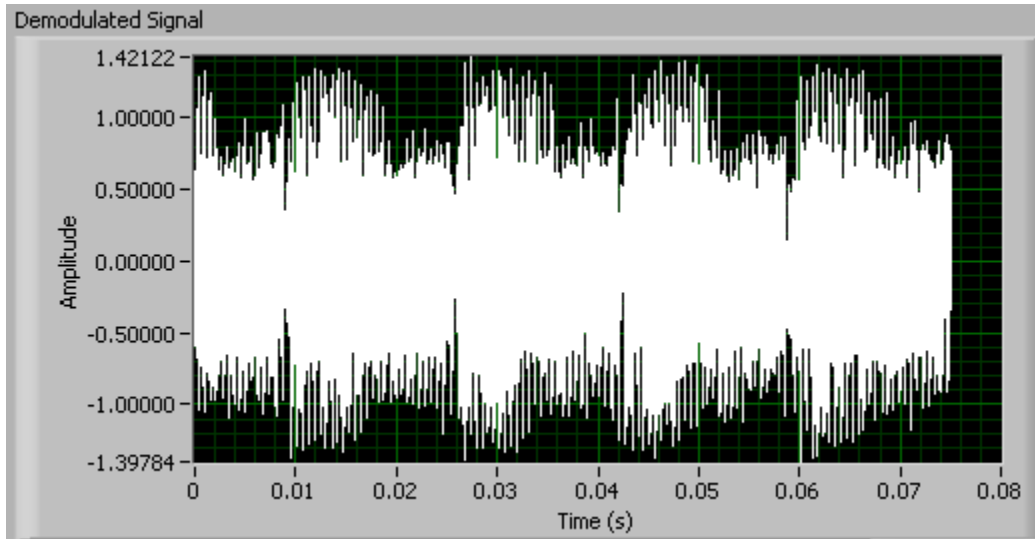
Figure 87.   Demodulated video signal obtained from the baseband
demodulation module with $f_{cut\text{-}off}$ = 6 MHz.

From Figure 87 it was seen that lowering the filter cut-off frequency did not have a significant effect. As a final test, it was decided to set the filter cut-off frequency to a very low value. The cut-off frequency chosen for this was 100 kHz. The resulting video signal obtained is shown in Figure 88.
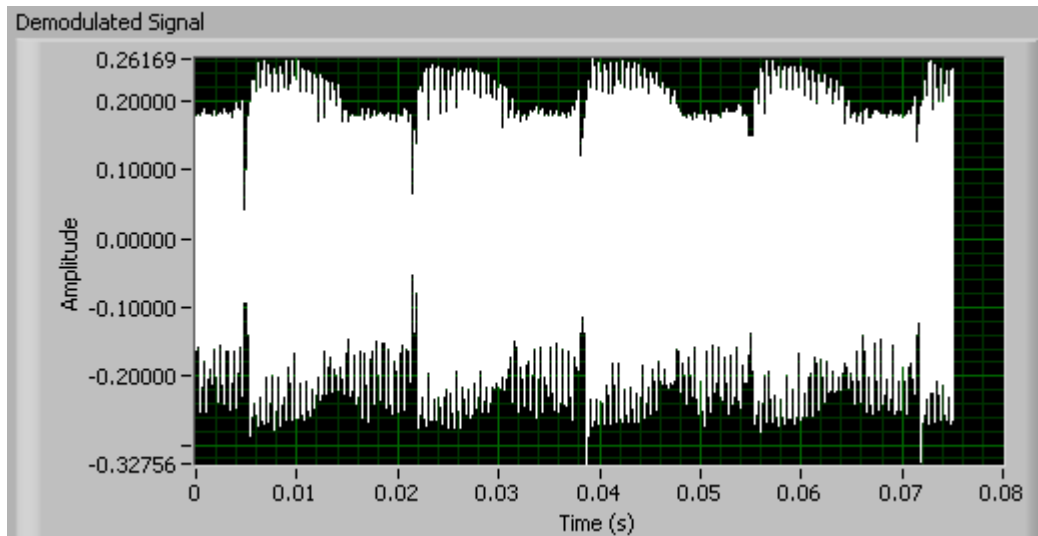
Figure 88.   Demodulated video signal obtained from the baseband
demodulation module with $f_{cut\text{-}off} = 100$ kHz.

A close-up view of the video signal given in Figure 88 is shown in Figure
89. Comparing this with the original video signal given previously in Figure 77, it is seen
that the demodulated signal is still too distorted to be decoded.
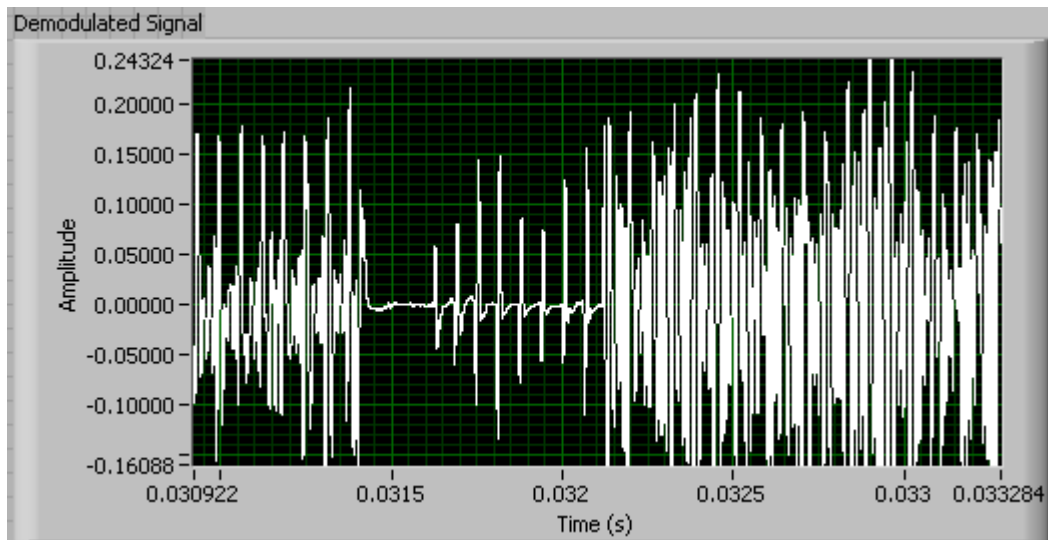
Figure 89.   Zoomed video signal obtained from the baseband demodulation
module with $f_{cut\text{-}off} = 100$ kHz zoomed.

117

b.   *Tangent-type Demodulator Tests*

The tangent-type demodulation module introduced in Chapter V was tested as described in Figure 79. Similar to the previous module test, a sine wave with a frequency of 50 kHz and amplitude 0.6 V peak-to-peak was generated using the signal generator. The amplitude of the signal was adjusted to prevent over-modulation. This signal was then fed to the signal synthesizer for modulation and up-conversion to RF at 2.4 GHz. The baseband *I* and *Q* signals obtained from the quadrature demodulator were input into channels 0 and 1 of the PXI-5112 digitizer, respectively. The output obtained from the *FM Demod Single Fetch Tangent* VI is shown in Figure 90. An expanded version of the demodulated signal is shown in Figure 91.
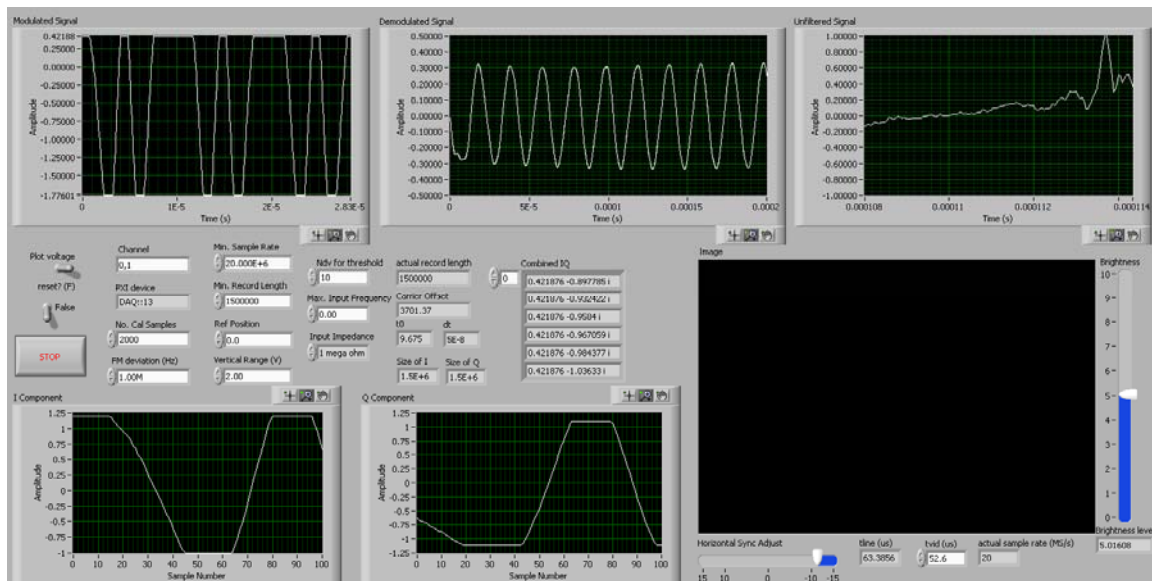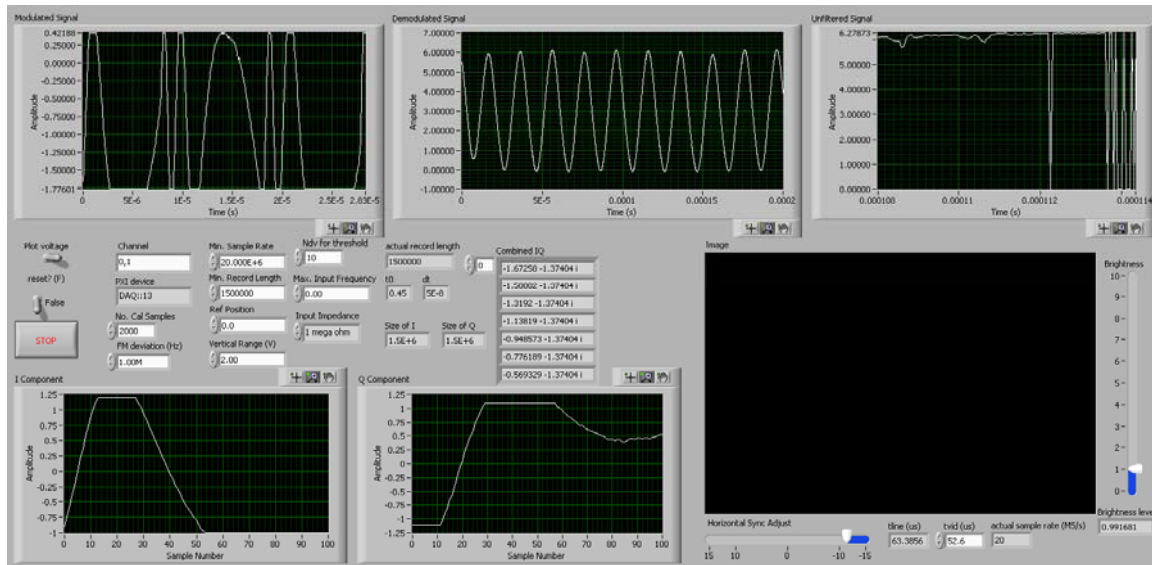

Figure 90.   Output obtained from the *FM Demod Single Fetch Tangent* VI.

It is seen that the sine wave was recovered by the module. The same third-order Butterworth filter $(f_{cut-off} = 100 \text{ kHz})$ used in the previous test was used to filter the demodulated signal.
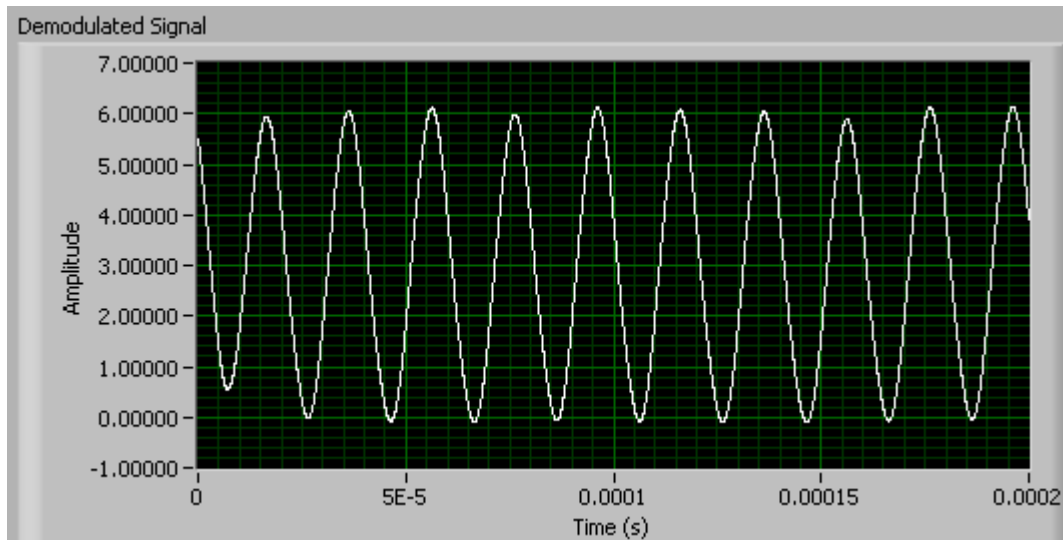
Figure 91.   Demodulated sine wave with 50-kHz frequency.

The same tests utilizing the 50-kHz square and ramp waves were repeated for the tangent-type demodulation module. The outputs obtained from the module are given in Figure 92 and Figure 93. It is seen that the waveforms were not recovered accurately. However, in both situations, the fundamental frequencies of the input signals could be retrieved successfully. As seen from Figure 92, the square wave has distortions at the amplitude peaks. Initially, these were attributed to the attenuation of the high-frequency components by the filter. Although the cut-off frequency was changed and several experiments were done, the module failed to provide an accurate square wave. Similarly with the ramp wave, there were distortions on the signal recovered as well. The recovered waveform looks like a sine wave rather than a ramp wave at the peaks and lows. This distortion is considered as caused by the filter.
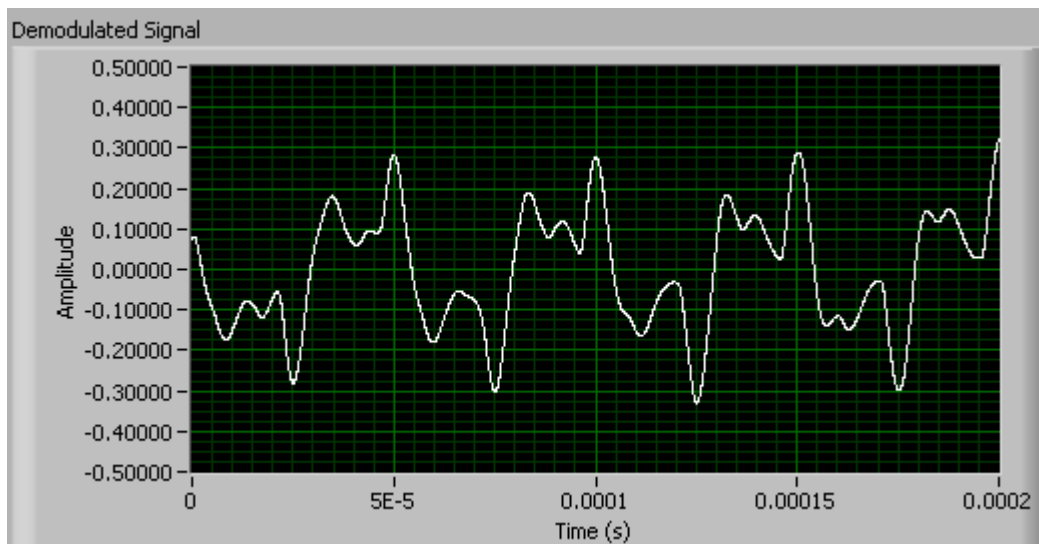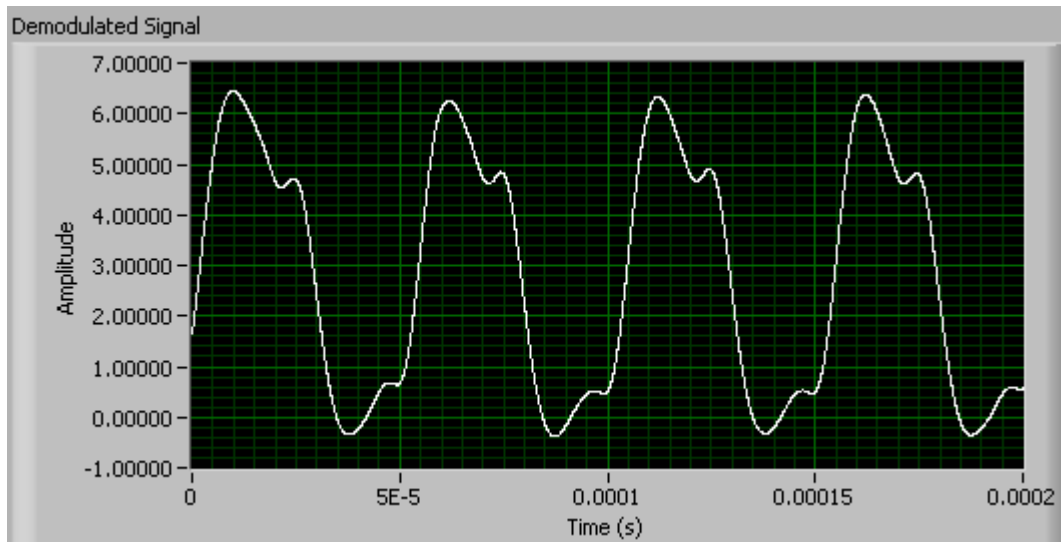
Figure 92.   Demodulated square wave obtained from the
tangent-type demodulation module.
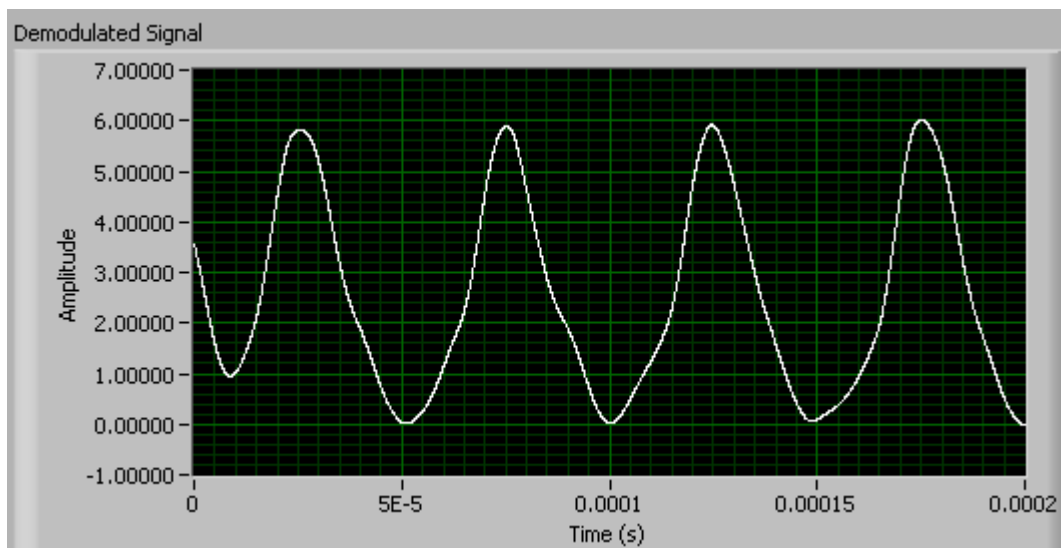
Figure 93.   Demodulated ramp wave obtained from the
tangent-type demodulation module.

In the next test, the real-time streaming video signal was used as the modulating signal. The filter cut-off frequency was adjusted to 9 MHz since the video signal has a 6-MHz bandwidth. Similar to the previous test with video signals, a variable signal attenuator was placed between the video camera and the synthesizer to prevent over-modulation. Then attenuation of 3 dB was applied to the output of the video camera. A snapshot of the module while running is shown in Figure 94. An expanded version of the demodulated video signal obtained is also shown in Figure 95. It was seen that the demodulated video signal obtained had excessive level of distortions. The distortions corrupted the sync pulses and the NTSC decoding module failed to decode and display the video.
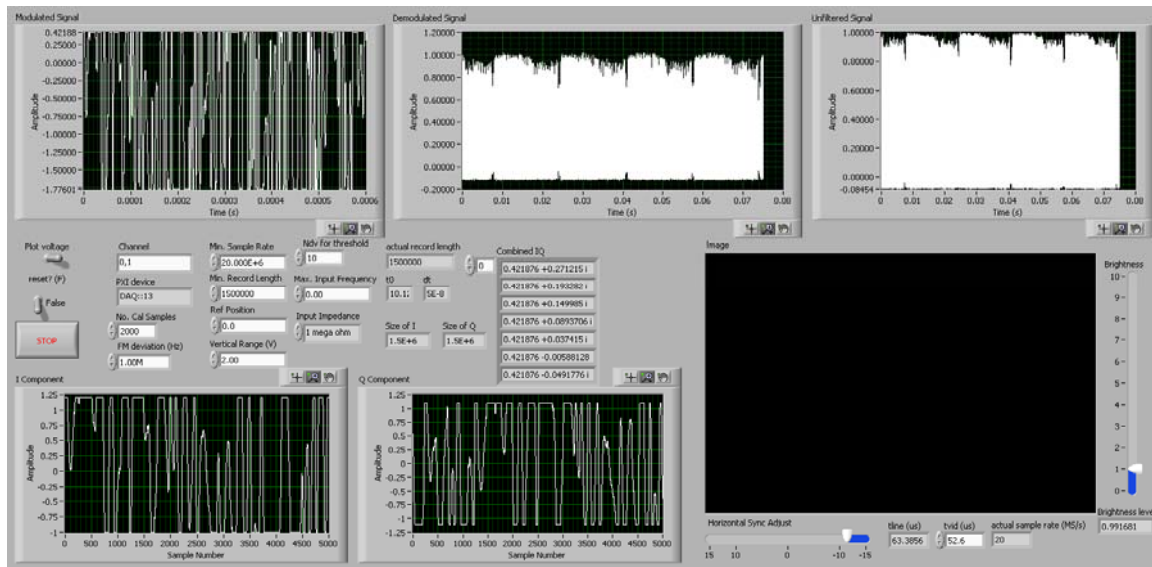
Figure 94.   Snapshot of the tangent-type demodulation module
with video input ($f_{cut\text{-}off}$ = 9 MHz).

121
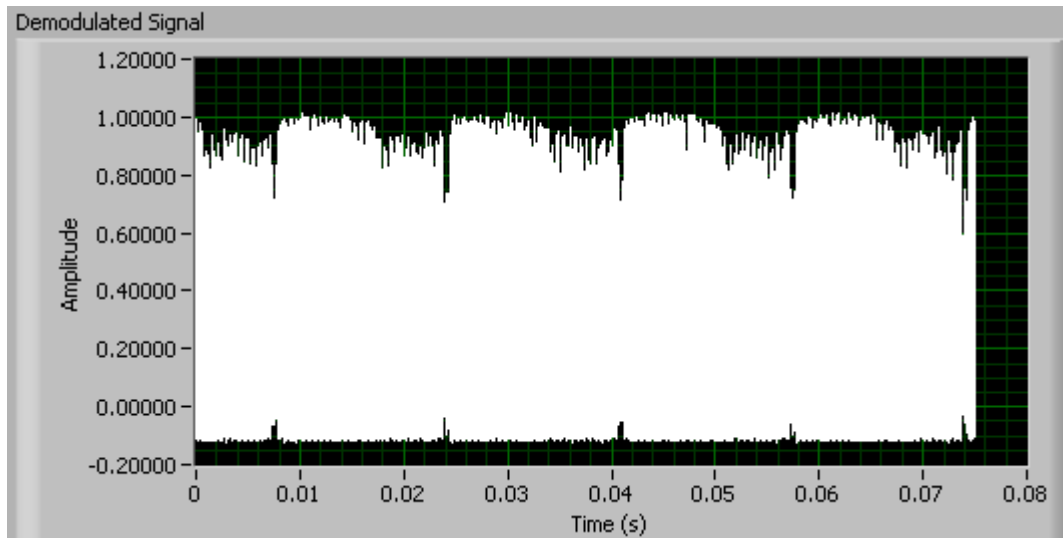
Figure 95.   Demodulated video signal obtained from the tangent-type
demodulation module ($f_{cut-off}$ = 9 MHz).

Similar to the previous situation encountered with the baseband demodulation module, the filter cut-off frequency was decreased down to 100 kHz to reduce the distortions and the test was repeated. The resulting demodulated signal is shown in Figure 96 and Figure 97 (zoomed).
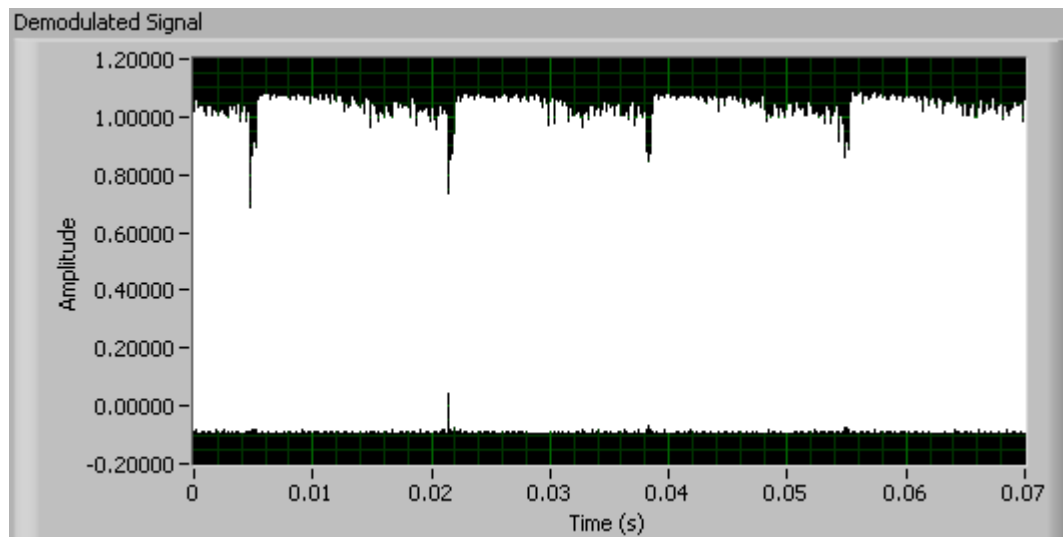
Figure 96.   Demodulated video signal obtained from the tangent-type
demodulation module ($f_{cut-off}$ = 100 kHz).
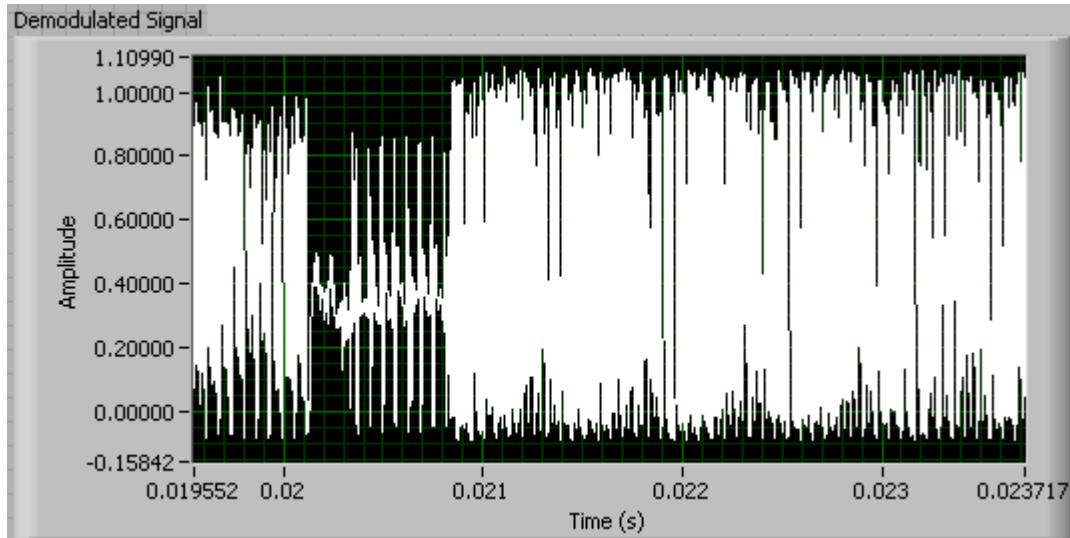
Figure 97.   Zoomed view of the video signal obtained from the tangent-type demodulation module ($f_{cut\text{-}off}$ = 100 kHz).

It was observed that, once again, the noise problem affected the results negatively even though the filter cut-off frequency was set very low. The demodulated video signal could not be decoded and displayed by the NTSC decoding module.

C.   SUMMARY OF RESULTS

In Section A of this chapter, the software simulations needed to validate application of the FM demodulation modules introduced in Chapter V were performed. The results showed that both the baseband and tangent-type demodulation techniques can be used for the demodulation of FM video signals.

After the validation of the demodulation methods, in Section B the verification of the functionality of the software modules developed based on the simulations was given. It was seen that both modules showed similar performances. Both modules were able to retrieve the sinusoidal signal used as the modulating signal. However, distortions were observed when square and ramp waves were used. On the other hand, the fundamental frequencies of the square and ramp waves were retrieved successfully. When a real-time streaming video signal was used as the modulating signal, the modules were able to

123

provide the demodulated video signal back at the output. However, the signals obtained could not be decoded by the NTSC decoding module. In Section C.3 of Chapter V, it was mentioned that the video decoder measures the duration of the sync pulses in the video signal and compares this duration with the minimum duration required for a valid sync pulse. If the measured duration is not greater than this minimum pulse duration, the pulse is considered as noise. Because of the excessive noise on the demodulated signal, the video decoder failed to validate the pulses as sync pulses since it cannot measure a pulse duration that is greater than the minimum duration for a valid sync pulse. Hence the pulses were considered as noise and as a result the video could not be displayed.

A slight improvement was achieved by decreasing the low-cut-off frequency of the filter used in the module; however the video stream could not still be displayed. The fact that the baseband video signals can be frequency modulated and successfully recovered indicates that the demodulation software is operating as expected. There are several sources of error that could be causing the poor quality of the signal when hardware is used:

1. The quality of the FM signal out of the signal generator is unknown. Distortions may have occurred before demodulation.
2. The signal generator may be applying pre-emphasis increasing the magnitude of the high-frequency components in order to improve the overall SNR.
3. The demodulator noise is too high and more samples/pixels may need to be collected.
4. Frequency offset between the incoming RF and LO may cause problems. Simulations of this effect in MATLAB and LabView have indicated that the demodulation process is very tolerant to a shift in frequency (up to 200 kHz).

In Chapter VII, a summary of the overall research presented in this thesis is given and conclusions are made, along with recommendations for future work.

124

VII. CONCLUSIONS AND RECOMMENDATIONS

In this chapter, a summary of the research presented in this thesis is given and conclusions, along with future recommendations, are made.

A. SUMMARY AND CONCLUSIONS

UAVs play an important role in modern military warfare. They provide a high degree of situational awareness by carrying out surveillance and reconnaissance missions that lead to gaining air dominance against adversaries. The ability to gain air dominance is crucial in the sense that it saves lives and affects the length of the conflict. In order for a UAV to accomplish its surveillance and reconnaissance mission, the data link between the UAV and the GCS must remain uninterrupted and provide a reliable information transfer. An antenna with tracking capability is a good solution to sustain this datalink.

The ultimate objective of the ongoing project presented in this thesis is to develop a digital tracking antenna array for use in communications with a UAV, using COTS components. The research previously done in key areas included RSNS and DBF for direction finding and tracking as well as demodulation and decoding techniques for video data transmission. The research presented in this thesis focused on the development of the demodulation techniques in order to allow the digital tracking array to successfully retrieve and display the video data embedded in the FM signals received by the antenna. An in-depth review of the properties and functionalities of the current system and its components was also covered in order to provide a useful reference for future studies.

The feasibility of utilizing new demodulation techniques for the demodulation of the video signals was investigated. The tangent-type demodulation technique was studied as a new approach for the demodulation process. The previous baseband FM demodulation technique was enhanced to handle video signals. The applicability of these two techniques in the receiver system was validated by computer simulations done in

125

MATLAB and LabView. It was seen that FM video signals received from a UAV can be demodulated by using both the baseband and tangent-type demodulation techniques.

The modular approach used in the previous studies for the development of the software modules for the receiver processor was maintained. Based on the results of the simulations, an FM demodulation module utilizing the tangent-type demodulation technique for the demodulation of FM video signals was developed. Additionally, the previous FM demodulation module using the baseband demodulation technique with a sinusoidal input waveform was modified to handle video signals. Both modules were operated on a single channel. Subsequently, both modules were tested using a bench-top test set up. Different waveforms were used as input modulating signals. These included sine, square and ramp waves and real-time streaming video signal. The newly developed tangent-type FM demodulation module showed similar performance compared to the previous baseband demodulation module. Both modules were able to demodulate the sine wave. The demodulated square and ramp waves by both modules had distortions due to the attenuation of high-frequency components. However, the fundamental frequencies of both waves were retrieved. The video signal used as the modulating signal was recovered using both demodulators. However, the signals obtained were of poor quality, which prevented decoding of the video data. The filter cut-off frequencies were decreased to eliminate the high-frequency noise. A slight improvement was obtained; however, the sync pulses were still distorted preventing the video data from being decoded and displayed.

The development process also included the modification of the user interfaces of the previously developed modules. The previous user interfaces of the NTSC decoding module and the baseband FM demodulation module were examined and modified to provide more efficient functionality and analysis. The functionality of the modified NTSC decoding module was tested using a bench-top test setup. The functionality of the module was verified using unmodulated streaming video obtained from a video camera

126

as the input. However, when integrated within the demodulation modules, the module failed to decode and display the demodulated video obtained at the output of the demodulators.

B.   RECOMMENDATIONS FOR FUTURE WORK

In order to reach the ultimate goal of developing a digital tracking array that has the capability to acquire, track and demodulate the FM video signals coming from a UAV, research and studies in the following areas are recommended. The recommendations presented cover not only improving the areas studied in this research, but also enhancing overall system performance.

1.   FM Demodulation Modules

Currently, the video signal obtained from the baseband and tangent-type FM demodulation modules cannot be decoded by the NTSC decoding module. As a result, the streaming video cannot be displayed on the screen. The noise problem was considered to be the reason for this issue. Since the NTSC decoding module functionality with unmodulated video signals was verified by bench-top tests, emphasis should be given to improving the quality of the demodulated video signal by eliminating noise and making it compatible with the NTSC decoding module. Concentration can be focused on improving the quality of the vertical sync pulses included in the demodulated video signal. Also the Vsync level computed by the *Fetch from 5112* subVI should be the proper value for the demodulated video signal. The computation is currently done according to the input video signal. However, the Vsync computed is used in the *NTSC Processor* subVI to display the demodulated video. It is possible that the amplitude level of the demodulated video signal may not match the Vsync level delivered by the *Fetch from 5112* subVI. Future work can include developing a method to calculate the Vsync value according to the demodulated video signal. Once this is done, the software modules can easily be updated and integrated into the system.

2. NTSC Decoding Module

The NTSC decoding module is capable of decoding and displaying video data in black and white. Further studies could focus on modifying the module to have the capability of processing color information.

3. Quality of the FM Signal

In the hardware tests, the frequency modulation was done using the HP 8341B Frequency Synthesizer to simulate the data transmission from a UAV. The video signal out of the camera was fed to 8341B and the frequency modulated signal obtained was fed to the AD8347 quadrature demodulator. However, the quality of the FM signal provided by the 8341B was unknown. Future work may include the assessment of the FM signal quality obtained from the signal generators. Additional tests can be performed using a different signal generator for frequency modulation in order to compare the quality of the FM signal. The specifications of the signal generators used should be checked carefully before performing the hardware tests. The input signal frequency range should be able to include the video signal bandwidth (i.e., 6 MHz). Similarly, the input signal amplitude range should cover $+/-$ 2 volts.

4. Other System Enhancements

From an overall system perspective, there are several fields for research and development that can be explored to extend the capabilities of the digital tracking array antenna system. The values used for the moduli in the RSNS module can be increased in order to decrease the bin size, which therefore provides the antenna array the capability to track the incoming signal with higher accuracy. Another improvement for the tracking aspect can be achieved by making the monopulse slope constant dynamically change according to the current scan angle. This provides faster convergence compared to using a constant value for the slope constant.

128

As the new COTS equipment with better specifications become available for low prices in time, the COTS equipment used in the digital tracking array system can be replaced with new equipment with better performance. For example, the quadrature demodulators used in the system can be replaced with new demodulators having higher second-order input intercept point (IIP2) specifications. This can decrease the amount of second-order distortion and improve the performance of the quadrature demodulators. Similarly, new and faster A/D digitizers, which have higher resolution, can replace the current PXI-5112 digitizers to obtain lower noise and better sensitivity. Also, an A/D digitizer with a higher sampling rate (i.e. twice the carrier frequency) can provide anti-aliasing of the acquired signals at high frequencies and eliminate the need for a separate hardware demodulator.

THIS PAGE INTENTIONALLY LEFT BLANK

APPENDIX: MATLAB CODES

A. MATLAB CODE FOR THE SIMULATION OF BASEBAND DEMODULATION USING A 50 KHZ SINE WAVE

```matlab
% fm_demod_BB_sine_wave.m
%
%************************************************************************
%This m file is used to simulate Baseband FM demodulation. A sine     *
%wave is created as the modulating signal and demodulated using       *
%baseband demodulation                                                *
%                                                                     *
%Original version by: David C. Jenn (Professor ECE Department, NPS)   *
%Edited by: Fevzi Aytaç KAYA / 1st LT. / Turkish Air Force / 2010     *
%************************************************************************


clear
Fs = 1500000; % Sampling rate of signal
dt=1/Fs;
fm=50000;      %modulating signal freq.
omegam=2*pi*fm;
dev = 20000; % Frequency deviation in modulated signal
disp(['deviation: ',num2str(dev)])
T=5*1/fm;     % total observation time
t0=0;
t = [0:dt:T]'+t0;
Nt=length(t);  % Number of time samples
disp(['time step (us): ',num2str(dt/1e-6)])
% single tone message signal
beta=dev/fm;
disp(['beta=',num2str(beta)])

m=cos(omegam*t);  % message signal
mi=sin(omegam*t);  % integral of message

%Modulated signal
theta=dev*mi.*t;
Noise=wgn(length(theta),2,-200);
I=cos(theta)+Noise(:,1);
Q=sin(theta)+Noise(:,2);

% plot FM modulated BB signal
figure(1), clf
clf
plot(t,I,t,Q)
xlabel('Time, sec')
ylabel('Modulated Signal, volts')
```

```matlab
title('Modulated signals')
legend('I','Q')
axis([t0,t0+T,-1,1])
thr0=atan2(Q,I+1e-10)+pi;    % 0 to 2*pi
thr=unwrap(thr0);

% recover using I and Q
for i=2:Nt
    dQdt=(Q(i)-Q(i-1));
    dIdt=(I(i)-I(i-1));
    Ia=(I(i)+I(i-1))/2;
    Qa=(Q(i)+Q(i-1))/2;

    % Baseband demodulation formula
    mr(i-1)=(Ia*dQdt-Qa*dIdt)/2/pi/t(i);
end

mr=mr/660;  %Set this to adjust output amplitude

% plot demodulated signal
figure(2), clf
clf
plot(t,m,'b-',t(1:Nt-1),mr,'r-')
xlabel('Time, sec')
ylabel('Message Signal, volts')
title('Message signals')
legend('Original','Demodulated');
axis([t0,t0+T,-2,2])

%I vs. Q can be plotted by uncommenting the following
% figure(3)
% plot(I,Q,'.');
% title('I vs Q')
```

B. MATLAB CODE FOR DISPLAYING VIDEO FRAMES

```matlab
% NTSC_video_display.m
% Written by David C. Jenn Professor, NPS  (11/23/08)
% uses floating point raw data from 5112
% read NTSC data and process sequentially
% SIMULATING STREAMING DATA
% WORKS for all combinations of field
% time reset added
clear
% setup PXI-5112 data read
fs=20e6;
dt=1/fs/1e-6;                          % sample time in microseconds
dv=2/2^8;                              % voltage quantization interval
% load matlab file already read from text file
disp('reading text file ...');
V0=dlmread('TextFile7.txt');
Ns=length(V0);           % number of samples read in from file
X=[1:640];
Y=[1:480];
Nlines=259;              % starting at first FULL line of video (so not
260)
tpix=52.6/640;           % pixel time in microseconds
tline=63.5;              % complete line of data
Tmin=1.5;                % pulses < Tmin are noise
% initialize counters and flags
nfld=0;                  % =0 searching for even field; =1 searching for
odd
frame=0;                 % counts frame number
isy=1;                   % set isy=0 if a start of field (end of long
pulse)
lnn=0;                   % counts lines in the current frame
npix=1;                  % counts pixels in the current line
iproc=1;                 % =0 processing, =1 searching
% use the first few lines to find sync and blanking level for this file
Vmin=V0(1);
 for nn=1:floor(tline/dt)+10
     if V0(nn)<Vmin, Vmin=V0(nn); end
 end
 Vsync=Vmin+10*dv;
 disp(['Vsync=',num2str(Vsync)])
% -------------- PROCESS STREAMING DATA ------------------------------
 n=1;                    % sample index of data from 5112 ADC
 t=0;                    % time in microseconds
 V=V0(1);
 tb=0;
 TS=0;
 TE=0;
 TSo=0;
 TEo=0;
```

133

```matlab
    Tmin=1;
    isy=1;
    V=V0(1);
    Vmax=max(V0);
    while n<Ns-1
        n=n+1;
        t=t+dt;                  % new time
        tb=tb+dt;                % blanking sample counter
        Vo=V;
        V=V0(n);                 % new voltage point
    if floor(n/50000)==(n/50000), disp(['n=',num2str(n)]), end

    if iproc==1
        if V<=Vsync & Vo>Vsync        % first point below threshold
            TSo=TS;
            TS=t;                     % samples below threshold
            NS=n;
            isy=1;                    % potential start point
        end
        if V>Vsync & Vo<=Vsync        % step up
            TEo=TE;
            TE=t;
            isy=0;                    % potential stop point
        end
    % determine if this is a valid pulse or just a noise spike
        if isy==0
            dsp=TS-TEo;          % width of up spike or sync pulse spacing
            if dsp<Tmin
                TS=TSo;
                isy=1;
            end
        end
        if isy==0
            if dsp>=Tmin                 % valid sync pulse
                isy=1;
                if TEo-TSo>3.5*tline
                    disp('new field')
                    isy=1;
                    lnn=1;
                    TEo=TEo-TS;
                    TSo=TSo-TS;
                    TE=TE-TS;
                    t=t-TS;               % reset time reference
                    TS=0;
                    tb=0;
                    if TE-TEo<.75*tline
                        disp('odd')
                        itype=1;
                    end
                    if TE-TEo>=.75*tline
                        disp('even')
                        itype=0;
```

134

```matlab
                    end
                    if nfld==0 & itype==0, iproc=0; end
                    if nfld==1 & itype==1, iproc=0; end
                end
            end
        end
    end    % end of iproc
    % blanking level for this frame
        if tb>tline/2 & tb<=tline/2+dt
            Vb=V; disp(['Vb=',num2str(Vb)]);
            Vwht=14/4*(Vb-Vsync)+Vsync;
        end
    if isy==1 & iproc==0
        t1=2*4.7+1+(lnn-1)*63.42;  % start time of video data for this
line
        t2=t1+52.6;                 % end time of video data for this line
            if (t>=t1 & t<=t2)      % time window for line lnn
                tp1=t1+(npix-1)*tpix;    % start time of pixel number npix
                tp2=tp1+tpix;
                    if t>=tp1 & t<=tp2     % in pixel npix
                        npix=npix+1;
                        Vp=V;                  % 0<=V<=1 black to white
                            if itype==1, P(2*lnn-1,npix)=Vp/Vmax*1.5; end
                            if itype==0, P(2*lnn,npix)=Vp/Vmax*1.5; end
                        end
                    if npix==640            % finished with this line
                        npix=1;             % restart pixel counter
                        lnn=lnn+1;
                    end
                end
            if lnn==Nlines              % finished with this field
                lnn=1;
                isy=1;
                nfld=nfld+1;
                iproc=1;                % look for start of next field
            end
% if an odd field was processed then a complete frame is collected so
plot
            if nfld==2
                disp(['completed frame number: ',num2str(frame)])
                frame=frame+1;
                figure(frame), clf
                imagesc(X,Y,abs(P(12:516,1:640)));
                colormap(gray);
                axis off
                title(['Frame number: ',num2str(frame)])
                nfld=0;
            end
    end
end                                         % end data loop
disp('OUT OF DATA BEFORE END OF FIELD PROCESSED -- INCOMPLETE FRAME')
```

THIS PAGE INTENTIONALLY LEFT BLANK

C. MATLAB CODE FOR THE SIMULATION OF BASEBAND DEMODULATION OF A VIDEO SIGNAL

```matlab
% fm_demod_BB_video_data.m
%
%***********************************************************************
%This m file is used to simulate Baseband FM demodulation.          *
%A video data file (in txt format) is required for the input.       *
%                                                                    *
%Written by: Fevzi Aytaç KAYA / 1st LT. / Turkish Air Force / 2010
*%***********************************************************************
*

tic
clear
clc
%Amplification set here
volume_knob=1;  % Range 1-30 (suggested)
%Read modulating signal data from text file
AA=dlmread('video_data.txt');     %File name is video_data.txt
n1=1; n2=length(AA);
V=AA(n1:n2);
clear AA
t=1e-4*[0:length(V)-1]';
Vmax=max(V); Vmin=min(V); V0=max([Vmax,abs(Vmin)]);
X=V/V0;    %normalize
M=3;       %interpolation factor
%Y=interp(X,M);   % If doing interpolation, M times the sampling rate
Y=X;              % If not doing interpolation

%Plot input message signal
figure(1)
plot(t,X)
xlabel('time, sec')
ylabel('Amplitude')
title('Modulating signal')

% FM modulation parameters at BB
Fs=10/1e-4; % Sampling rate of signal
dt=1/Fs;
Fdev = 10; % Frequency deviation in modulated signal
disp(['deviation: ',num2str(Fdev)])
t=(1e-4)/M*[0:length(Y)-1]';
t0=0;
Nt=length(t);  % Number of time samples
disp(['time step (us): ',num2str(dt/1e-6)])
%Integration
YY=[];
```

137

```
YY=200*cumtrapz(t,Y);
%Modulation
theta=[];
theta=Fdev*YY.*t;
%Construct I and Q
I=[];
Q=[];
Noise=wgn(length(theta),2,-250);
I=cos(theta);+Noise(:,1);
Q=sin(theta);+Noise(:,2);
% plot FM modulated BB signal
figure(2), clf
clf
plot(t,I)
title('I')
figure(4)
plot(t,Q)
title('Q')


% recover using I and Q
mr=[];
for i=2:Nt
    dQdt=(Q(i)-Q(i-1));
    dIdt=(I(i)-I(i-1));
    Ia=(I(i)+I(i-1))/2;
    Qa=(Q(i)+Q(i-1))/2;
    % Baseband demodulation formula
    mr(i-1)=(Ia*dQdt-Qa*dIdt)/2/pi/t(i);
end
% plot demodulated signal
figure(3)
plot(t(1:Nt-1),mr,'r-')
title('Output after demodulation')
%uncomment below if amplification is required
%and set amplfication factor (volume knob)
% amplified=(mr)*volume_knob;
% for m=1:size(amplified,2)
%     if(amplified(m)>1)
%         amplified(m)=1;
%     else if (amplified(m)<-1)
%             amplified(m)=-1;
%         end
%     end
% end
%Plot I vs. Q
figure(4)
plot(I,Q,'.');
title('I vs Q')
axis([-1.1 1.1 -1.1 1.1])
grid on
toc
```

D. MATLAB CODE FOR THE SIMULATION OF TANGENT-TYPE DEMODULATION OF A SINUSOIDAL WAVEFORM

```matlab
% fm_demod_tangent_sine.m
%
%*************************************************************************
%This m file is used to simulate tangent type FM demodulation.         *
%A sine wave is created as the modulating signal and demodulated       *
%using baseband demodulation                                           *
%                                                                      *
%Written by: Fevzi Aytaç KAYA / 1st LT. / Turkish Air Force / 2010     *
%*************************************************************************


clear
clc
clf


m=pi/2e4;      %Time interval
amp=1;         %Amplitude
fc=1500000;    %carrier freq
fm=50000;      %modulating freq
df=10000;      %freq. deviation


beta=df/fm;    %Modulation Index
LPF1_order=3;  %Order of LPF before atan2 block
fs=5*(fm+fc);  %Sampling Freq.
s=1/fs;        % Sampling period
t=0:s:m;       % Time vector

%Construct message signal and integrate
message=beta*(cos(2*pi*fm*t));
theta=beta*(sin(2*pi*fm*t));

%Modulate the integrated signal
x=fmmod(theta,fc,fs,df);

%Uncomment below to plot I and Q
% figure(1)
% plot(t,x)
% title('FM Signal');

%Mix modulated signal with sinusoids I_mix and Q_mix
I_mix=sin(2*pi*fc*t);
Q_mix=cos(2*pi*fc*t);
I_lpf=x.*I_mix;
Q_lpf=x.*Q_mix;
```

139

```matlab
%---------------------------LPF---------------------------------------
% Butterworth Lowpass filter designed using the BUTTER function.
% All frequency values are in Hz.
Fs = fs;  % Sampling Frequency
N  = LPF1_order;    % Order
Fc = .4*fm;  % Cutoff Frequency
% Calculate the zpk values using the BUTTER function.
[z, p, k] = butter(N, Fc/(Fs/2));
% To avoid round-off errors, do not use the transfer function.  Instead
% get the zpk representation and convert it to second-order sections.
[sos_var,g] = zp2sos(z, p, k);
Hd          = dfilt.df2sos(sos_var, g);
%---------------------------------------------------------------------

%Filter I and Q before arctangent block
I=filter(Hd,I_lpf);
Q=filter(Hd,Q_lpf);

%arctangent and differentiate
phi=atan2(Q,I);
S1=diff(phi);

%Set time vector (same number of elements)
t2=t;
t2(:,1)=[];

%Plot the output of the differentiator
% figure(3)
% plot(t2,S1)
% title('S1(k)');

%Set first 10 samples to zero to eliminate unwanted components
for i=1:10
    S1(i)=0;
    t2(:,i)=0;
end

%Set amplification to match modulating signal
amplitude_adjust=1930;

%Plot the amplified demodulated signal
figure(4)
plot(t2,amplitude_adjust*S1,t,message,'r')
legend('Demodulated','Original');
title('Demodulated Signal vs. Modulating Signal');
xlabel('Time (sec)');
ylabel('Amplitude');
```

140

E. MATLAB CODE FOR THE SIMULATION OF TANGENT-TYPE DEMODULATION OF A VIDEO SIGNAL

```matlab
% fm_demod_tangent_video.m
%
%************************************************************************
%This m file is used to simulate tangent type FM demodulation.        *
%A text file including video data captured by a video camera is       *
%reuired. The video data is modulated and demodulated back by using   *
%tangent type demodulation.                                           *
%                                                                     *
%Written by: Fevzi Aytaç KAYA / 1st LT. / Turkish Air Force / 2010    *
%************************************************************************


clear
clc
tic

%Amplification at the output is set here
volume_knob=16.1;  % Range 1-30 (suggested)
do_improvement=1;   %Set to 1 if improvement is desired

AA=dlmread('TextFile7.txt'); %Read video data in TextFile.txt
n1=1; n2=length(AA);
V=AA(n1:n2);
clear AA

t=1e-4*[0:length(V)-1]';
Vmax=max(V); Vmin=min(V); V0=max([Vmax,abs(Vmin)]);
X=V/V0;    %Normalization

% Y=X;
figure(1)
plot(t,X)
xlabel('time, sec')
ylabel('Amplitude')
title('Speech waveform from LabVIEW')

% FM signal
fc=20000;       %carrier freq
fs=10/1e-4;     %Sampling freq
Fdev=1000;       %freq. deviation
t=(1e-4)/3*[0:length(X)-1]';

%Modulate
modulated=fmmod(X,fc,fs,Fdev);
```

141

```matlab
%plot modulated signal
figure(2)
plot(t,modulated)
title('FM Signal');

%----------------Add-noise------------------------------------------
%I_mod = awgn(x,30,'measured'); % Add white Gaussian noise.
%-------------------------------------------------------------------

%Mix with sinusoids
I_mix=sin(2*pi*fc*t);
Q_mix=cos(2*pi*fc*t);
I_lpf=modulated.*I_mix;
Q_lpf=modulated.*Q_mix;

%---------------------------LPF-------------------------------------
% Butterworth Lowpass filter designed using the BUTTER function.
% All frequency values are in Hz.
Fs = fs;        % Sampling Frequency
N  = 3;         % Order
Fc = fc;      % Cutoff Frequency
% Calculate the zpk values using the BUTTER function.
[z, p, k] = butter(N, Fc/(Fs/2));
% To avoid round-off errors, do not use the transfer function.  Instead
% get the zpk representation and convert it to second-order sections.
[sos_var,g] = zp2sos(z, p, k);
Hd          = dfilt.df2sos(sos_var, g);
%-------------------------------------------------------------------
%Filter I and Q signals
I=filter(Hd,I_lpf);
Q=filter(Hd,Q_lpf);

%Tangent type demodulation and differentiation
phi=atan2(Q,I);
S1=diff(phi);

%Start improved tan-type demodulator
%Add C1(k)
if do_improvement==1
    C1=zeros(size(S1),1);
    for j=2:size(S1)
        if S1(j)<0
            C1(j)=2*pi;
        end
    end
    S2=S1+C1;
End
%------------------End_of_Improvement-------------------------------
```

```matlab
if do_improvement==1
    demodulated=S2;
else
    demodulated=S1;
end

t2=t;
t2(size(t,1))=[];

%Amplification is done here
amplified=(demodulated-0.83775)*volume_knob;

for m=1:size(amplified)
    if(amplified(m)>1)
        amplified(m)=1;
    else if (amplified(m)<-1)
            amplified(m)=-1;
        end
    end
end

amplified=amplified.*(-1);

figure(3)
%plot(t,X,t2,amplified,'r')  %Compare with this
plot(t2,amplified,'r')       %Output only
xlabel('Time (sec)');
ylabel('Amplitude');
title('Demodulated video signal');

%Plot I and Q circle
figure(4)
plot(I,Q,'.');
title('I vs Q')
xlabel('I');
ylabel('Q');
toc
```

THIS PAGE INTENTIONALLY LEFT BLANK

LIST OF REFERENCES

[1]   C. A. Hughes, "Achieving and enduring air dominance," Research Report, Air Command and Staff College, Air University, Maxwell Air Force Base, Alabama, April 1998.

[2]   C. Beal, J. Boatman, and M. Hewish, "UAV development: The art of compromise," *Jane's International Defense Review*, vol. 26, issue 5, May 1, 1993.

[3]   "Unmanned aerial vehicle," July 5, 2010. [Online]. Available: http://en.wikipedia.org/wiki/Unmanned_aerial_vehicle. [Accessed July 11, 2010].

[4]   P. E. Pace, *Detecting and Classifying Low Probability of Intercept Radar.* 2nd Ed., Norwood, MA: Artech House, pp. 323-325, 2009.

[5]   Photo by Photographer's Mate 2nd Class Daniel J. McLain, "RQ-2B Pioneer UAV," December 22, 2006. [Online]. Available: http://upload.wikimedia.org/wikipedia/commons/1/18/RQ-2B_pioneer_uav.jpg, [Accessed July 11, 2010].

[6]   D. C. Jenn, Y. Loke, T. C. H. Matthew, Y. E. Choon, O. S. Siang, and Y. S. Yam, "Distributed phased arrays and wireless beamforming networks," *International Journal of Distributed Sensor Networks*, pp. 283–302, 2009.

[7]   J. A. Bartee, "Genetic algorithms as a tool for phased array radar design," Master's Thesis, Naval Postgraduate School, Monterey, California, June 2002.

[8]   C. S. Ong, "Digital phased array architectures for radar and communications based on off-the-shelf wireless technologies," Master's Thesis, Naval Postgraduate School, Monterey, California, December 2004.

[9]   G. M. Burgstaller, "Wirelessly networked digital phased array," Master's Thesis, Naval Postgraduate School, Monterey, California, September 2006.

[10]   B. L. Gezer, "Multi-beam digital antenna for radar, communications, and UAV tracking based on off-the-shelf wireless technologies," Master's Thesis, Naval Postgraduate School, Monterey, California, September 2006.

[11]   A. Lee, "Variable resolution direction finding using the robust symmetrical number system," Master's Thesis, Naval Postgraduate School, Monterey, California, December 2006.

[12]   J. Benveniste, "Design and development of a single channel RSNS direction finder," Master's Thesis, Naval Postgraduate School, Monterey, California, March 2009.

[13]   I. L. Tan and D. J. Pandya, "UAV digital tracking array design, development and testing," Master's Thesis, Naval Postgraduate School, Monterey, California, December 2009.

[14]   M. Skolnik, *Introduction to Radar Systems,* 3rd Ed., New York: McGraw-Hill, New York, pp. 210–229, 2001.

[15]   Photo by Hamish Lindsay, "The FPQ Skin Tracking Radar," 22 October 2004. [Online]. Available: http://www.honeysucklecreek.net/images/other_stations/croq6dsh1.jpg, [Accessed July 18, 2010].

[16]   D. C. Jenn, "Microwave devices & radar," vol. II, pp. 111–115, 2009 (unpublished lecture notes).

[17]   K. W. Kwai, P. E. Pace, D. C. Jenn, and J. C. Chen, "Robust symmetrical number system direction finding arrays with virtual spacing," Naval Postgraduate School, Monterey, California, (unpublished notes).

[18]   D. C. Jenn, "RSNS processing using a single channel," Naval Postgraduate School, Monterey, California, (unpublished notes).

[19]   D. C. Jenn, "Digital antennas," Naval Postgraduate School, Monterey, California, (unpublished notes).

[20]   S. J. Roome, "Analysis of quadrature detectors using complex envelope notation," *IEEE Proceedings*, vol. 136, Pt. F, no. 2, April 1989.

[21]   B. Razavi, "Design considerations for direct conversion receivers," Circuits and Systems II: *Analog and Digital Signal Processing, IEEE Transactions on* 44(6), pp. 428–435, 1997.

[22]   National Instruments, "Anatomy of a video signal," December 6, 2006. [Online]. Available: http://zone.ni.com/devzone/cda/tut/p/id/3020, [Accessed July 14, 2010].

[23]   "NTSC   scanning,   timing/sync,   sync   recovery,   numbers."   [Online].
        Available: http://www.ntsc-tv.com/. [Accessed July 14, 2010].

[24]   W. Tomasi, *Electronic Communication Systems: Fundamentals Through
        Advanced,* 5th Ed., pp. 254–282, Upper Saddle River, New Jersey: Pearson
        Prentice Hall, 2004.

[25]   K. M. E. Hui, "Digital tracking array for FM signals based on off-the-shelf
        wireless technologies," Master's Thesis, Naval Postgraduate School, Monterey,
        California, December 2007.

[26]   M. Hagiwara and M. Nakagawa, "Performance of improved tangent-type FM
        demodulator using digital signal processing," *Electronics and Communications in
        Japan*, vol. 67-B, no.10, 1984.

[27]   F. Shadt, F. Mohr and M. Holzer, "FM demodulation of IQ baseband signals
        using Kalman filters," *Radioelektronika, 18th International Conference*, 2008.

[28]   W. L. Stutzman and G. A. Thiele, "*Antenna Theory and Design*," 2nd Ed.,
        Hoboken, New Jersey: John Wiley & Sons, Inc., p. 173, 1998.

[29]   D. C. Jenn, "Microwave devices & radar," vol.II, pp. 9–10, 2009 (lecture notes).

[30]   C. H. Eng, "Design and development of an automated demodulator calibration
        station," Master's Thesis, Naval Postgraduate School, Monterey, California,
        December 2009.

[31]   Analog Devices, "Direct Conversion Quadrature Demodulator Datasheet," 2005.
        [Online]. Available:
         http://www.analog.com/static/imported-files/data_sheets/AD8347.pdf.
        [Accessed July 21, 2010].

[32]   K. Forsberg, H. Mooz and H. Cotterman, "*Visualizing Project Management,*" 3rd
        Ed., Hoboken, New Jersey: John Wiley & Sons, Inc., p. 361, 2005.

THIS PAGE INTENTIONALLY LEFT BLANK

INITIAL DISTRIBUTION LIST

1.   Defense Technical Information Center
   Ft. Belvoir, Virginia

2.   Dudley Knox Library
   Naval Postgraduate School
   Monterey, California

3.   Prof. Dan Boger
   Department of Information Sciences
   Naval Postgraduate School
   Monterey, California

4.   Prof. Clark Robertson
   Department of Electrical and Computer
   Naval Postgraduate School
   Monterey, California

5.   Prof. David Jenn
   Department of Electrical and Computer
   Naval Postgraduate School
   Monterey, California

6.   Lt. Col. Terry Smith
   Department of Information Sciences
   Naval Postgraduate School
   Monterey, California

7.   Robert D. Broadston
   Department of Electrical and Computer
   Naval Postgraduate School
   Monterey, California

8.   Prof. Kevin Jones
   Department of Aeronautics and Astronautics
   Naval Postgraduate School
   Monterey, California

9.   1st Lt. Fevzi Aytaç Kaya
   Turkish Air Force Electronic Warfare Support Center Command, Ankara, Turkey